Search for Excited Leptons in the Leptonic Contact-Interaction Decay Channel with 2016 CMS Data

Masterarbeit

von

Christoph Schuler

vorgelegt der

Fakultät fur Mathematik, Informatik und Naturwissenschaften der RWTH Aachen

erstellt im

Februar 2017

bei

Prof. Dr. Thomas Hebbeker

Zweitgutachter

Prof. Dr. Christopher Wiebusch

Abstract

This thesis presents an analysis of 2016 CMS data with 35.9 $\text{fb}^{-1}$of $\sqrt{s} = 13$ TeV proton-proton collisions. A search for excited leptons in the leptonic contact-interaction decay channel is performed. This includes seven different final states: four electrons, three electrons, two electrons and one muon, two electrons and two muons (which is analysed for both a possible e^* as well as a possible μ^*), one electron and two muons, three muons, and four muons. Using a veto on Z-bosons, possible signals can be distinguished quite easily from any background coming from the Standard Model of Particle Physics. The data are consistent with the background prediction within the evaluated uncertainties. Therefore limits can be set on the compositeness scale Λ as well as the mass of the excited electron / muon. Masses between 200 GeV and 4.5 (4.6) TeV at 95% confidence level can be excluded for excited electrons (muons). In Λ, the exclusion limits reach up to 10.5 (11) TeV at low excited lepton masses.

Zusammenfassung

Diese Arbeit behandelt eine Suche nach angeregten Leptonen im Contact-Interaction Zerfallskanal in den 2016er Daten die CMS an Proton-Proton Kollisionen aufgenommen hat. Die Schwerpunktsenergie dieser Daten ist $\sqrt{s} = 13$ TeV und die integrierte Luminosität beträgt 35.9 fb^{-1}. Schwerpunkt der Suche sind sieben verschiedene Kanäle: der vier-Elektronen-Kanal, der drei-Elektronen-Kanal, der zwei-Elektronen-ein-Myon-Kanal, der zwei-Elektronen-zwei-Myonen-Kanal (welcher sowohl für den Fall eines erzeugten e^* als auch für den Fall eines erzeugten μ^* untersucht wird), der ein-Elektron-zwei-Myonen-Kanal, der drei-Myonen-Kanal, sowie der vier-Myonen-Kanal. Der erwartete Standard-Modell-Einfluss wird mithilfe eines Z-Vetos reduziert, was das Signal stark von diesem abhebt. Es wurde keine außerhalb der Fehler signifikante Abweichung zwischen Messung und Vorhersage gefunden. Auf Grund dessen wurden Ausschlussgrenzen auf die mögliche Skala der Substruktur eines angeregten Leptons Λ und die Masse eines solchen Teilchens gesetzt. Für angeregte Leptonen können Massen von 200 GeV bis 4.5 (4.6) TeV für angeregte Elektronen (Myonen) bei 95% Konfidenzniveau ausgeschlossen werden. Für geringe Massen dieser Teilchen können Werte von Λ bis zu 10.5 (11) TeV ausgeschlossen werden.

Contents

1 Introduction **3**
1.1 Units and Notation . . . 4

2 Theory **5**
2.1 The Standard Model of Particle Physics . . . 5
2.1.1 The Weak Force and Electroweak Unification . . . 5
2.1.2 Quantum Chromodynamics . . . 8
2.2 Excited Leptons . . . 8

3 LHC and the CMS Detector **13**
3.1 The Large Hadron Collider . . . 13
3.2 The Compact Muon Solenoid . . . 13
3.2.1 Coordinate System . . . 15
3.2.2 The Detector Components . . . 15
3.2.3 The Trigger System . . . 19

4 Analyzed dataset and Monte Carlo **22**
4.1 The 2016 Dataset . . . 22
4.1.1 Monte Carlo Simulation . . . 22
4.1.2 Expected Backgrounds . . . 23
4.1.3 Signal Generation . . . 24
4.1.4 Signal Characteristics . . . 27

5 Analysis **32**
5.1 Event Selection . . . 32
5.2 Object Reconstruction . . . 34
5.2.1 Electrons . . . 34
5.2.2 Muons . . . 34
5.3 Kinematic Selection . . . 37
5.4 Invariant mass distribution . . . 41
5.5 The Control Region . . . 41
5.6 Background Prediction Corrections . . . 45
5.6.1 Pileup Reweighting . . . 45
5.6.2 Scale Factors . . . 45
5.7 Systematic Uncertainties . . . 47

6 Results **51**
6.1 The Signal Region . . . 51
6.2 Statistical Interpretation . . . 55
6.2.1 Background Fitting Method . . . 55
6.2.2 Limit setting . . . 58
6.2.3 Comparison to other analyses . . . 60

7 Conclusion and Outlook **61**

8 Appendix **62**
8.1 Channel dependent cuts 62
8.2 The Z cut 62
8.3 Event Displays 62
8.4 Limits 62

1 Introduction

«Curiosity demands that we ask questions, that we try to put things together and try to understand [...]»(Richard Feynman - The Feynman Lectures on Physics Vols 1-2)

For a long time, mankind has searched for answers to the question what we and the universe are made of. In time, scientists have provided theories and models, which were tested, sometimes refined and sometimes discarded. The current best description of the elemental processes and particles is called the Standard Model of Particle Physics, which has been tested over decades. Still, there are open questions the Standard Model fails to answer properly. Therefore, other theories, designed as enhancements or extensions of the Standard Model, are pursued of and have to be tested. For example, the Standard Model describes quarks and leptons, which have an intriguingly similar structure in terms of their generations. There are models, which assume a compositeness for quarks and leptons, which could explain this structure (aswell as some other aspects, e.g. the electrical charge of those particles).

The assumption of a substructure of particles is not completely new, as there are several examples in the history of science, where a compositeness was discovered of what was previously thought to be the 'smallest component'. Atoms were found to consist of protons, neutrons and electrons, and, in turn, protons were found to have an extremely complex substructure themselves. Thus, the assumption is a quite natural one. All these composite particles do have excited states. Therefore, the discovery of an excited quark or lepton would be a significant hint towards a possible substructure of those fermions.

One such model predicts the production of excited states of fermions at high-energy hadron colliders. This could be measured at detectors such as CMS. Searches for excited quarks have been performed and have not shown any evidence of a substructure yet [1,2]. In this thesis, a search is performed in the 35.9 fb^{-1}2016 CMS dataset for excited electrons and muons, which are created via contact-interaction and in turn, as the theory predicts, could decay via contact-interaction leptonically, leading to final states with three or more leptons. The word 'contact-interaction' describes short-distance physics, which do not possess poles in the accesible range of any kinematic variables. The exact kinematics of those processes are therefore not known and are instead described by effective operators.

This is the first time, that anyone has searched for this model in this decay channel. A large benefit of this search region is the fact, that the expected background of the Standard Model is extremely low compared to other possible channels. This channel is best suited to search for a high-mass excited lepton, as the branching ratio favors contact-interaction decay channels in this region.

1.1 Units and Notation

In this thesis, most values are given in natural units, which are commonly used in high-energy physics. In this unit system, $\hbar$ (the reduced Planck constant) and c (the speed of light) are both set to 1. Using this convention, both masses and momenta (in addition to energy) are given in eV (or 10^9 eV = 1 GeV). Charges are provided in multiples of the elementary charge e. This convention is used, as values for masses or momenta are typically extremely small compared to SI units (e.g. proton mass: $m_P = 1.672621777(74) \cdot 10^{-27}$ kg). Interaction cross sections are given in pico or femto barns (1 pb = 1000 fb = 10^{-40} m^2), depending on the specific process looked at. Correspondingly, the unit used for the intergrated luminosity, which is a quantity to describe the size of the data set, is fb^{-1}.

The theoretical framework of this thesis is, as it is about high energy physics, using the common relativistic notation, which is therefore explained here shortly. The momentum of a particle is given in the position-time four-vector notation

$$p^\mu = \begin{pmatrix} t \\ x_1 \\ x_2 \\ x_3 \end{pmatrix} \tag{1}$$

where t is the time coordinate, and x_1, x_2 and x_3 are the coordinates for space (c=1). One defines a covariant four-vector p_μ via this contravariant vector and the metric $g_{\mu\nu}$:

$$p_\nu = g_{\mu\nu} p^\mu$$

with

$$g_{\mu\nu} = \begin{pmatrix} 1 & 0 & 0 & 0 \\ 0 & -1 & 0 & 0 \\ 0 & 0 & -1 & 0 \\ 0 & 0 & 0 & -1 \end{pmatrix} \tag{2}$$

The product $p_\mu p^\mu$ is invariant under Lorentz-transformation. In the Standard Model the so called 'gamma matrices' γ^μ play an important role. They were introduced by Dirac and have to fulfil [3]

$$\gamma^\mu \gamma^\nu + \gamma^\nu \gamma^\mu = 2g^{\mu\nu}$$

2 Theory

This chapter introduces the Standard Model of Particle Physics (SM), the most accepted and well tested model for elementary particle physics. As this model is quite complex, only basic concepts and for this thesis relevant aspects will be explained. Afterwards, a short overview on the theory of excited leptons is given, which is more of a possible extension of the Standard Model rather than an independent model.

Unless otherwise noted, information on the SM is taken from [4, 5].

2.1 The Standard Model of Particle Physics

Current knowledge of physics states fermions, which are the particles matter consists of, and bosons, which are responsible for interactions between those particles. An overview of all elementary particles is given in Fig. 1. Fermions, which have a spin equal to 1/2, are divided into quarks (q) and leptons (ℓ). They are grouped (columnwise) in doublets to so called 'generations', as they exhibit a similar behaviour. Between the generations, particles mainly differ in mass. Leptons are additionally divided into the charged leptons electron (e), muon (µ) and tau (τ), and their corresponding electrically neutral neutrinos (ν_e, ν_μ, ν_τ). Each fermion in this table has a corresponding anti-particle, which has the same mass and spin, but reversed sign in all other quantities (like charge).

These particles interact with each other by mediating particles. These particles are called 'bosons', as they have integer spins. The mediator of the electromagnetic force is the photon (γ), which interacts with electrically charged particles like the electron or the muon. The gluon is the mediator of the strong interaction, which couples to particles with color charge. The only fermions, which carry this charge. are the six quarks up(u), down(d), charm(c), strange(s), top(t) and bottom(b). The mediators of the weak force are the Z and W (W^+, W^-) bosons, which explain the beta decay of radioactive nuclei.

A rather new addition is the Higgs boson, which was found in 2012 by the ATLAS and CMS experiments [6, 7]. This scalar boson is a result of spontaneous symmetry breaking, which is needed to allow the W and Z bosons to obtain mass. Compared to the other bosons, it does not carry a force itself.

The gravitational force is not included in the Standard Model, but instead is described by Einstein's theory of general relativity.

2.1.1 The Weak Force and Electroweak Unification

The weak interaction is described by quantum flavor dynamics (QFD), which allows parity-violating processes. It has more than one mediator: 'Neutral currents' are mediated by the Z-boson and 'charged currents' are transmitted via the $W^{\pm}$-boson. The latter one can change the flavor of quarks and leptons. The charge of the weak interaction is the 'weak isospin' (T). The first formulation of the weak theory was given

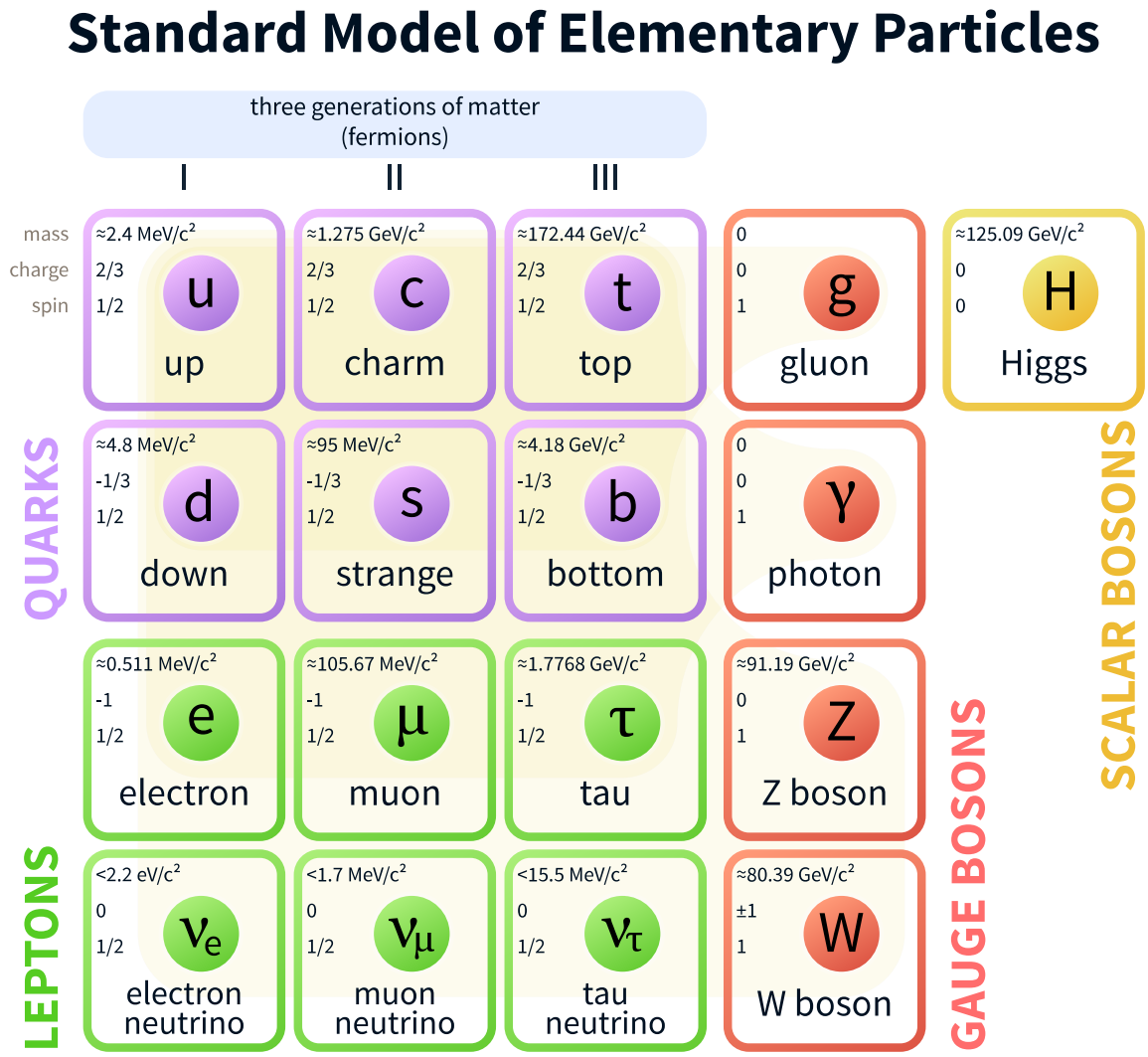

Figure 1: Overview of all elementary particles known to the Standard Model of Particle Physics [8].

by Fermi in 1933 [9], when he was trying to explain the radioactive β-decay. Fermi imposed the interaction as a contact-interaction with a coupling strength G_F ('Fermi constant'), in which he makes no precise predictions on the exact kinematics of the process. As explained in [4], the correct propagator for the W and Z bosons is given by (inserting either M_W or M_Z for M)

$$\frac{-i(g_{\mu\nu} - q_\mu q_\nu / M^2)}{q^2 - M^2}$$

where $g_{\mu\nu}$ is the Minkowski metric given in 1.1, and q^2 is the tranferred momentum. This is typically much smaller than the mass of the W or Z boson, in which case the formular simplifies to that of a contact interaction. With this knowledge, the Fermi constant can be written as

$$G_F = \frac{\sqrt{2}}{8} \frac{g^2}{M_W^2} = 1.1663787(6) \cdot 10^{-5} \text{ GeV}^{-2}$$

where g is the weak coupling constant.

The electroweak unification describes the fact, that quantum electrodynamics (QED) and QFD are formluated within the same mathematical formalism (they are 'manifestations' of the same electroweak interaction). The obvious difference between these two, the corresponding strength of the forces, can be solved, if the mediators of the weak force are extremely massive. The Glashow-Weinberg-Salam model [10,11] predicts four massless fields (W^1, W^2, W^3, B) with corresponding coupling constants g and g'. The fields mix to these physical bosons:

$$W^\pm = \sqrt{\frac{1}{2\pi}}(W^1 \mp iW^2)$$

$$Z = -B \sin\Theta_W + W^3 \cos\Theta_W$$

$$\gamma = B \cos\Theta_W - W^3 \sin\Theta_W$$

with Θ_W being the weak mixing angle (also called 'Weinberg angle'), measured to $\sin^2(\Theta_W) = 0.23$ [12]. In this unification, the 'weak hypercharge' (Y) is defined, which connects electrical charge (Q) and third component of the weak isospin T_3 via the Gell-Mann-Nishijima equation

$$\mathrm{Q} = \frac{1}{2}\mathrm{Y} + \mathrm{T}_3$$

The weak coupling constants g and g' and the electromagnetic coupling constant (g_e) are related [4]:

$$g \sin\Theta_W = g' \cos\Theta_W = g_e$$

This formalism does not itself state a mass in itself for the W and Z bosons, as it would break local gauge invariance. This problem is solved by the Higgs mechanism [1].

2.1.2 Quantum Chromodynamics

Quantum chromodynamics (QCD) is the theory used to described interactions between quarks and gluons. These particles are the only ones, which carry so called 'color' charge. This theory is formulated as a $SU(3)$-group and describes the properties of the strong interaction, whose mediator is the gluon. The most significant difference to electrodynamics (as they both couple to some form of charged particle) is the fact, that, while in QED there is only one kind of charge, there are three types of charge in QCD (green, red and blue). Each quark can carry one type of this charge, and gluons carry two types of this charge. Now, as the mediator themselves carry the charge they couple to, there is the possibility of gluons coupling to each other, which makes the theory significantly more complicated compared to quantum electrodynamics.

All particles, which were measured so far, do not carry any color charge, they are 'colorless'. This phenomenon, that colored particles cannot be isolated, is called 'confinement'. If any two color charges are seperated (in distance to one-another), at some point it becomes energetically favorable for a new quark-antiquark pair to appear, which leads (for particle accelerators like the LHC and its experiments) to the production of 'jets', which are many colorless particles clustered together.

Quark-gluon interaction introduces a factor of $\frac{-ig_s}{2}\lambda^a\gamma^\mu$, where λ^a stands for the Gell-Mann λ-matrices and g_s is the strong coupling constant. This 'constant' depends on the momentum transfer q^2. At very short distances, the 'strong' force becomes relatively weak, which often is referred to as 'asymptotic freedom' [4].

2.2 Excited Leptons

The concept for the existence of excited leptons is quite natural. In science history, there were several discoveries of a substructure to what was previously thought to be the smallest particle. As we know, the proton and the neutron both consist of more-elementary subparticles, the previously mentioned quarks. A similar substructure could be possible for any fermion currently known. For example, an electron could consist of any number of more-elementary particles, which are too small to be measured directly with current known methods. If this substructure is real, it would be necessary for fermions to have excited states, with masses at least of the order of a few hundred GeV [3]. This model may explain the existance of fermionic generations and their rather complex pattern of masses and mixing angles [13, 14].

Quantum numbers of excited and ordinary leptons are expected to be the same and conserved in physical processes, which makes the only difference between 'normal' leptons and excited leptons their respective mass and their lifetime [15]. Excited leptons and excited neutrinos form an isospin doublet of the form [13]

$$\begin{pmatrix}\nu_\ell\\ \ell^-\end{pmatrix}_L, \quad \ell^-_R \begin{pmatrix}\nu^*_\ell\\ \ell^{*-}\end{pmatrix}_L, \quad \begin{pmatrix}\nu^*_\ell\\ \ell^{*-}\end{pmatrix}_R \tag{3}$$

These assumptions limit the number of parameters in the theory and also allow for non-zero masses prior to $\mathrm{SU_L(2)\times U(1)}$-symmetry breaking [3, 13].

The coupling of excited fermions to bosons is described by [3]

$$\mathcal{L} = \frac{1}{2}\bar{f}^*\gamma^\mu \left(g_s\lambda^a G^a_\mu + g\tau W_\mu + g^{'} Y B_\mu\right) f^*$$

where f^* is the excited fermion state and Y is their weak hypercharge (-1 for leptons and 1/3 for quarks). g_s, g, and $g^{'}$ are the strong and electroweak gauge couplings and G^a_μ, W_μ and B_μ describe the gluon, the $\mathrm{SU_L(2)}$ and the U(1) gauge fields.

The gauge bosons can be used to describe the transition from right-handed excited leptons to ordinary left-handed leptons, and vice versa, via [3]

$$\mathcal{L} = \frac{1}{2\Lambda}\bar{f}^*_R\sigma^{\mu\nu}\left(g_s f_s \frac{\lambda^a}{2} G^a_{\mu\nu} + g f \frac{\tau}{2} W_{\mu\nu} + g' f' \frac{Y}{2} B_{\mu\nu}\right) f_L + h.c.$$

where Λ is the compositness scale, and f, f_s, and f′ are parameters, which depend on the dynamics of the compositness and are therefore unknown. Depending on these parameters, the coupling of the excited leptons to the bosons can differ significantly. For this analysis however, only the decay is studied with a contact interaction (CI) Lagrangian given by [3]

$$\mathcal{L}_{CI} = \frac{g^2_*}{2\Lambda^2} j^\mu j_\mu$$

with

$$j_\mu = \eta_L \bar{f}_L\gamma^\mu f_L + \eta^{'}_L \bar{f}^*_L\gamma^\mu f^*_L + \eta^{''}_L \bar{f}^*_L\gamma^\mu f_L + H.c. + (L \to R)$$

which has no dependency on these factors. For all further investigation, g^2_* is set to 4π, the η factors of left-handed currents are set to one for simplicity, and those of the right-handed currents are set to zero. 'Contact interaction' describes short-distance physics, which do not possess poles in the accesible range of any kinematic variables. The exact kinematics of those processes are therefore not known and are instead described by effective operators. In this model, this type of interaction is only valid for energies below the compositeness scale Λ [3].

A Feynman diagram for the creation of such an excited fermion in a proton-proton collision is given in Fig. 2.

For excited leptons, the contact-interaction creation can take place either singly via $qq \to \ell\ell^*$ or pairwise via $qq \to \ell^*\ell^*$. The corresponding cross sections for these processes (based on the CI-Lagrangian) are

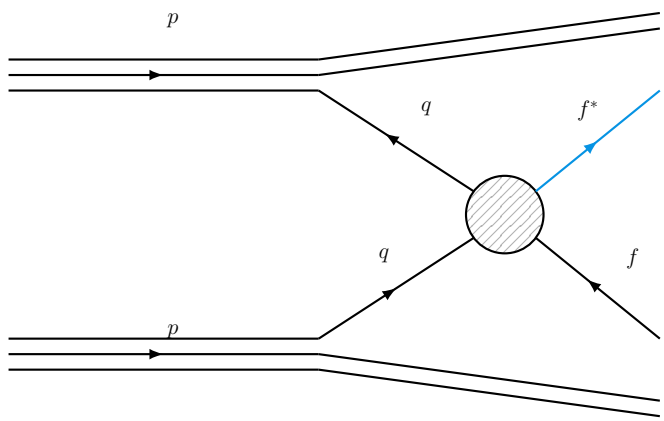

Figure 2: Possible Feynman diagram for the creation of an excited fermion (quark or lepton) in proton-proton collisions.

$$\sigma(qq \to \ell\ell^*) = \frac{\pi\hat{s}}{6\Lambda^4}\left(1+\frac{v}{3}\right) \times \left(1-\frac{m^{*2}}{\hat{s}}\right)\left(1+\frac{m^{*2}}{\hat{s}}\right)$$

and

$$\sigma(qq \to \ell^*\ell^*) = \frac{\pi\tilde{v}\hat{s}}{12\Lambda^4}\left(1+\frac{\tilde{v}^2}{3}\right)$$

with

$$v = \frac{\hat{s}-m^{*2}}{\hat{s}+m^{*2}} \text{ and } \tilde{v} = \sqrt{1-4\frac{m^{*2}}{\hat{s}}}$$

.

Excited leptons can decay either to a light lepton in conjunction with a boson ($\ell \to \ell V$ with $V = Z, W, \gamma$) or to several leptons ($\ell \to \ell\ell'\ell'$ with $\ell' = e, \mu, \tau$). The Feynman diagrams of the possible decays of the excited lepton are shown in Fig. 3. The branching ratio (BR) of each possible decay is shown in Fig. 4. It can be seen, that the contact-interaction decay channels ($\ell\ell\ell$, ℓqq) have a significantly larger BR for high M^*/Λ, which makes those channels more sensitive search regions for high-mass excited leptons. Although the $\ell\ell\ell$ channel has a smaller branching fraction compared to ℓqq, it benefits from the fact, that there is very little background expected from the Standard Model. The decay width for the contact-interaction decay is given by [3]

$$\Gamma(\ell^* \to \ell + \ell'\bar{\ell}') = \frac{m^*}{96\pi}\left(\frac{m^*}{\Lambda}\right)^4 S'$$

where S' is a combinatorical factor with $S' = 1$ for $\ell \neq \ell'$ and $S' = 2$ for $\ell = \ell'$. The decay width is highly dependent on m^*/Λ.

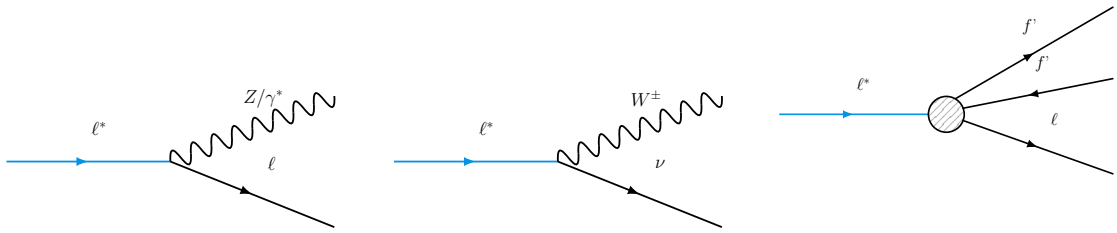

Decay with a γ or Z boson. Decay with a W boson. Contact-Interaction decay. $f'f'$-pair can be any fermion set, and does not have to be equal to $\ell\ell$.

Figure 3: Overview of the Feynman diagrams for the various decay possibilites of a created ℓ^*.

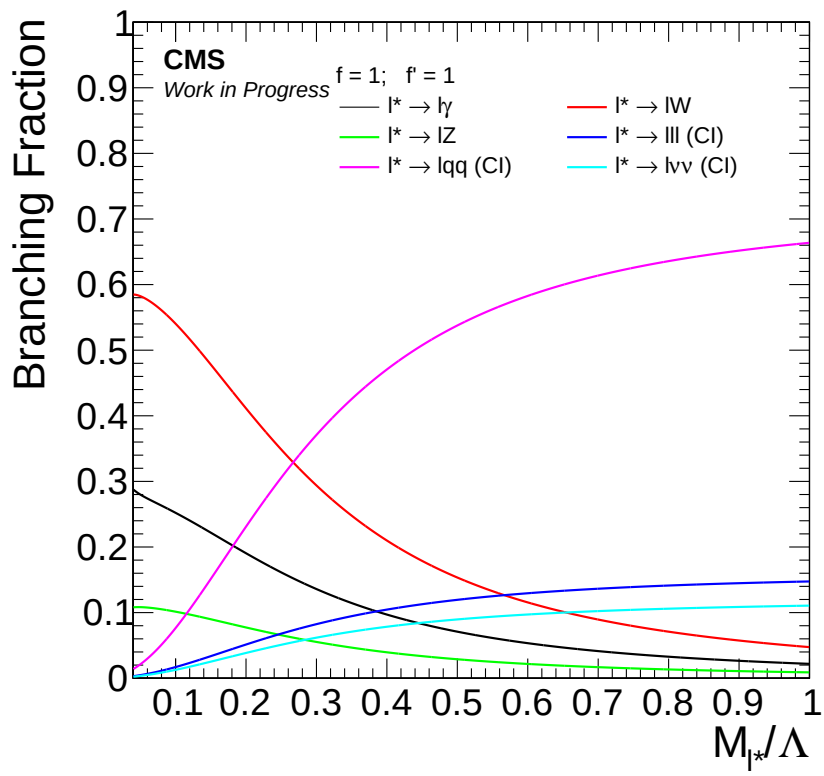

Figure 4: Branching fraction of the ℓ^* decay for f=f′=1. A common alternative (f=-f′=1) does not affect the CI-channels, but is only relevant for the bosonic decays. The channel analysed in this thesis is shown in blue and benefits from a small background expectation from the SM.

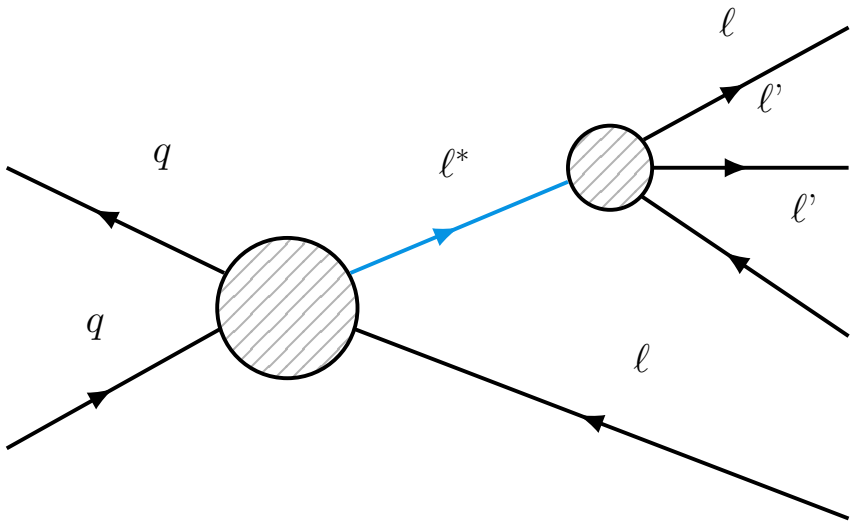

Figure 5: Feynman diagram of the signal model. The exact dynamics at the vertex is not known in contact interaction theory and thus is only indicated by a grey circle. Note, that ℓ' does not have to be equal to ℓ, but it can be ($\ell = e, \mu$).

The full Feynman diagram for the process relevant for this search is given in Fig. 5.

Searches for excited leptons have been performed in the $\ell\ell\gamma$- and the $\ell\ell Z$-channels, but have not resulted in any evidence of the existence of those. The best current 95% confindece level exclusion limits are at 3.0 / 2.8 TeV in mass for the excited muon / electron [16,17]. In terms of the compositness scale Λ, values of up to 17 TeV have been excluded.

3 LHC and the CMS Detector

This analysis uses data taken from the Compact Muon Solenoid (CMS) [18] detector, which is located at the Large Hadron Collider (LHC) [19] at CERN. This chapter explains the experimental setup and basic quantities in more detail, which will be used in this thesis.

3.1 The Large Hadron Collider

The Large Hadron Collider (LHC) [19] is the world's largest particle accelerator. It is located at CERN, Geneva and measures almost 27 km in circumference. It is located in the tunnel previously used by the Large Electron-Positron Collider (LEP) [20]. The LHC is part of an accelerator chain (shown in Fig. 6), which in total can accelerate protons up to an energy of 7 TeV (or, in case of lead acceleration, up to 2.75 TeV) per particle. The pre-LHC accelerator injects protons with an energy of 450 GeV into the LHC in bulks of particles, so called bunches.

In the LHC ring, the particles are guided by magnetic fields maintained by superconducting electromagnets through two beam pipes kept at ultrahigh-vacuum. The beams travel in opposite directions and can be brought to collision at the interation points, where the experiments are located.

At the LHC, there are four major experiments: ALICE (A Large Ion Collider Experiment) [22], the ATLAS experiment [23], CMS (Compact Muon Solenoid) [18], and LHCb (Large Hadron Collider beauty) [24]. While ALICE focusses on the analysis of heavy ion collisions, and LHCb is designed to analyse decays of b-hadronds, ATLAS and CMS are multipurpose experiments able to search for new physics at high energies.

3.2 The Compact Muon Solenoid

If not otherwise noted, all information on the detector is taken from [18].

The Compact Muon Solenoid (CMS) is a multi-purpose detector at LHC, located 100 meter underground between lake Geneva and the Jura mountains. It is designed to measure data from proton-proton (lead-lead) interactions at a center-of-mass energy of 14 TeV (5.5 TeV) at a luminosity of 10^{34} cm^{-1} s^{-1} (10^{27} cm^{-1} s^{-1}). Its design goals concerning performance are:

- Good muon reconstruction, charge determination and a high momentum resolution for muons with momenta up to the TeV scale.
- Good charged particle reconstruction in the tracker. Efficient tagging of τ's and b-jets.
- Highly efficient photon and lepton isolation at high luminosity as well as good electromagnetic energy resolution overall.
- Good missing-transverse energy (MET) and dijet-mass resolution.

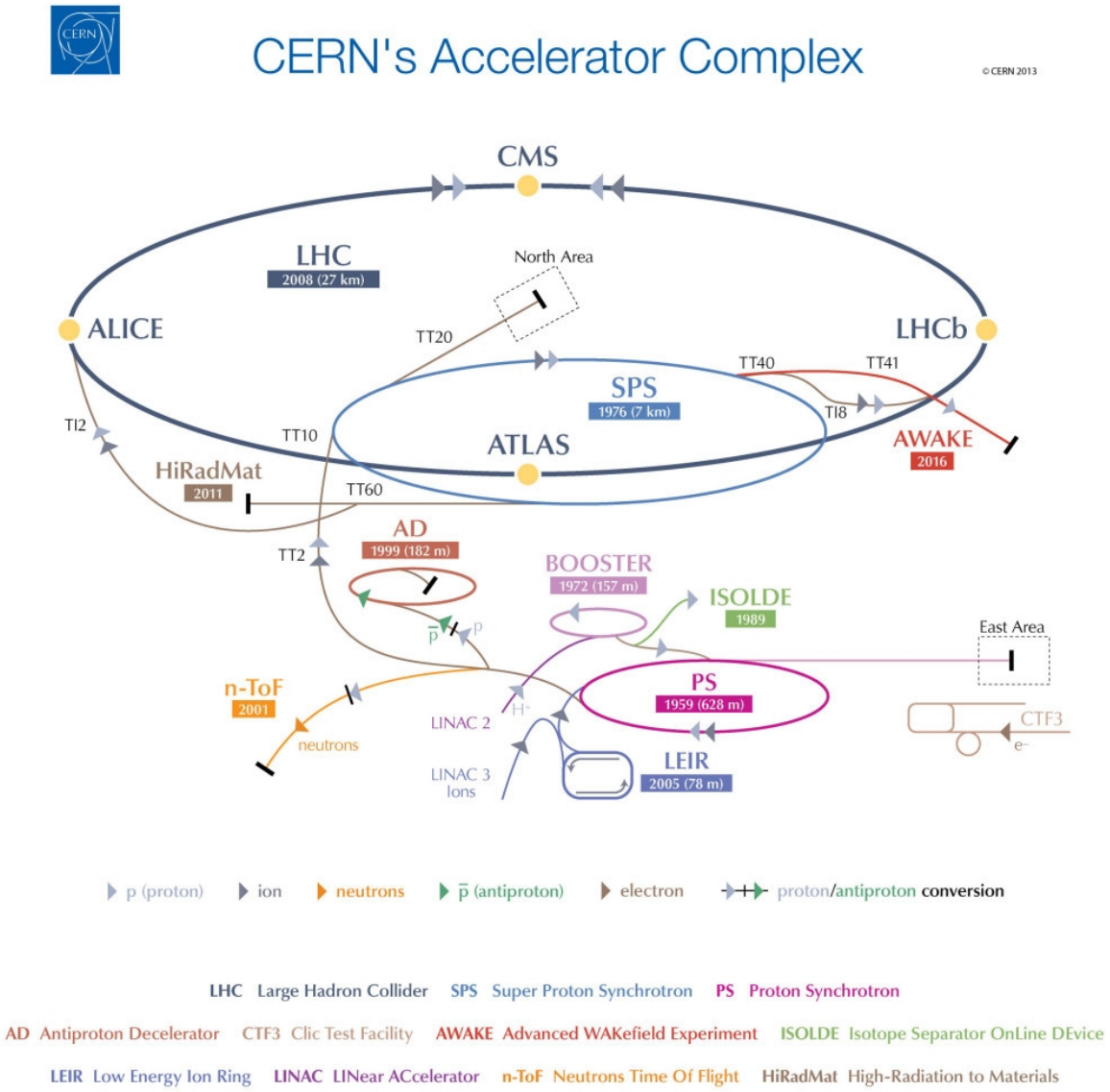

Figure 6: CERN's accelerator complex: For proton-proton acceleration, H^+-ions get accelerated by the linear accelerator LINAC 2, then by the proton-synchrotron booster PSB, the proton-synchrotron PS and the super proton-synchrotron SPS before being injected at 450 GeV into the Large Hadron Collider LHC itself. Figure is taken from [21]

A schematic picture of all components is given in Fig. 7, as they are structured in several layers around the interaction point. An more detailed overview on the various subsystems is given below.

3.2.1 Coordinate System

The common coordinate system used with CMS has its center in the collision point, with the y-axis pointing upward, the x-axis pointing radially inward towards the LHC ring and thus the z-axis pointing along the beam direction towards the Jura mountains. In radial coordinates, the azimuthal angle ϕ is measured in the x-y-plane, where the polar angle θ begins at the z-axis. Due to this choice of coordinate system, the momentum and energy transverse to the beam direction ($\mathrm{p_T}$, $\mathrm{E_T}$) are measured in the x-y-plane.

$$p_T^2 = p_x^2 + p_Y^2$$

Instead of using the angle θ, one uses the so called pseudorapidity

$$\eta = -\ln\left(\tan\left(\frac{\theta}{2}\right)\right)$$

as it is approximately equal to the rapidity in the case that the particle of interest is travelling close to the speed of light. Also, often one refers to the distance ΔR between two particles, which is defined by

$$\Delta R = \sqrt{(\Delta\eta)^2 + (\Delta\phi)^2}$$

where $\Delta\eta$ and $\Delta\phi$ are the corresponding individual differences between the particles in those coordinates.

3.2.2 The Detector Components

In this section, the various detector parts are described. As the CMS detector is structured in several layers around the interaction point, the desription of its parts of CMS is done in the same order. Preceeding is a short description of the magnet, which plays an important role in determining the charge and momenta of particles. The detector is typically divided into the cylindrical inner part (so called barrel region) and the forward parts (endcap region).

The Magnet

The superconducting solenoid magnet of the CMS detector provides a magnetic field of 3.8 Tesla in the inner detector, bending the tracks of charged particles. Therefore it is an important component for determining the charge and momenta of these particles. Surrounding the solenoid is an iron return yoke, which returns the magnetic flux and acts as a frame for the muon chambers.

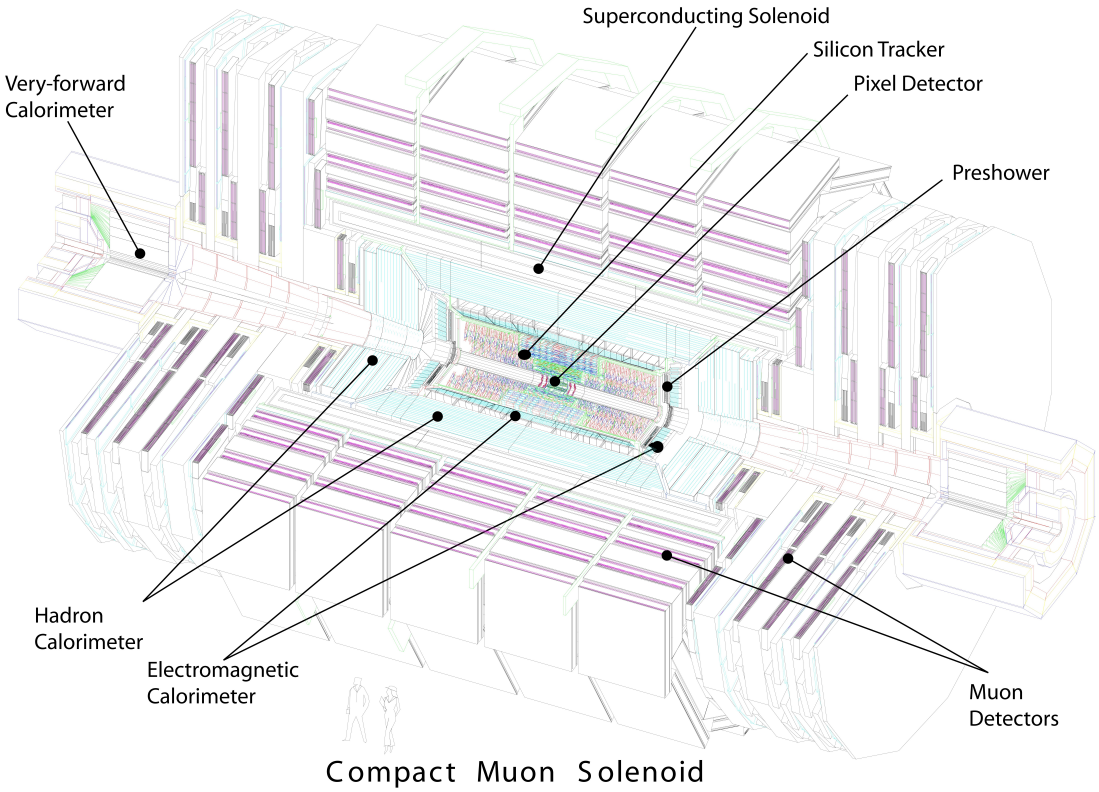

Figure 7: Perspective view of the CMS detector, taken from [18].

The Tracking System

The tracker is the innermost system of the CMS detector located directly around the interaction point. As one expects more than 20 overlapping proton-proton interactions per bunch-crossing at the design luminosity of 10^{34} cm^{-1} s^{-1} (every 25 ns), the tracker has to have a high granularity and fast response time. It consists of a pixel detector with three barrel layers and a silicon strip tracker with 10 barrel detection layers. In the endcap, there are two disks in the pixel detector and three plus nine disks in the strip tracker. The whole system covers an area in the pseudorapidity $|\eta|$ up to 2.5. For charged particles, the spatial resolution of the tracker reaches 15 - 20 µm [18]. A schematic view of the tracker is given in Fig. 8.

While this information is true for all data, which are used in this analysis, in the meantime, the CMS tracker was upgraded with a new pixel detector.

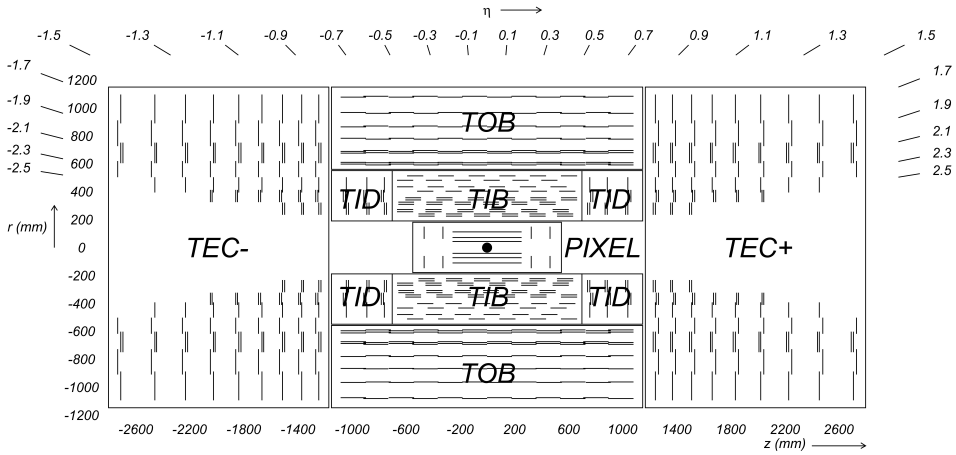

Figure 8: Schematic view of the tracker, consisting of the pixel, the tracker inner barrel and disk (TIB/TID), the tracker outer barrel (TOB) and the tracker endcaps (TEC+, TEC-, depending on z-axis). Figure taken from [18].

The Electromagnetic Calorimeter

The following subdetector is the electromagnetic calorimeter (ECAL). It consists of lead-tungsten crystals ($PbWO_4$), which have a high density (8.28 g/cm^3) and a short electromagnetic radiation length (0.89 cm). In the barrel, avalanche photodiodes and in the endcap, vacuum phototriodes are used. The whole system covers a range of $|\eta| < 3.0$ and it is hermetic and homogenous, which offers good energy resolution. A

typical energy resolution of the ECAL is given by [18]

$$\left(\frac{\sigma}{E}\right)^2 = \left(\frac{2.8\%}{\sqrt{E}}\right)^2 + \left(\frac{0.12}{E}\right)^2 + (0.30\%)^2$$

If the corresponding energy is not too high, photons and electrons are stopped within this system and their quantities are measured.

The Hadronic Calorimeter

The next layer in CMS is the hadronic calorimeter (or HCAL), which is designed to measure hadron jets and it is necessary to determine the missing transverse energy (MET). The HCAL is divided into four segments: the hadron barrel (HB), the hadron endcap (HE), the hadron outer (HO) and the hadron forward (HF) calorimeters. Its total coverage extends in η up to 5, their placement is shown in Fig. 9. This design is partly due to other systems enclosing it, e.g. the HB is fit between the outer extents of the ECAL and the inner extent of the magnet. In order to cover more interaction lengths of the hadrons (the HCAL shall contain the whole shower), the HO is placed outside the solenoid in the barrel region. The HO itself is restrained in size and placement by the muon system.

The HB and HE both consist of multiple layers of brass alternating with plastic scintillators. As it is located outside the solenoid, the HF has the solenoids material as additional absorber before it detects the showers with scintillators. The forward region uses Cherenkov-based detection methods.

As this thesis analyses light lepton final states, this subsystem is of less relevance for this analysis.

The Muon System

The CMS muon system is the outermost detection system of CMS, embedded in the iron return yoke of the magnet. It is used for muon identification, momentum measurement and triggering. It consists of three different detector systems. In the inner barrel region ($|\eta| < 1.2$) drift tubes (DT) are used, while in the outer regions and the endcap cathode strip chambers (CSC) are installed. The muon system covers a range up to 2.4 in $|\eta|$ with no acceptance gaps, as the different drift tubes and CSCs are offset with respect to each other. In addition to these, in both the barrel and the endcap region (for $|\eta| < 1.6$), resistive plate chambers (RPC) are used in the detector in order to provide a fast, independent trigger.

Drift Tubes

These 2.4 meter long tubes are filled with a mixture of gases (85% Argon, 15% carbon dioxide) with an anode wire in the (longitutinal) center of each tube. Cathode strips are located at the tube's walls. When a muon passes the gas-mixture, it ionizes the

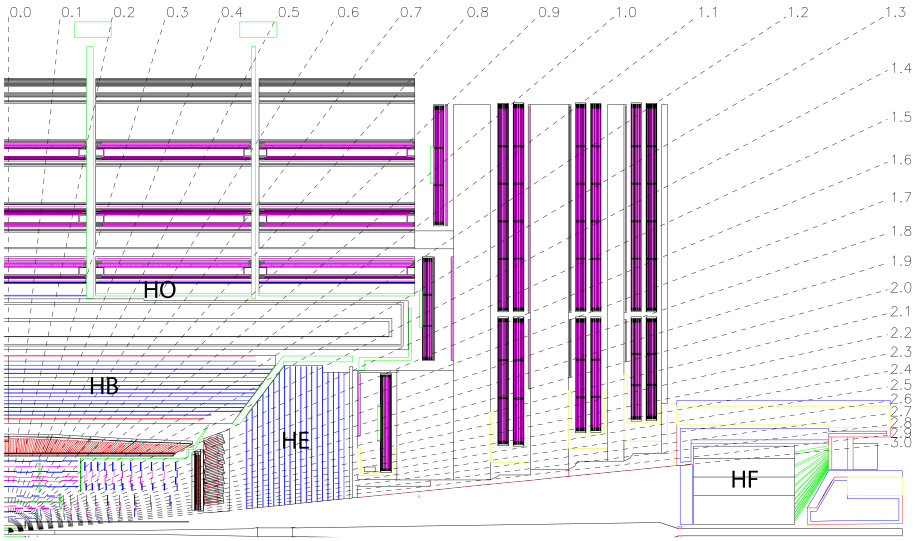

Figure 9: Longitudinal view of CMS to show placement of the various parts of the hadronic calorimeter. Figure taken from [18].

gas and creates a signal at both the anode and the cathode. By layering many of these tubes, a transversing muon can be measured and located.

Cathode Strip Chambers
In trapedoizal chambers radial to the beam axis, cathode strips are mounted. Perpendicular to those, in gas filled gaps, layers of anode wires are mounted. This setup is used to measure all components of a muon's trajectory in a non-uniform magnetic field (as it is in the endcaps).

Resistive Plate Chambers
Resistive plate chambers consist of several readout strips, located between plates with high electric resistance. Due to high voltage, a passing muon creates an avalanche of charged particles, which will then be measured. This process is very fast, so they are used for triggering.

Using those in conjunction with tracks from the tracker, a p_T-resolution better than 2.0% can be reached for barrel muons with a transverse momentum between 20 GeV and 100 GeV. For endcap muons with a transverse momentum below 1 TeV, this resolution is still below 10% [25].

3.2.3 The Trigger System

With a crossing frequency of 40 MHz, and several collisions happening per crossing, there is a such a large amount of data generated, that it is impossible to store it.

Therefore one needs a trigger mechanism, which drastically reduces the amount of data. At CMS, this is done in two steps:
The Level-One (L1) trigger consists of largly programmable electronics. It only uses coarsly segmented data from the calorimeters and the muon system. A schematic overview for the L1 trigger is given in Fig. 10. The L1-trigger only gets some rough information from the muon system and the calorimeters, but not from the tracker. These collected information are quickly evaluated, if the event is of any interest. This reduces the event rate to 30-100 kHz, which is recorded by the Data Acquisition (DAQ) system and then sent to the high level trigger for further processing.

After the L1-trigger comes the high level trigger (HLT), which is completely software based in a large computing center. All events which pass the L1 trigger are then processed by the HLT, using full information of an event, which gives more advanced selection options. The software starts with information taken from the L1 trigger, and then decides, if it fits to other recorded hits (e.g. from the tracker), to decide if it passes as a HLT object. At this point, some requirements are set for different trigger paths (e.g. whether it passes a single muon requirement, or a double electron requirement, and so on). Using this, data can be reconstructed and sorted, depending on their event content. The resulting data subsets are stored in so called 'data streams', with an event rate in the order of 100 Hz.

The LHC computing grid then sends the recorded data to computing centers all over the world for further reconstruction [26]. A copy of the original data is stored at CERN and Budapest (Tier 0), for reprocessing or rereconstruction. At Tier 1 computing centers, Monte Carlo simulated backgrounds are stored together with raw data for access on very large data samples for data-intensive analysis. Already processed data can then be used by an end-user on the Tier-2 computing centers, where they can be accessed together with simulated MC samples. Also, a large amount of Monte Carlo simulation is processed at these computing centers.

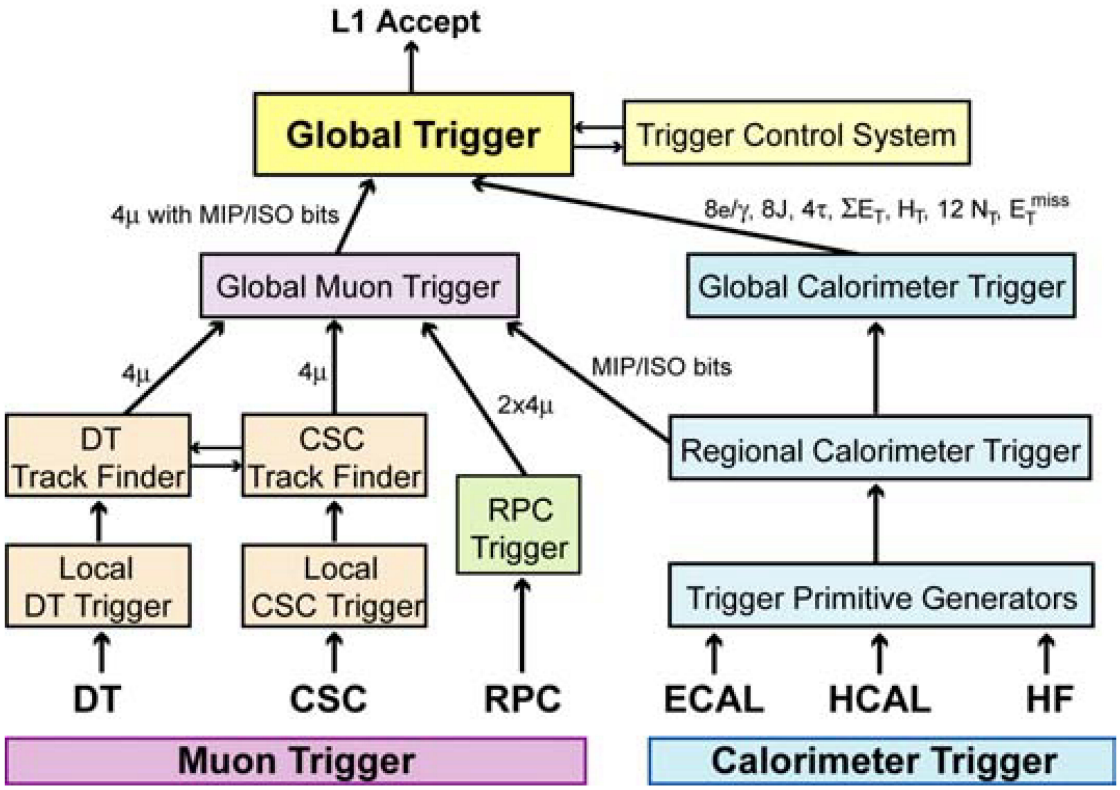

Figure 10: Schematic diagram for operation method of the L1 trigger. Figure taken from [18].

4 Analyzed dataset and Monte Carlo

In this section, all samples used for this analysis are briefly described. This includes the full 2016 dataset as well as the Monte Carlo based background prediction and signal sample generation. In the later analysis parts, these are compared and it is searched for differences between the predicted background and the measured data.

4.1 The 2016 Dataset

For this thesis, the whole 2016 CMS dataset at a center-of-mass energy of $\sqrt{s} = 13$ TeV with an intergrated luminosity of 35.9 fb^{-1} is analyzed. An overview of the datasets used, divided into their size (integrated luminosity), is shown in Tab. 1. The data has been certified by the CMS Physics Data and the Monte Carlo Validation group [27]. Only events, which are in the certified event list (called 'golden JSON' file), are used in this analysis.

As this analysis is interested in events with three of four light leptons, not all data is of interest. Only datasets, which were classified by the trigger (as explained in section 3.2.3) for either the DoubleMuon, the DoubleElectron or the MuonEG dataset, are used. For the purely muonic (electronic) channels, the DoubleMuon (DoubleElectron) dataset was used, while for the mixed channels, the MuonEG dataset was analyzed. The whole dataset corresponds to an integrated luminosity of 35.9fb^{-1}with an uncertainty of 2.5%, as given in [28].

4.1.1 Monte Carlo Simulation

Monte Carlo generation is often used in particle physics to simulate the full kinematics of a given process as well as calculating its cross section. Events are simulated by taking the theoretical prediction of the process, and imposing pseudo-random number generated distributions for the kinematics of the events. First, the hard scattering process is simulated. Afterwards, the parton shower of quarks and gluons is calculated,

Table 1: Data taking periods (electron and muon channels) in 2016 with the corresponding run periods, golden run ranges, integrated luminosity and data-set names.

Period	Run	Golden Runs	Integrated lumi	dataset
1	Run B	273158-275376	5.79fb^{-1}	Run2016B-03Feb2017-v3
2	Run C	275657-276283	2.57fb^{-1}	Run2016C-03Feb2017-v1
2	Run D	276315-276811	4.25fb^{-1}	Run2016D-03Feb2017-v1
2	Run E	276831-277420	4.01fb^{-1}	Run2016E-03Feb2017-v1
2	Run F	277981-278808	3.10fb^{-1}	Run2016F-03Feb2017-v1
3	Run G	278820-280385	7.54fb^{-1}	Run2016G-03Feb2017-v1
3	Run H	281613-283685	8.61fb^{-1}	Run2016H-03Feb2017-v2,3

which in turn enters the hadronization (forming of hadrons). Afterwards, the response of the detector is simulated by GEANT4 [29]. In order to get a good description of the physical process, this procedure is repeated a large amount of times to get a large set of possible outcomes of the event generation.

To get the correctly normalized background prediction for this analysis, the background has to be scaled to the measured integrated luminosity, which is done by applying a weight of the form

$$w = \alpha \cdot \frac{L_{\text{data}}^{\text{int}} \cdot \sigma}{N_{\text{events}}^{\text{background}}}$$

Note, that α is an additional factor, which includes some form of correction, which will be explained later (see section 5.6).

There are different types of Monte Carlo (MC) simulating programs, each with different features. In this thesis, the following generators are used: POWHEG [30, 31], Pythia8.2 [32] and aMC@NLO [33].

The event is, depending on the generator used, calculated at leading order (LO) or next-to-leading order (NLO) precision. In case the cross section of a calculated process is more precisely known (due to theoretical predictions) than the calculation of the generator results in, it can be corrected by a so called 'k-factor', which is defined by:

$$k = \frac{\sigma(\text{higher order})}{\sigma(\text{generated order})}$$

4.1.2 Expected Backgrounds

In this chapter, all expected Standard Model backgrounds are briefly described. Of interest are final states with three or four light leptons (3ℓ and 4ℓ category). There are two possible ways of measured leptons: prompt and fake leptons. Prompt leptons are real leptons coming from the decay of particles, while 'fake leptons' is used to describe high-energy jets, which leave an extremely similar track in the detector as a normal lepton, and are therefore misidentified as such. Although jets may contain leptons, these are non-prompt particles, which are not well isolated. For the most dominant backgrounds, Feynman diagrams are given in Fig. 11 and 12.

- **Z-pair production**: For the 4ℓ categories, the most relevant background is the ZZ pair production, where two Z bosons are created. Both decay to two leptons, giving the exact final state of the signal. Z pair production happens on leading order via quark-quark or quark-gluon interaction, the next-to-leading order process of gluon-gluon fusion going to ZZ is also included. The former background was produced with POWHEG 2.0 at NLO and the cross section is scaled to match the next-to-next-to-leading order cross section [34], while the gluon-fusion background is created with MCFM at LO and the cross section is scaled to match the NLO cross section [35].

- **WZ production**: The associated creation of a W and a Z boson, which both decay leptonically and therefore resulting in three leptons, giving the final state of the 3ℓ categories. If jets are in the same event and one jet is misidentified as a lepton, it can also enter the 4ℓ categories.

- **Drell Yan (DY)**: The production of a Z boson in conjunction with jets can be an important background. If the Z decays into two leptons, and a jet can be misidentified as another one, this results in the same final state as the 3ℓ categories. An additional contribution from this background can occur, if a high-energy photon is emited during this process (then often referred to as $Z\gamma$). This photon can in turn convert to two additional leptons, which (with the ones of the Z boson) can produce the 4ℓ final state. Additionally, high energy photons are likely to fake electrons, as the detector response is very similar for these two particles.

- **Top pair production**: When a top pair is produced, both top quarks decay to b-quarks and emit a W-boson. The latter one can decay to a lepton and a neutrino (giving two neutrinos and two leptons). In addition to jets, which can fake leptons, it can reproduce any final state of the analysis.

- **ttX background**: When a top pair is produced in cunjunction with a Z or W boson, it can simulate final states of both the 4ℓ and the 3ℓ search categories.

- **Higgs production**: The creation of a Higgs, which in turn decays to two Z bosons, decaying to four leptons and resulting in the final state of the 4ℓ categories is also included. All production mechanisms of the Higgs (gluon-fusion, vector boson fusion and associated production with a W-boson) are taken into account.

- **tZq background**: If a Z is produced in conjunction with a top quark and other quarks, the top decays to a W-boson, producing a similar background as WZ-production.

- **Triboson**: The production of three heavy bosons is quite rare (small cross section), but is capable of producing the same final state in both the 3ℓ and 4ℓ categories. All of WWW, WWZ, WZZ and ZZZ production is included.

All these backgrounds are simulated via Monte Carlo. The specific names and cross sections of the used background samples are given in Tab. 2. In order to improve statistics, for some background processes, several samples were used. These samples are binned in terms of the invariant mass of the resulting lepton pair (e.g. for DY the mass of the Z boson.). Any overlap between these samples has been removed.

4.1.3 Signal Generation

The signal Monte Carlo was generated with Pythia8 at leading order for both the creation of a μ^* as well as an e^*. The value of the compositeness scale Λ for these

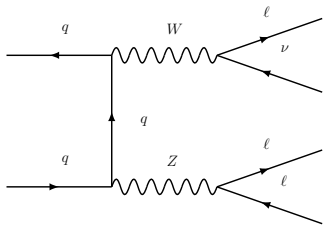

WZ production.

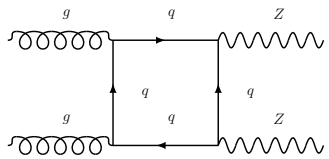

ZZ via gluon-fusion.

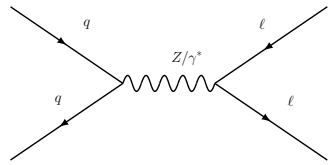

Drell-Yan process.

Figure 11: Feynman diagrams of Diboson production, gluon-fusion resulting in two Z bosons and the Drell-Yan process.

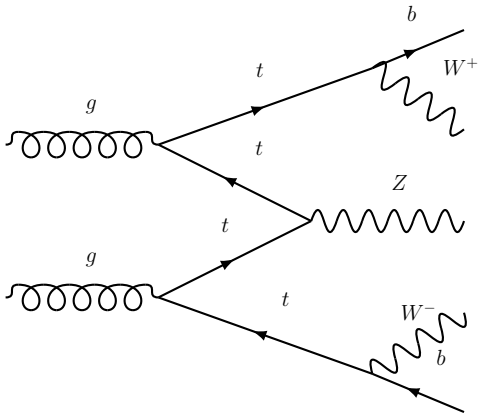

$t\bar{t}Z$ process.

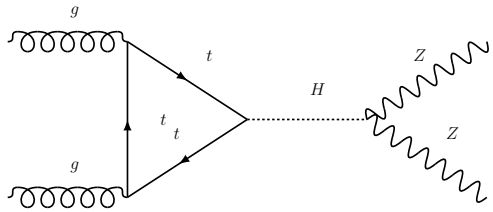

Creation of Higgs, decay to ZZ.

Figure 12: Feynman diagrams of top pair production (+X), and Higgs production via a top loop.

Table 2: Overview of Monte Carlo samples used to simulate the expected background. Overlap between samples has been removed. The 'order' column describes the order of the cross section, when the weight is applied.

	Background	Generator	Order	σ (pb)	weight
qq/qg→ZZ	ZZTo4L	POWHEG	NNLO	1.212	1.1
	ZZTo2L2Nu	POWHEG	NNLO	0.5644	1.1
	ZZTo2L2Q	aMC@NLO	NNLO	3.22	1.1
gg→ZZ	GluGluToContinToZZTo4tau	MCFM	NLO	$1.586 \cdot 10^{-3}$	1.7
	GluGluToContinToZZTo4mu	MCFM	NLO	$1.586 \cdot 10^{-3}$	1.7
	GluGluToContinToZZTo4e	MCFM	NLO	$1.586 \cdot 10^{-3}$	1.7
	GluGluToContinToZZTo2e2mu	MCFM	NLO	$3.194 \cdot 10^{-3}$	1.7
	GluGluToContinToZZTo2e2tau	MCFM	NLO	$3.194 \cdot 10^{-3}$	1.7
	GluGluToContinToZZTo2mu2tau	MCFM	NLO	$3.194 \cdot 10^{-3}$	1.7
$t\bar{t}$	TTTo2L2Nu	POWHEG	NNLO	87.31	1.0
	TTTo2L2Nu MLL-500-800	POWHEG	NNLO	0.3259	1.0
	TTTo2L2Nu MLL-800-1200	POWHEG	NNLO	0.03263	1.0
	TTTo2L2Nu MLL-1200-2500	POWHEG	NNLO	$3.051 \cdot 10^{-3}$	1.0
	TTTo2L2Nu MLL-2500-Inf	POWHEG	NNLO	$1.747 \cdot 10^{-4}$	1.0
	TTZToLLNuNu	aMC@NLO	NNLO	0.2529	1.0
	TTWJetsToLNu	aMC@NLO	NNLO	0.2043	1.0
Drell Yan	DYJetsToLL M-50	aMC@NLO	NNLO	5765.4	1.0
	DYJetsToLL M-10to50	aMC@NLO	NLO	18610	1.0
	DYJetsToLL M-400to500	aMC@NLO	NLO	0.423	1.0
	DYJetsToLL M-500to700	aMC@NLO	NLO	0.24	1.0
	DYJetsToLL M-700to800	aMC@NLO	NLO	$3.5 \cdot 10^{-2}$	1.0
	DYJetsToLL M-800to1000	aMC@NLO	NLO	$3.0 \cdot 10^{-2}$	1.0
	DYJetsToLL M-1000to1500	aMC@NLO	NLO	$1.6 \cdot 10^{-2}$	1.0
	DYJetsToLL M-1500to2000	aMC@NLO	NLO	$2.0 \cdot 10^{-3}$	1.0
	DYJetsToLL M-2000to3000	aMC@NLO	NLO	$5.4 \cdot 10^{-4}$	1.0
Other Diboson	WWTo1LNuQQ	aMC@NLO	NNLO	49.997	1.0
	WZTo2L2Q	aMC@NLO	NLO	5.595	1.0
	WWTo2L2Nu	POWHEG	NNLO	12.178	1.0
	WZTo3LNu	POWHEG	NLO	4.42965	1.0
Other processes	VBF HToZZTo4L	POWHEG	NLO	$1.034 \cdot 10^{-3}$	1.0
	WminusH HToZZTo4L	POWHEG	NLO	$1.471 \cdot 10^{-4}$	1.0
	WplusH HToZZTo4L	POWHEG	NLO	$2.339 \cdot 10^{-4}$	1.0
	GluGlu HToZZTo4L	POWHEG	NLO	$1.212 \cdot 10^{-2}$	1.0
	WWW	aMC@NLO	NLO	0.2086	1.0
	WWZ	aMC@NLO	NLO	0.1651	1.0
	WZZ	aMC@NLO	NLO	$5.565 \cdot 10^{-2}$	1.0
	ZZZ	aMC@NLO	NLO	$1.398 \cdot 10^{-2}$	1.0
	tZq	aMC@NLO	NLO	$7.58 \cdot 10^{-2}$	1.0

samples is 10 TeV. The samples were created with 50000 events per sample for various excited lepton mass points. An overview of the cross sections per mass for the chosen Λ is given in Tab. 3. For both processes, the contact interaction decay $\ell\ell^* \rightarrow \ell\ell\ell'\ell'$ with $\ell = e, \mu$ and $\ell' = e, \mu, \tau$ was simulated. Note, that this search only includes light lepton (e, µ) channels, and thus is unable to reconstruct the τ. Although it might happen, that, if a τ decays into a muon or electron and the other decays hadronically, the event still enters the selection.

4.1.4 Signal Characteristics

In this section, the kinematics and characteristics of the excited lepton signals are analysed to search for methods to distinguish it from the expected background. The signal produces multi-lepton final states with four leptons. For a generated e^*, these are the 4e, the 2e2µ and the 2e2τ final states, while for a generated μ^*, they are the 4µ, the 2e2µ and the 2µ2τ final state.

The final states containing τ leptons are not analyzed explicitely in this thesis, although there is a point to be made on these final states. Taking into account the fast decay of the τ lepton, the detector can measure two and more leptons. Two, in case the created τ leptons both decay hadronically and three leptons, if one τ decays hadronically. All other possibilities lead to a final state with some combination of electrons and muons. Of those combinations, both '3+1'-combinations ($3e1\mu$ and $1e3\mu$, if two τ leptons are created and one decays into a muon and the other decays into an electron) are rare as the branching ratio of a τ decaying leptonically is only 34% (17% per lepton). These search categories are neglected in this analysis as they are to rare to improve the sensitivity of this search. The remaining 4ℓ final states and the corresponding 3ℓ final states are analysed. All these decay possibilites are simulated in the used signal samples.

The three-leptonic final states are of interest, not only because some events with τ leptons are covered, but more importantly because a significant amount of signal can be recovered in these categories if one of the leptons from the 4ℓ-categories is not reconstructed correctly or falls out of the acceptance. The inclusion of the 3ℓ search category is especially valuable for the electron final states (this is shown later 5.3).

The basic coordinate distributions of the leptons for the signals are shown for muons in Fig. 13 and for electrons in Fig. 14. As these plots use information from generator level, there is no difference (apart from statistical effects). This is due to the fact, that the major difference between electron and muons is their mass, which can be neglected at these energy scales.

In the distributions, it can be seen, that for a higher generated mass, the mean p_T increases and the width in η decreases, which is expected, as the decay products have a more central flight direction. As the acceptance of the detector does not cover the whole η-range, some leptons will be lost by default. All these distributions show information from the generator level, so resolution effects of the detector are not included at this point. It is also interesting to have a look into the generated mass of the ℓ^*. For very

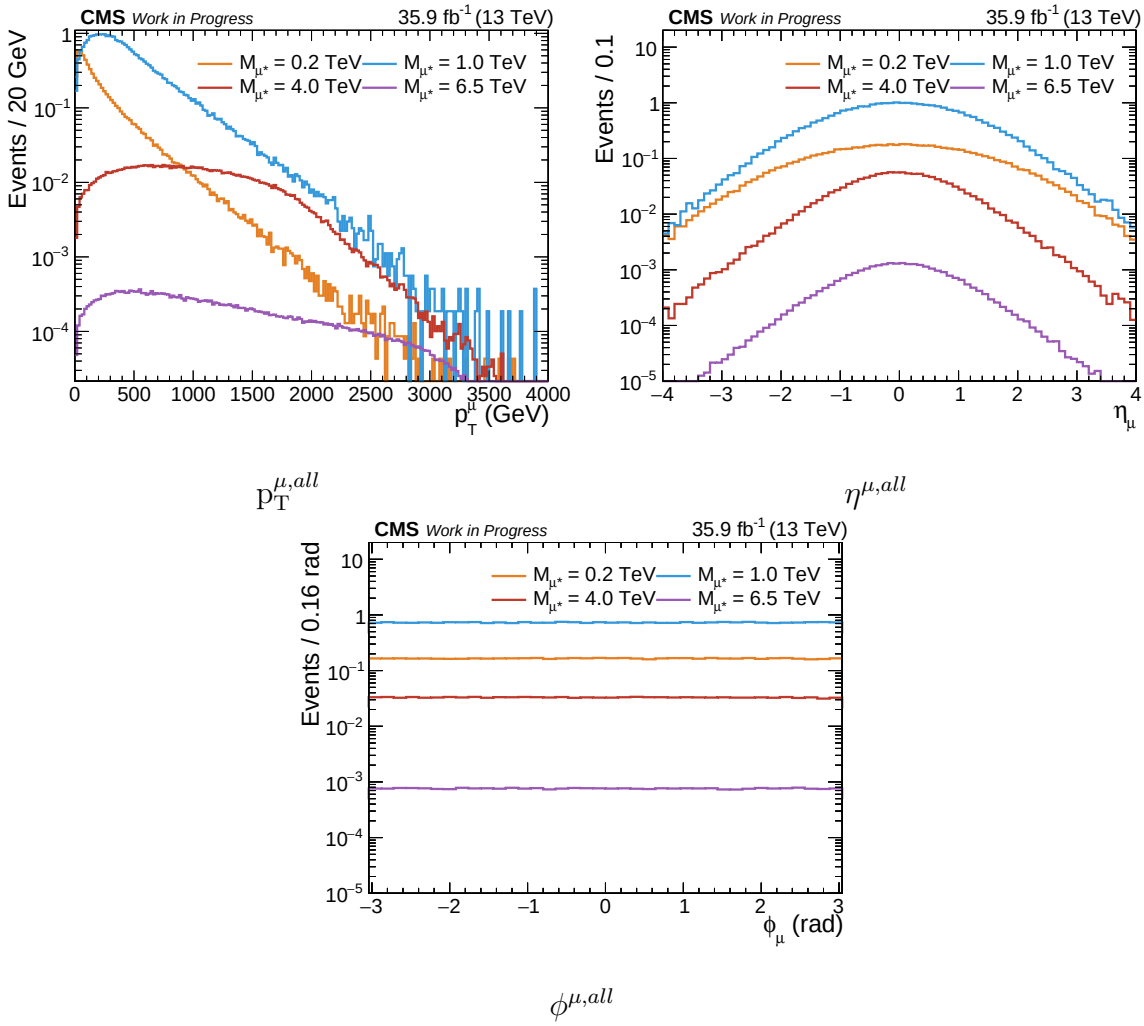

Figure 13: Distributions of basic properties of muons for various signal samples. For each distribution, all generated muons per event are filled. As can be seen, some muons are outside the acceptance of the detector ($|\eta| > 2.4$), so they are not recognized when reconstructing the event. All these distributions are calculated on μ^* samples, and they are scaled to their corresponding theory cross section for $\Lambda = 10$ TeV.

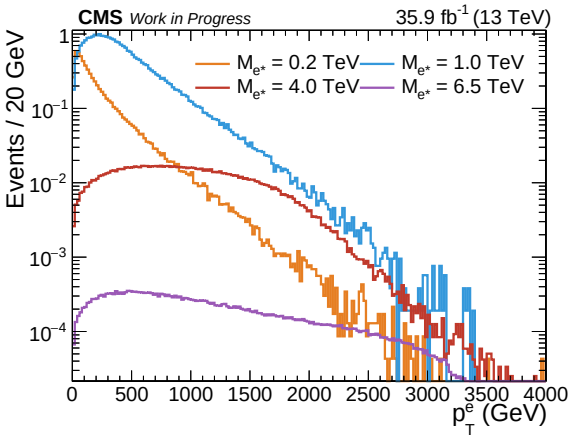

$p_T^{e,all}$

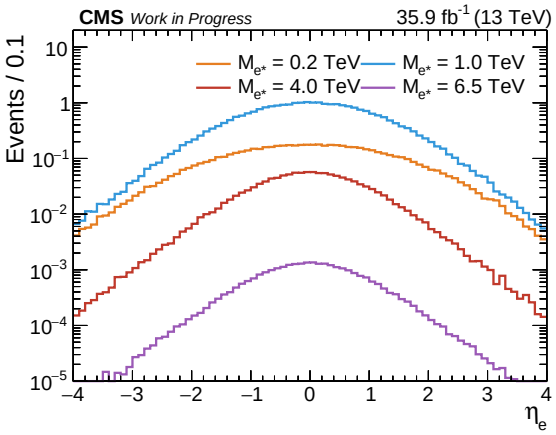

$\eta^{e,all}$

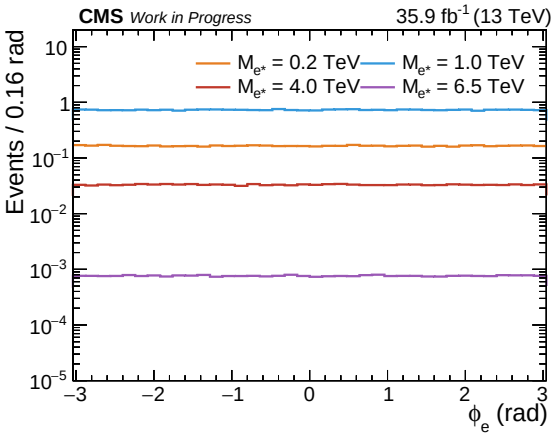

$\phi^{e,all}$

Figure 14: Distributions of basic properties of electrons for various signal samples. For each distribution, all generated electrons per event are filled. Also here, some electrons are outside the range of the ECAL ($|\eta| > 2.5$) and will therefore be lost. These distributions are calculated on e^* samples, and they are scaled to their corresponding theory cross section for $\Lambda = 10$ TeV.

Table 3: Overview of the generated samples (50000 events each) with the LO cross section given for the compositeness scale of $\Lambda = 10$ TeV. The choice of Λ mainly scales the cross section and does not have a significant impact on the signal shape.

ℓ^* mass (GeV)	$\sigma \times BR$ (pb); $\Lambda = 10$ TeV	ℓ^* mass (GeV)	$\sigma \times BR$ (pb); $\Lambda = 10$ TeV
200	$5.995 \cdot 10^{-5}$	3000	$4.894 \cdot 10^{-5}$
500	$1.726 \cdot 10^{-4}$	3500	$2.451 \cdot 10^{-5}$
750	$2.367 \cdot 10^{-4}$	4000	$1.172 \cdot 10^{-5}$
1000	$2.605 \cdot 10^{-4}$	4500	$5.358 \cdot 10^{-6}$
1250	$2.533 \cdot 10^{-4}$	5000	$2.408 \cdot 10^{-6}$
1500	$2.261 \cdot 10^{-4}$	5500	$1.105 \cdot 10^{-6}$
2000	$1.538 \cdot 10^{-4}$	6000	$5.17 \cdot 10^{-7}$
2500	$9.037 \cdot 10^{-5}$	6500	$2.67 \cdot 10^{-7}$

high masses, it becomes more and more likely for the ℓ^* to be produced 'off-shell', which means, that it does not have its original mass, but a significantly different mass. Also, the width of the distribution increases with higher generated mass and decreases with higher Λ. This is shown in Fig. 15.

If one uses the reconstructed mass of the corresponding excited leptons (e^*, μ^*), a more significant difference between electron and muon channels is visible. This is done by selecting the leptons from the decay of the generated ℓ^* and using their properties after reconstruction, taking effects of detector resolution into account (the way it would be reconstructed, if one would know the correct leptons to recombine). The mass of the ℓ^* reconstructed is shown in Fig. 16. As one can see, the distributions are wider for muons, which is due to the fact that electrons have a better resolution than muons in the CMS detector (as for muons, the momentum is determined from the sagitta of the track, as the particle does not deposit all its energy inside the detector).

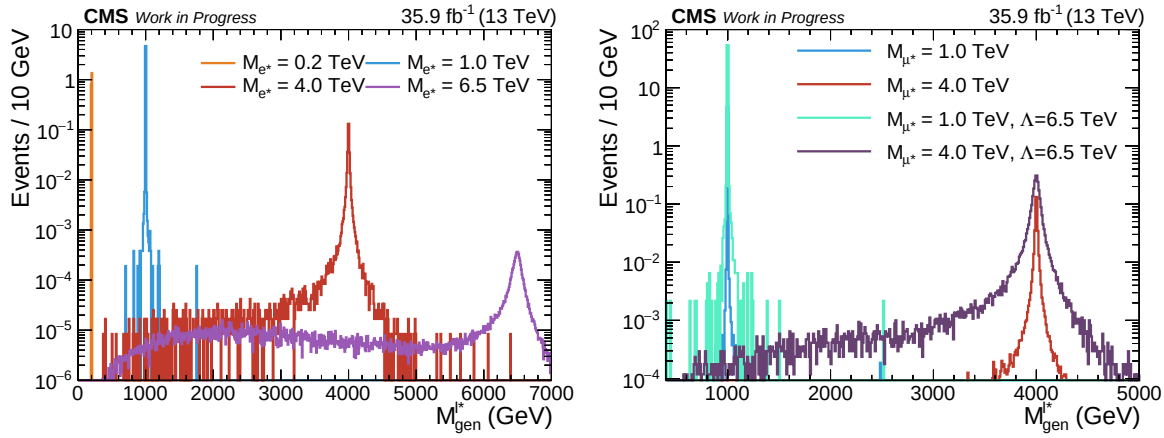

Figure 15: Generated mass of some samples for the case of the e^*. For μ^*, this is similar. What can be seen is that for high mass samples, offshell production becomes more likely. To show the influence of Λ on this distribution, on the right side, the distribution is shown for samples with $\Lambda = 10$ TeV and $\Lambda = 6.5$ TeV.

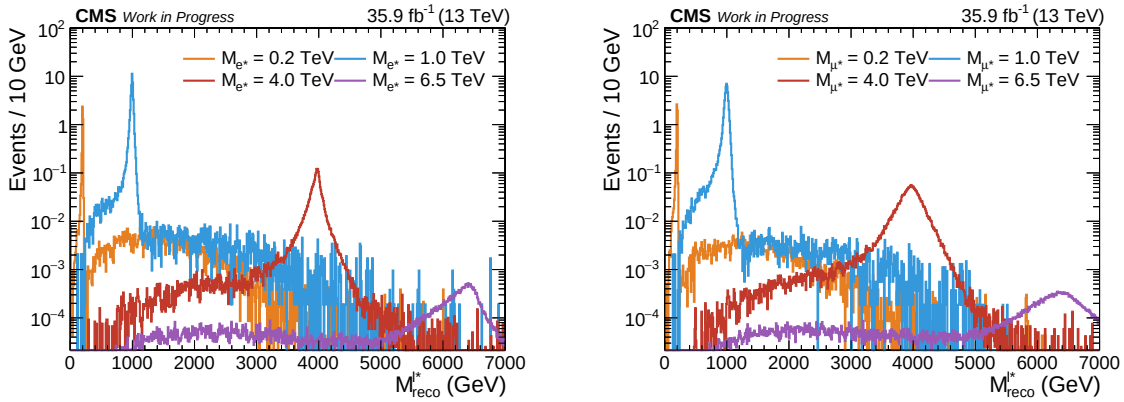

e^* μ^*

Figure 16: Reconstructed ℓ^* mass, if reconstructed leptons are matched to those generated (and coming from the decay of the ℓ^*). As muon resolution is worse that electron resolution in CMS, the width of the distribution is slightly smaller for the electron case.

5 Analysis

The analysis contains seven different channels (4ℓ-categories: $4e$, $2e2\mu$, 4μ; and 3ℓ categories: $3e$, $2e1\mu$, $1e2\mu$, 3μ), all exclusive to their corresponding light-lepton event content. E.g. the 3μ event class contains only events with exactly three muons and no electron. One should note that only the number of light leptons is specified, the event can contain any number of other particles (photons, jets, etc.). A large part of the events in the 3ℓ categories are those, where a single lepton from the 4ℓ categories is outside the acceptance or does not meet the reconstruction requirements. As the background in these search categories, although being significantly different, can be coped with, the inclusion of these categories increases the overall sensitivity of the search. For the 4ℓ category, the main expected background comes from the Z-pair production, while for the 3ℓ category, WZ-background becomes more important. In order to avoid a bias towards the signal, this analysis was designed as a blinded analysis. Therefore, a control region was defined, which was used to check for good analysis flow.

The first section of this chapter explains how an event was selected and what needs to be fulfilled for it to be further analyzed. Afterwards, an overview of how the light leptons are reconstructed in each event and the subsequent categorization of those events in the seven search categories of this analysis. Then, further steps are introduced to increase the sensitivity of this search. A control region is defined and shown at the end of this chapter.

5.1 Event Selection

In order for an event to be analyzed, it needs to pass a certain trigger. As this analysis is interested in multilepton final states (with three or four light leptons), double-lepton triggers are used, as they have low p_T-thresholds and high efficiency. Depending on the analysis channel, different sets of triggers were used (with a logical OR between them, in case of more than one trigger). The different trigger paths are as follows:

- 4e and 3e

  Trigger: A combination of a double-electron trigger, where both electrons have to fulfil $p_T > 33$ GeV, and a double-electron trigger, where the leading electron has to fulfil $p_T > 23$ GeV and the second electron has to fulfil $p_T < 12$ GeV, is used. As the triggers have slightly different identification requirements, the inclusion of both is helpful[1].

  Offline p_T-cut: Leading and subleading electron have to have $p_T > 35$ GeV

- 2e2μ, 1e2μ and 2e1μ

  Trigger: The trigger requires either an electron or a muon with a transverse momentum of at least 37 GeV. The other correspoding particle has to have a

[1] HLT_DoubleEle33_CaloIdL_GsfTrkIdVL_MW, HLT_Ele23_Ele12_CaloIdL_TrackIdL_IsoVL_DZ

$p_T > 27$ GeV. For both particles, some loose identification requirements must be met[2].

Offline p_T-cut: Leading electron and leading muon have to have $p_T > 40$ GeV

- 4µ and 3µ

  Trigger: For the muonic channels, a trigger which requires the leading muon to have a transverse momentum of at least 30 GeV and the subleading muon to fulfil $p_T > 11$ GeV[3].

  Offline p_T-cut: Leading muon has to have $p_T > 35$ GeV, subleading muon $p_T > 20$ GeV

As these triggers have slightly different p_T thresholds, the corresponding offline p_T-cut varies between different categories. This p_T-cut is imposed slightly higher than the trigger threshold in order to avoid the turn-on of the trigger efficiency. This is necessary, as the description of simulation in the region of the trigger turn on is not in agreement with data.

For triggers on electrons, it is required that the candidate fulfils a loose calorimeter-based electron identification (CaolIdL) and depending on the trigger either a loose tracker based identification (TrackIdL) or a very loose Gaussian sum filter driven tracker based identification (GsfTrkIdVL). In addition, the HLT_Ele23_Ele12-trigger requires a very loose isolation (no other particles in a small cone around the electron candidate). Note, that all these triggers were active for the whole period of proton-proton collision data taking in 2016. By imposing these triggers and additional p_T cuts, some signal is lost. This efficiency loss is smaller than one percent and slightly higher for low mass samples, which is shown in the appendix 8.1.

[2] HLT_Mu37_Ele27_CaloIdL_GsfTrkIdVL, HLT_Mu27_Ele37_CaloIdL_GsfTrkIdVL
[3] HLT_Mu30_TkMu11

5.2 Object Reconstruction

As explained, this analysis searches for anomalies in light lepton spectra. In order to do this, the physical objects of electron and muon need to be reconstructed. This is explained in this section.

5.2.1 Electrons

Electron reconstruction uses information from the tracker as well as the electromagnetic calorimeter. A complex algorithm called 'particle flow' algorithm [36] is used, which uses different techniques and imposes some isolation criteria to distinguish better between electrons and jets (the algorithm can be used to reconstruct all types of measurable particles in the detector, but is only used for electrons here). Seeds determined from ECAL superclusters (which describes the cluster of crystals hit by an electron and its photons created by bremsstrahlung) are especially well fit for isolated electrons. For tracker based electrons, a preselection based on the number of hits and the fit's χ^2 is applied and the selected tracks are fit again with a Gaussian-sum filter (GSF) [37]. Those information are then combined to a collection, where the tracks are combined and used to identify the electrons.

After this reconstruction, some identification criteria are imposed to ensure high-quality selection of electrons. For this analysis, the cut-based loose electron ID is used [38]. It uses information about the shape and size of a candidate particle's supercluster, namely the width in η and ϕ ($|\Delta\eta_{in}|$, $|\Delta\phi_{in}|$) and the spread in the ECAL ($\sigma_{i\eta i\eta}$). The ID also takes the electron's relative deposited energy in ECAL and HCAL (as electrons are expected to deposit most of their energy in the ECAL) into account. To ensure isolation of the electrons, the isolation requirement of the particle flow algorithm is used with a correction applied based on the effective area of the reconstructed electron.

In addition to the ID, due to the layout of the tracker with a coverage up to $|\eta| < 2.5$ and conversion pipes for cooling in a range of $1.4442 < |\eta| < 1.556$, only electrons with η-values not influenced by these are used for this analysis. All electrons are required to have a p_T larger than 20 GeV in order to ensure good reconstruction of those particles. This cut also looses some efficiency in signal reconstruction, which is mostly in the order of 1%. For low mass samples, the loss is more significant at around 10 %, which can be seen in the appendix 8.1.

5.2.2 Muons

Muon Reconstruction

Muons in CMS are reconstructed with two independent, different approaches. One is the 'global muon' reconstruction, which is performed 'outside-in' (in terms of detector direction), while the 'tracker muon' reconstruction fits 'inside-out'. Information on reconstruction is taken from [39–41]. As the muon system covers up to $|\eta|$ of 2.4, only muon candidates with smaller values are accepted.

Table 4: Definitions of the selection cuts for the cut-based (CB) Loose ID.

Variable	Barrel cut	Endcap cut
$\sigma_{i\eta i\eta}$	< 0.011	< 0.0314
$\lvert\Delta\eta_{in}\rvert$	< 0.00477	< 0.00868
$\lvert\Delta\phi_{in}\rvert$	< 0.222	< 0.213
H/E	< 0.298	< 0.101
Rel. comb. PF iso with EA corr	< 0.0994	< 0.107
$\lvert 1/E - 1/p\rvert$	< 0.241	< 0.14
exp. missing inner hits	≤ 1	≤ 1
pass conversion veto	yes	yes

Basis of global muon reconstruction is the 'standalone muon' (S/A muon) reconstruction. This uses only information from the muon chambers, taking initial trajectory estimates formed by matching pairs of local DT and CSC segments as a seed. Based on this seed, a fit using the Kalman technique [42] is performed along all CSC, RPC hits and DT segments along the trajectory. Afterwards, additional Kalman smoothing is applied to equalize the fitted track errors. This method alone has a high reconstruction efficiency and a momentum resolution of approximately 10% for muons with a transverse momentum of up to several TeV [41].

The global muon reconstruction method then uses these S/A muons as a seed and searches for matching tracks in the detector. A Kalman fit is performed, using the track candidate hits and the hits from the standalone muon. The candidate with the best fit probability is selected as a global muon. Using the additional information from the tracker, this method improves the transverse momentum resolution to around 1% for muons with a momentum of up to 1 TeV [43].

The tracker muon reconstruction method instead starts with the collection of all reconstructed tracks in the tracker. These tracks are extrapolated outwards and use the energy deposition in the crossed cells from the ECAL, HCAL and HO as well as information from muon segments close to the extrapolation (distance between extrapolation and chamber edges is taken into account). Afterwards, several quality cuts are imposed to give good muon hadron separation.

The muon pT is determined using the 'TuneP' algorithm, a specific cocktail of different algorithms existing to reconstruct the muon p_T, optimized for the special case of high-pT muons. For low-p_T muons (< 200 GeV), only the result of the tracker-fit is used to determine the transverse momentum. For high-energy muons, this is not feasible, as the tracks become more straight, making it harder to determine the momentum. Therefore, it is necessary to include hits from the muon chambers to determine the p_T. As those muons have a large likelihood of interacting with the iron return yoke of the magnet, it can happen, that additional hits in the muon system are measured, which do not come directly from the actual muon. In order to account for these effects, several algorithms have been developed:

- **Tracker-Plus-First-Muon-Station (TPFMS)**: This method only accounts for hits in the first muon station (the innermost one), when calculating the fit to the track. This is useful for muons which emit a bremsstrahlung photon while passing the muon system, which can smear the track.

- **Picky Fit**: This is most useful for cases, when there are multiple close-by hits in the muon chambers. Depending on the χ^2-variation of the fit, additional hits, which are not compatible, are removed.

The used *TuneP* or *cocktail* algorithm uses a mix of these different reconstruction methods (tracker-only, TPFMS, Picky), in order to benefit of the different advantages of these methods. This algorithm determines the muon momentum using the best fit from the different reconstruction algorithms, based on the corresponding goodness of the fit. This TuneP-reconstruction method is used for all muons in this analysis.

Muon Identification

Additional identification criteria can be used, to differentiate between well reconstructed muons and 'fake' muons. The latter one are particles, that also pass the muon reconstruction, but are either non-prompt non-isolated muons or high-energy hadrons. The latter ones can pass through the whole HCAL and therefore are measured in the muon system ('punch-through'). The different identification criteria are developed by the CMS muon group and are commonly used in all analyses.

For this analysis, the dedicated high-p_T muon ID, which is recommended for muons with high transverse momentum, is used. This specifies an object, in order to be identified as a muon, to have the following properties [44]:

- The candidate has to be reconstructed as a global muon.

- The object has to have at least passed two muon stations, which reduces accidental matching of tracks.

- After the global muon's track was fitted, at least on muon-chamber has to be hit by its track, in order to avoid hadronic punch-through and muons from decays in flight.

- In order to avoid bad reconstruction, the relative error on the transverse momentum of the best muon track has to be smaller than 0.3.

- The longitudinal distance of the tracker track with respect to the primary vertex d_z has to be smaller than 5 mm, in order to further suppress cosmic muons and to avoid tracks from pileup.

- The transverse impact parameter d_{xy} with respect to the primary vertex has to be smaller than 5 mm, in order to further suppress muons from decays in flight and to suppress cosmic muons.

- At least one pixel has to be hit, which also reduces contributions from in-flight decay muons.

- In order to guarantee a good $\mathrm{p_T}$ measurement of the object, the number of tracker layers with hits has to be larger than five.

In addition to these identification criteria, this analysis requires an additional isolation requirement for each muon. It is defined by taking all tracks around the muon track in a cone of $\Delta R < 0.3$, and requiring that the relative momentum of the muon compared to those track's momenta is smaller than 0.1:

$$\frac{\sum p_T^{tracker}}{p_T^{\mu}} < 0.1$$

This further reduces any contribution from jets.

5.3 Kinematic Selection

At this point, all events are selected and categorized into the seven channels. An overview of all cuts per channel up to this point is given in Tab. 5.

In order to distinguish the signal from the background, some selection based on the kinematics of the signal and the background is imposed. As most of the expected background includes a Z boson, while the signal does not, a Z veto is used. In each category, all possible same-flavour, opposing charge-sign lepton combinations are computed (so either a $\mu^+\mu^-$- or a e^+e^--combination). If one of these combinations ($m_{\ell\ell}$) has an invariant mass in the range of $m_Z \pm 15$ GeV (or 76 GeV $\leq m_{\ell\ell} \leq$ 106 GeV, $m_Z \approx 91$ GeV [1]), the event is used for the control region, as little to no signal contamination is expected. This is shown exemplarily for the 4e and the 1e2μ category in Fig. 17, all others can be found in the appendix 8.2. Note, that per event, only the two-body mass closest to $\mathrm{m_Z}$ is filled. Therefore, one would expect a peak in the distribution for signals, too (as the closest mass is plotted). But as the signal is not explicitely requiring a Z boson, instead an almost uniform distribution is seen, as shown in Fig. 18. The fact, that only very few signal events are vetoed by this cut makes it interesting to use as a control region (see section 5.5).

In Fig. 18 and similar distributions, the interesting variable (here, the invariant mass of two leptons, which is closest to the Z bosons mass) is shown on the x-axis. On the y-axis, the number of events per bin is shown. Data points are indicated as black dots (with their corresponding errors) and signal samples shown as outlined histograms (a different histogram per signal sample. Backgrounds are shown as stacked histogram, where background processes are indicated by different colors in this stack.

If there are data points included, a ratio plot is provided in addition to the normal distribution. In this subfigure, the ratio of data and background expectation is shown in addition to the statistical error band coming from the Monte Carlo prediction. An example for this can be seen in Fig. 22.

Table 5: Overview of all cuts for each search category. The number of light leptons refers to particles, which fulfil the earlier cuts and is meant exclusively (an event with three electrons constructed in this way only enters the 3e-category, not the 4e one, although technically the latter has three electrons aswell).

Channel	4e	3e	1e2µ	2e2µ	2e1µ	3µ	4µ
$p_T^{\ell,all}$ (GeV)	>20						
$p_T^{\mu,highest}$ (GeV)	—	—	> 40	> 40	> 40	> 35	> 35
$p_T^{\mu,2nd}$ (GeV)	—						
$p_T^{e,highest}$ (GeV)	> 35	> 35	> 40	> 40	> 40	—	—
$p_T^{e,2nd}$ (GeV)	> 35	> 35	—	—	—	—	—
$\eta^{\mu,all}$	<2.4						
$\eta^{e,all}$	< 1.4442 or $1.556 < \eta <2.5$						
# of light leptons	$4e, 0\mu$	$3e, 0\mu$	$1e, 2\mu$	$2e, 2\mu$	$2e, 1\mu$	$0e, 3\mu$	$0e, 4\mu$

This selection is more restraining in the 4ℓ categories, because it is more likely to be able to reconstruct a Z close to the real Z mass, as there are more possible Z bosons to reconstruct.

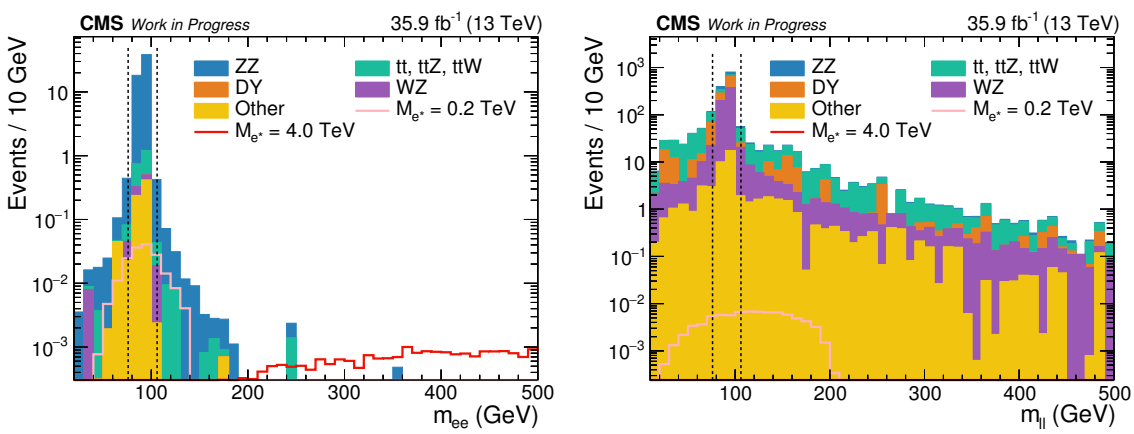

Figure 17: Z cut shown for the 4e (left) and the 1e2μ (right) category. As can be seen, the cut procedure is more restraining in the 4ℓ channel. Filled is the mass of the $\mu^+\mu^-$ (e^+e^-)-pair which is closest to m_Z.

It is possible that a lepton is lost, because it is outside the acceptance of the detector or because the imposed cuts remove it from the selection. For the 4ℓ-categories, this is absorbed by the 3ℓ ones to some extend. Still, this procedure loses some events in signal. How much remains of the signal is the final acceptance times efficiency shown in Fig. 19. As one can see, especially in the very low mass region, the loss in signal is significant, which is mostly due to the cuts on lepton p_T. One should keep in mind, that, as described in the theory section, the decay into same-flavor leptons (compared to opposite-flavor leptons) is twice as likely for both $\mu^*$and $e^*$and in the generated

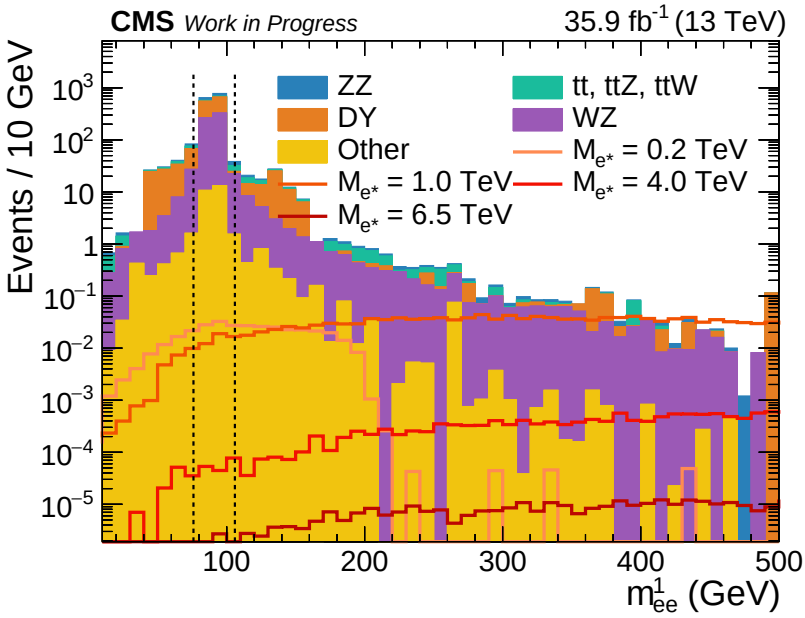

Figure 18: Z cut distribution shown for various signal points. The distribution for signals is more centered around the Z mass for low mass samples.

samples, the decay to τs is included. And as those are not explicitely reconstructed, and decay most likely hadronically (65 % branching ratio), the expected total reconstruction efficiency is around 70-80%. Especially for the e^*search, the addition of the 3ℓ search categories recovers a significant amount. The total efficiency is, for high masses, at 77% for excited muons and around 70% for excited electrons, which is very good considering the fact, that τ-decays are not explicitly analysed.

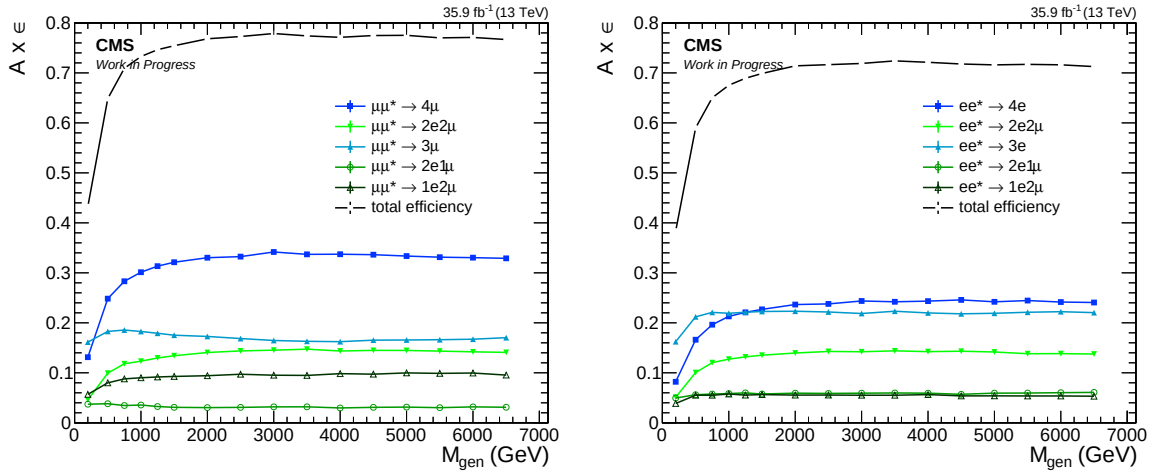

μ* e*

Figure 19: Acceptance times efficiency after all analysis steps for all channels with respect to the number of generated events per sample. Uncertainties are included, but are too small to be seen.

5.4 Invariant mass distribution

As shown in 2.2, the mass of the $\ell^*$is distributed sharply, which makes it interesting to reconstruct, as its shape is significantly different from the expected background. Therefore, the question imposes, what combination of leptons should be reconstructed in order to retain this feature. In case of the 3ℓ categories, the only sensible choice is the reconstruction of the three (light) lepton-invariant mass. For the 4ℓ categories, there is a choice to be made, as we ideally reconstruct a three-body invariant mass (i.o. to get the mass of the ℓ^*), but we have four leptons to combine. Therefore, there are four possible combinations (two, in case of the 2e2µ-channel), and it is not distinguishable, which lepton corresponds to the leptons from the decay. The most interesting reconstruction possibilities are:

- $\mathbf{m}_{min}$: The smallest reconstructable three-lepton invariant mass. The feature of this choice of reconstruction is, that for a signal, the distribution ends at the 'real' mass of the ℓ^*, as it is the heaviest particle in the event.

- $\mathbf{m}_{max}$: For this, the highest possible three-lepton invariant mass is reconstructed. Similar to m_{min}, the final distribution starts at the generated mass of the $\ell^*$and has a long tail to higher masses.

- $\mathbf{m}_{inv}$: A slightly misleading abbreviation, as all of these masses are invariant masses, m_{inv} describes the invariant mass of all (light) leptons in the event. It is not trivial to reconstruct the correct ℓ^* mass from this distribution in the 4ℓ case, as this method significantly widens the whole distribution in both directions.

The effect of the different methods can be seen in Fig. 20. As this is mainly a search for high-mass ℓ^*, m_{max} and m_{inv} are preferable, as the signal-to-background ratio is significantly better at high masses for these two distributions. Additionally, the m_{max}-distribution's tail is mostly in the region where less background is expected, and it is easier to reconstruct the real mass of the ℓ^*, if a signal is found.

5.5 The Control Region

This analysis was designed as a blinded analysis in order to avoid biases towards the signal. Therefore, a control region is defined, in which ideally no signal can influence the selection. This region is used to check for agreement between simulation and data without being influenced by a possible signal. For this, all events, which were vetoed for the signal region by the Z veto, are now instead used for this control region. In all other aspects concerning reconstruction, the selection is the same as it is for the signal region. This choice of control region is not completely void of any signal, as it is possible to reconstruct a $\mathrm{e}^+\mathrm{e}^-$ ($\mu^+\mu^-$) pair within the Z mass window for signal. The likelihood for this is higher for low-mass signals. In any case, the necessary value of Λ (which scales the cross section) in order for the signal to have a significant contribution has been rejected by other analyses by far (e.g. the used signal here has a Λ of 10 TeV,

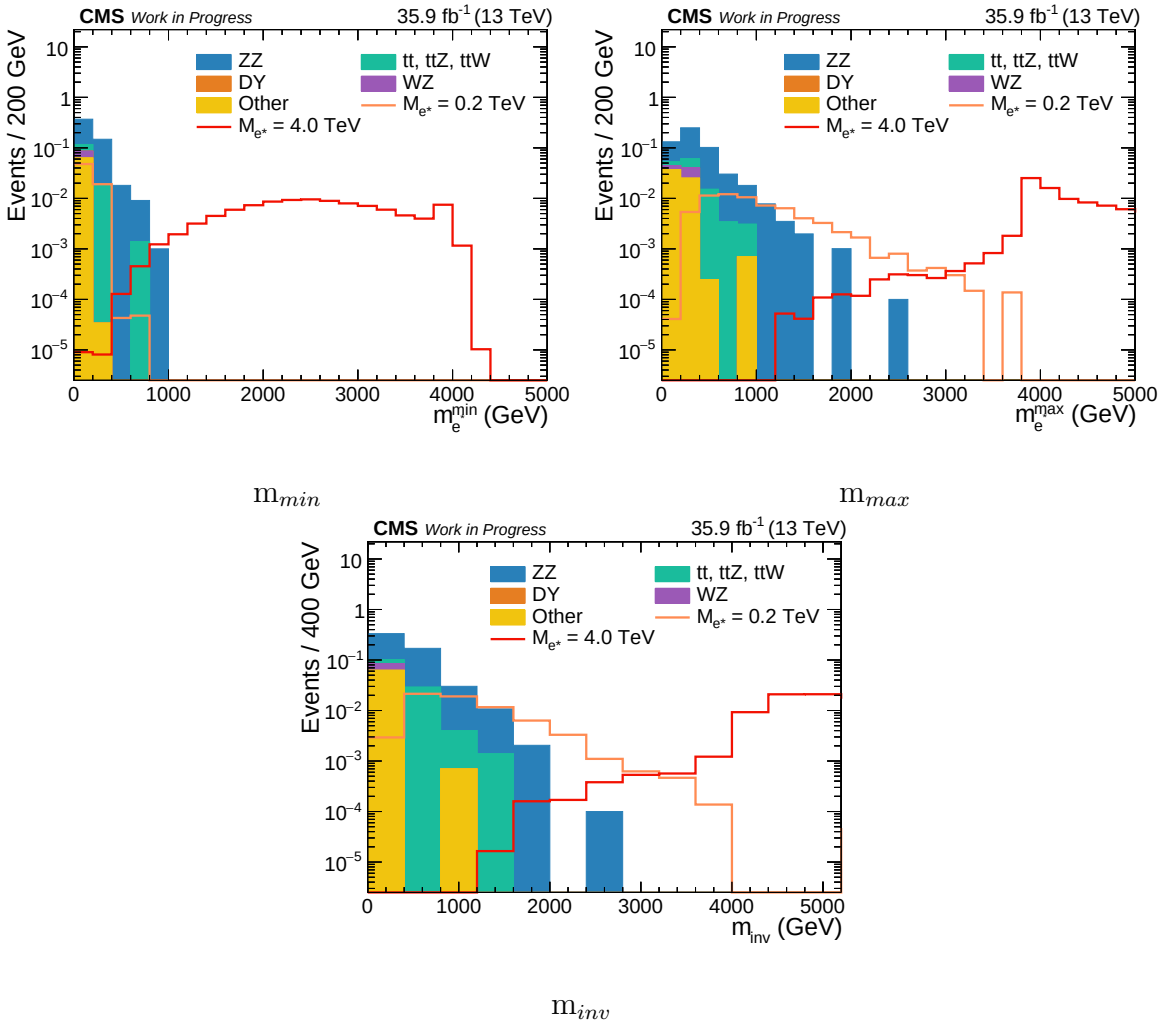

Figure 20: Different possible mass reconstruction methods shown examplarily for the 4e-distribution.

and other searches have exluded a value of Λ of up to 17 (15) TeV for muons (electrons) in the low mass region [16]). Therefore, any possible signal contribution to the control region is negligible. The resulting distributions for this region are shown in Fig. 21 and Fig. 22.

As expected, the background composition differs significantly between the 3ℓ- and the 4ℓ categories, WZ production is dominant for the first one and ZZ for the second one. In the 3ℓ categories, the contribution of Drell-Yan events is influenced by low statistics. As DY-events only enter the selection in case a jet is identified as a lepton, there is not sufficient Monte Carlo statistics over the whole distribution for this background. This can be seen in the corresponding ratio plots, which partly have large statistical error band even in regions with supposedly many events. Still, overall the measured data agrees within the uncertainties with the prediction from SM Monte Carlo simulation.

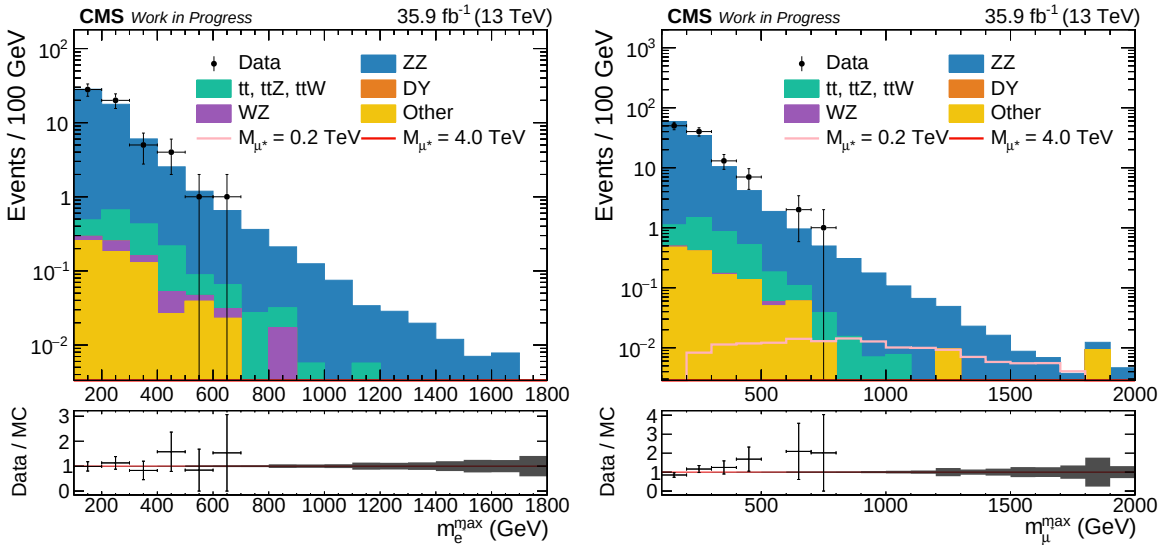

4e 4μ

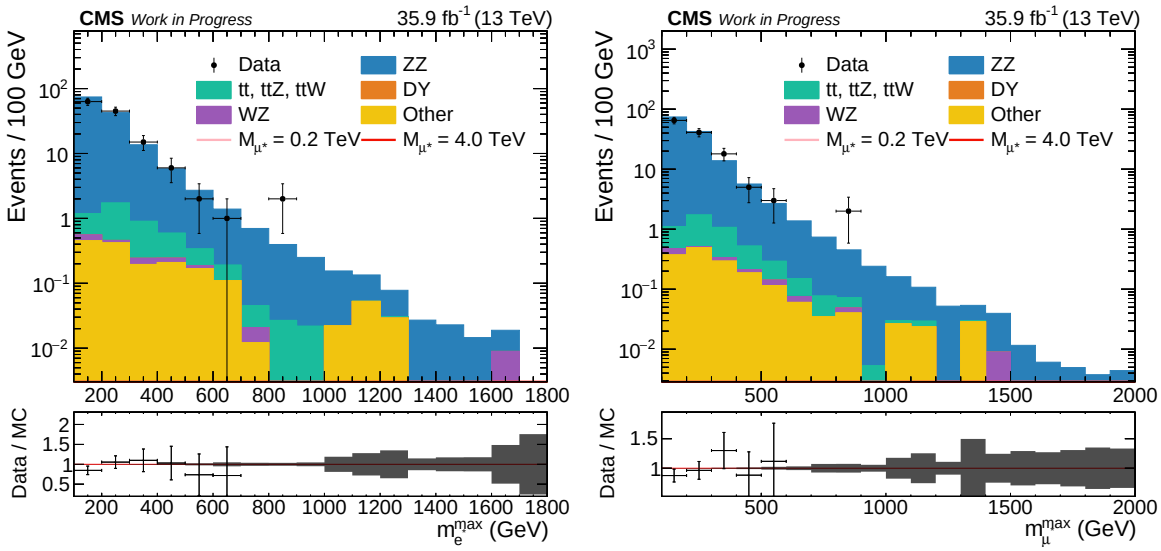

2e2μ,e^* 2e2μ,μ^*

Figure 21: Control region distributions of the 4ℓ categories, where the object selection is as described, but uses an inverse Z veto: there has to be at least one $\ell^+\ell^-$ pair in the Z mass window.

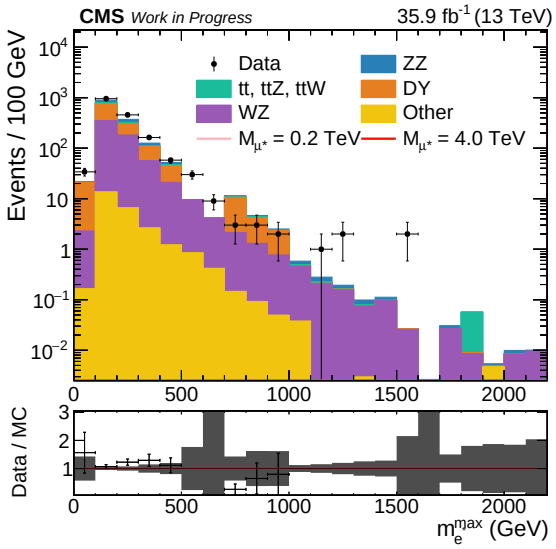

3e

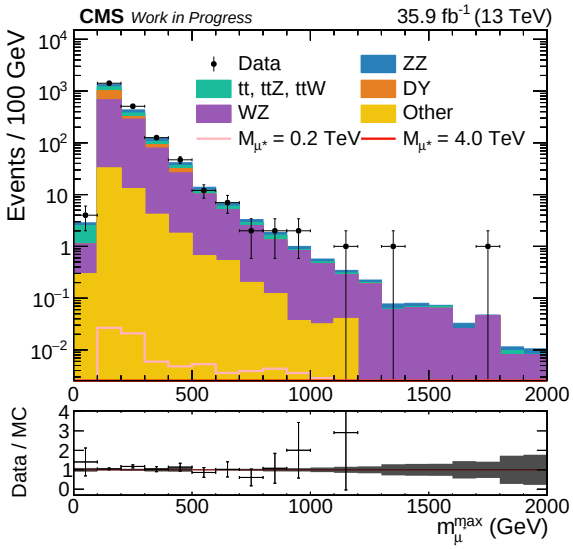

3μ

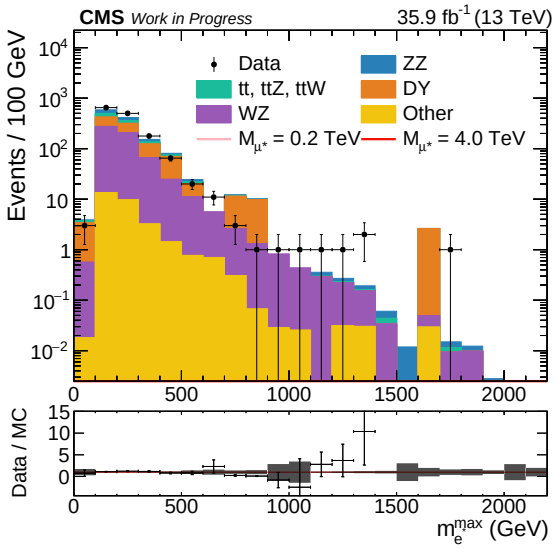

1e2μ

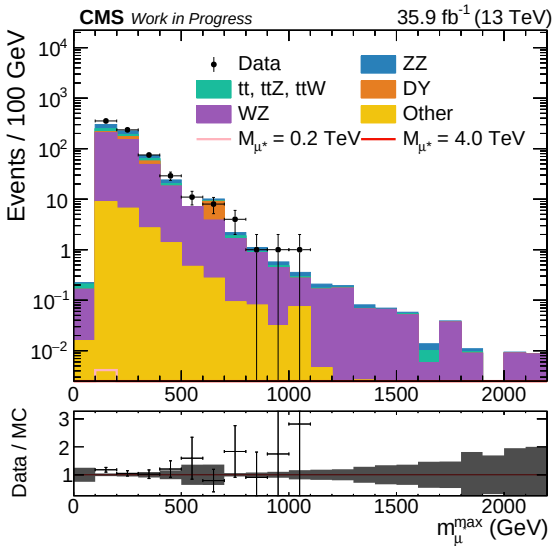

2e1μ

Figure 22: Control region distributions for the 3ℓ categories, with same restrictions as for the 4ℓ one.

5.6 Background Prediction Corrections

Due to various effects some corrections have to be applied to the background prediction by simulation. They are applied to the weight of an event (as denoted as α in seciton 4.1.1). These are most notably the pileup reweighting and the introduction of scale factors to correct for differences in reconstruction efficiencies between data and simulation. These corrections are explained in this chapter.

5.6.1 Pileup Reweighting

The occurence of several interactions during a single bunch crossing at the CMS detector is called pileup. There are two types of pileup, namely the 'in-time' pileup and the 'out-of-time' pileup [28]. While the former describes other interactions, which take place at the same time as the event one is interested in, the latter comes from an earlier event, whose data are still processed in detector parts with a response time larger than the bunch crossing time (25ns). Both contribute to the overall pileup, which is simulated by Monte Carlo, but may still be slightly different than data (e.g. pileup in data may change in time). In data, pileup is estimated from the measured luminosity in each bunch crossing times an average total inelastic cross section (minimum bias cross section).

This effect can be corrected for, using a method called 'pileup reweighting'. For this, a simulated event is weighted with a factor describing the discrepancy between data and simulation. A systematic uncertainty is included for this correction and explained in section 5.7.

5.6.2 Scale Factors

The reconstruction efficiency of particles differs slightly between data and simulation. This misbehaviour is measured and corrected by using event-by-event scale factors. These scale factors are calculated per particle comparing the efficiency in data and simulation. This is done by the corresponding CMS subgroups (Muon POG [45] for muons, EGamma POG [46] for electrons/photons). For muons, a scale is applied due to identification efficiency and isolation efficiency differences. For electrons, it is due to track reconstruction and ID efficiency. To show the size of the applied correction, the scale factors in dependency of η and $\mathrm{p_T}$ for electron identification are given in Fig. 23. In this figure, it can be seen, that especially for very low $\mathrm{p_T}$-electrons, there is a significant difference in reconstruction efficiency. Also, the gaps in electron reconstruction in $1.4442 < |\eta_e| < 1.556$, which are cut out in this analysis, are clearly visible. For all well-covered regions and electrons with sufficient $\mathrm{p_T}$, the order of the applied correction is around 1%. This is similar for other scale factors of electrons as well as those for muons.

Uncertainties on this procedure are explained in the next section.

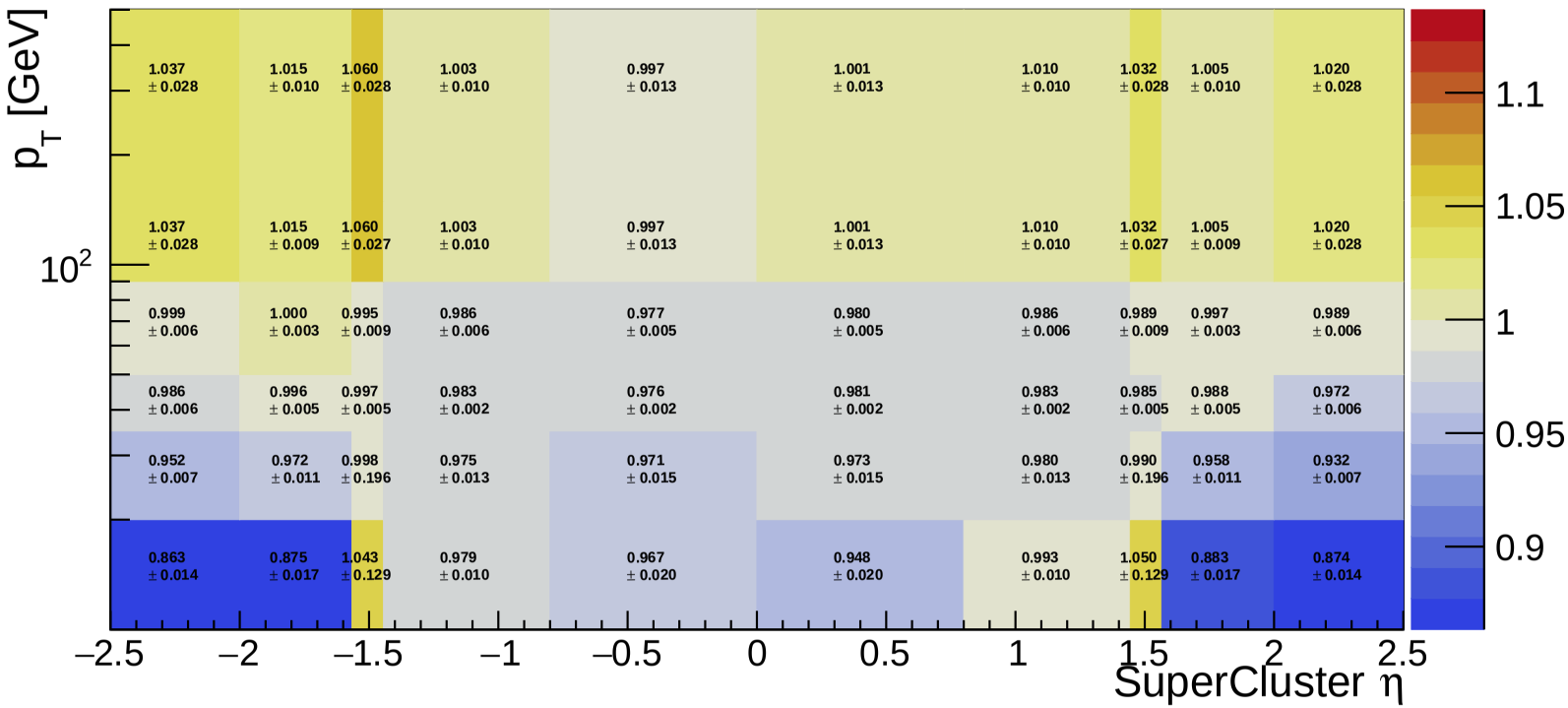

Figure 23: Scale factors for the electron identification efficiency, depending on η and p_T. The correction is in the order of 1% per electron.

5.7 Systematic Uncertainties

In this chapter, systematic uncertainties and the sources they arise from will be discussed. An overview on the different systematics and their relative size is given in Fig. 24, 25. These distributions are calculated on signal samples, as statistical uncertainties are significantly smaller. In the figures, the statistical error of the background prediction is included in order to show the relative size of systematic and statistical error. For the total systematic uncertainty, the different types are added quadratically. The included systematic uncertanties are:

- For each particle, there are systematic uncertainties on their respective resolution and energy scale based on recommendations from [47, 48]. In order to address those, for each event the corresponding quantity is shifted within one standard deviation and the final distributions are recalculated. By comparison with the original final distribution an estimate of the error can be evaluated. For electron resolution, the error is found to be negligible.

- A similar procedure is used to evaluate the systematic uncertainty arising from the pileup-reweighting method (as explained in 5.6.1). For this, the minimum bias cross section of the pileup prediction is shifted, and the final distribution is recalculated. This method is recommended by the Lumi Physics Objects Group of CMS [49]

- In order to account for uncertainties on the applied scale factors (as explained in 5.6.2), an uncertainty of 1.5% per muon and 2% per electron is assumed on the final distribution, as recommended by [45, 46].

- A systematic uncertainty on the luminosity of 2.5%, as measured in [28], is included.

- As protons are composite objects, consisting of valence quarks, sea quarks and gluons, each 'parton' carries a part of the momentum of the proton. The exact momentum of the partons is unknown, but it can be described by the 'parton distribution functions', which are statistical distributions of the partons momenta, which were measured by previous experiments [50] and are extrapolated [51] towards the LHC energy range. For all background samples, a systematic uncertainty arising from the parton distribution functions is included. These PDF uncertainties are calculated using event-dependent weights as recommended in the PDF4LHC prescription [52] using NNPDF3.0 cross section calculations. This uncertainty increases for higher energies, as the description of PDFs becomes less accurate. For the signal, this method is altered, as this includes both a shift from acceptance as well as from normalisation. The latter is in prinicple just an uncertainty on the cross section of the theory and is therefore neglected. Therefore, for signal, only the PDF uncertainty from acceptance is calculated and used. As the accpetance is quite high, this error is very small (roughly 0.1% and smaller).

It can be seen, that the muon scale uncertainty increases with higher masses, which is due to the fact, that the tracks of high-energy muons become more and more straight, making correct scale estimation more difficult.

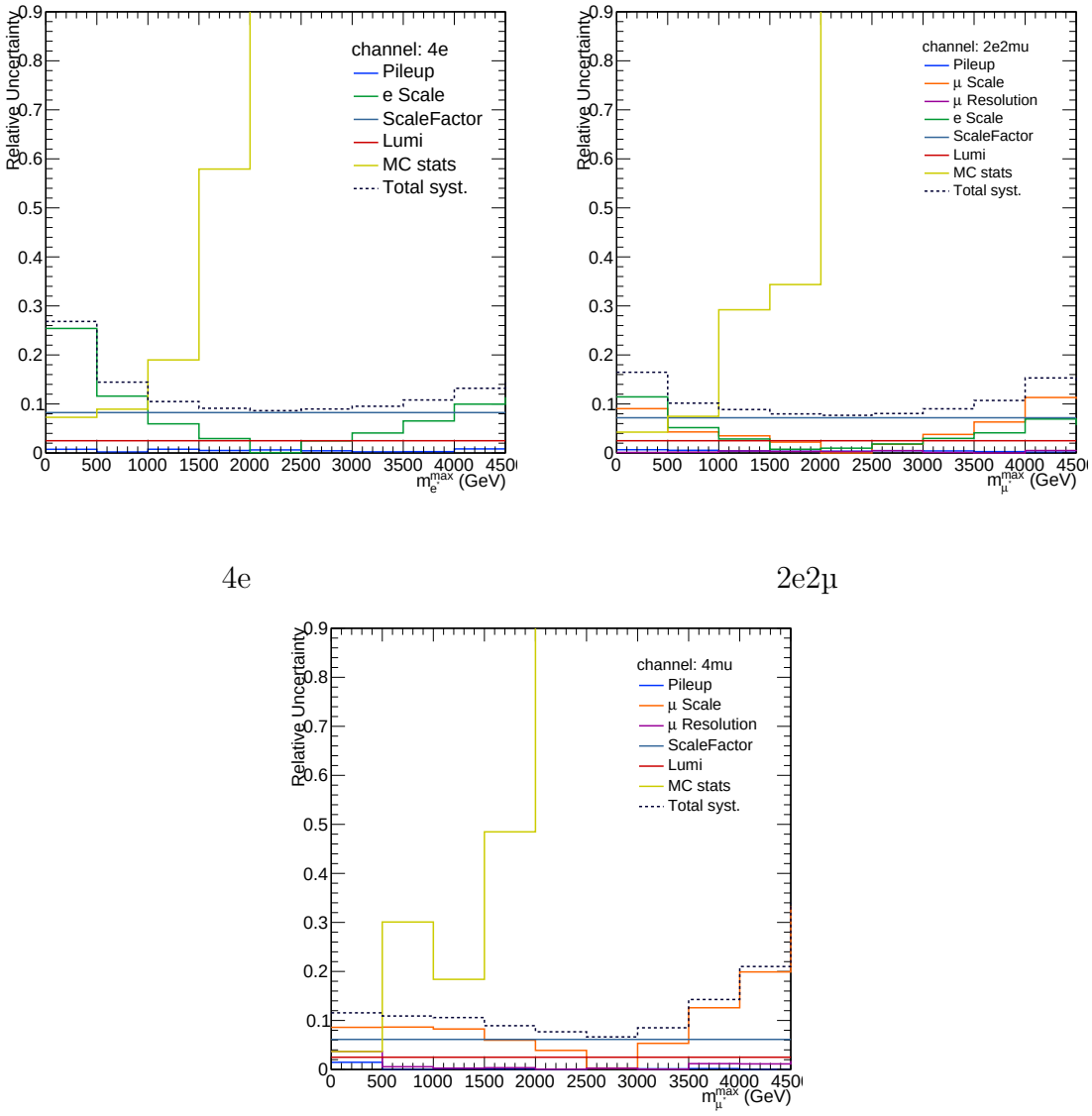

4e 2e2μ

4μ

Figure 24: Overview of systematic uncertainties for 4ℓ channels. As a comparision, the statistical error of the prediction from SM simulation is included. The relative error is quite significant, as the expected background is very low.

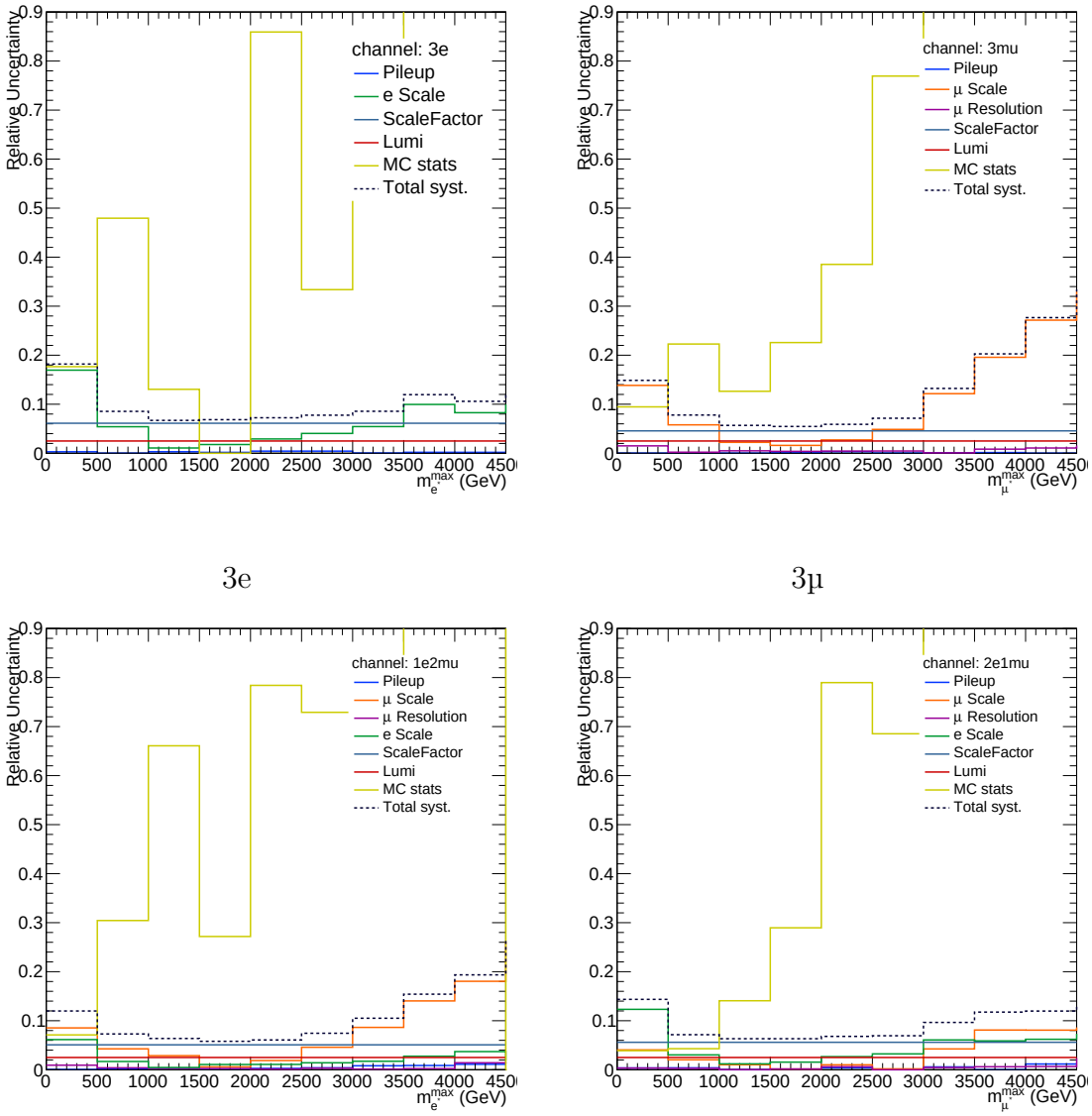

3e 3μ

1e2μ 2e1μ

Figure 25: Overview of systematic uncertainties for 3ℓ channels. As a comparision, the statistical error of the prediction from SM simulation is included.

6 Results

6.1 The Signal Region

As the control region shows sufficient agreement, the thesis was unblinded and the results are analyzed on their statistical behaviour. The background composition, integrated over the whole spectrum, for all channels is given in Tab. 6 together with the total number of data events with its statistical uncertainty per channel. The corresponding distributions are shown if Fig. 26 and 27. As can be seen, in some channels for some backgrounds (especially Drell-Yan), there are large statistical uncertainties on the background prediction by simulation. This effect is more significant for the 3ℓ-categories than for the 4ℓ ones. Taking the statistical uncertainties into account, most search regions show agreement between data and simulation.

More interesting is the 2e2µ region, as there is an apparent discrepancy between data and simulation without apparent statistical problems in the background prediction. The significance of this excess was calculated to 2.7σ, using the 'higgsCombine'-Tool of the CMSSW software [53]. Although there is a discrepancy between data and simulation, it is rather unlikely, that this is in fact a hint towards the existence of an excited lepton. As shown, a signal would have a large contribution at higher masses using this reconstruction method. Nevertheless, this might be hint towards new physics, which can be tested more thoroughly with more data, to see, if this is just a statistical effect, or something really interesting.

Another intersting data point is found in the 3e-category at a mass of almost 3 TeV. Although not too signficant, this might be a hint towards the existence of an excited lepton. It would be interesting to see whether this is an effect of statistics or if there might be something. For this, more data will be needed to test this region more thoroughly.

Table 6: Overview of the total number of events per channel integrated over the whole distribution for both background and data. As can be seen, there are significantly more events in the 3ℓ categories compared to the 4ℓ categories.

Background	4e	4μ	$2e2\mu$
ZZ	0.41 ± 0.01	0.58 ± 0.02	1.52 ± 0.03
$t\bar{t}$, $t\bar{t}Z$, $t\bar{t}W$	0.05 ± 0.01	0.21 ± 0.06	0.54 ± 0.07
DY	< 0.01	< 0.01	< 0.01
WZ	0.02 ± 0.01	0.11 ± 0.01	0.09 ± 0.03
Other	0.06 ± 0.01	0.10 ± 0.01	0.07 ± 0.03
N_{exp}^{evt}	0.55 ± 0.03	0.91 ± 0.06	2.29 ± 0.08
N_{data}	1	0	7

Background	3e	$2e1\mu$	$1e2\mu$	3μ
ZZ	16.9 ± 0.1	13.9 ± 0.1	19.1 ± 0.1	20.4 ± 0.1
$t\bar{t}$, $t\bar{t}Z$, $t\bar{t}W$	27.8 ± 0.9	126.5 ± 2.1	266.6 ± 3.2	142.5 ± 2.3
DY	171.2 ± 47.1	11.7 ± 7.6	80.4 ± 31.2	$47,4 \pm 26.4$
WZ	53.3 ± 0.6	57.3 ± 0.7	66.5 ± 0.7	70.8 ± 7.6
Other	5.5 ± 0.6	15.4 ± 1.1	23.1 ± 1.2	11.5 ± 2.6
N_{exp}^{evt}	274.6 ± 47.1	224.8 ± 8.1	455.8 ± 31.4	292.7 ± 26.5
N_{data}	231	246	469	270

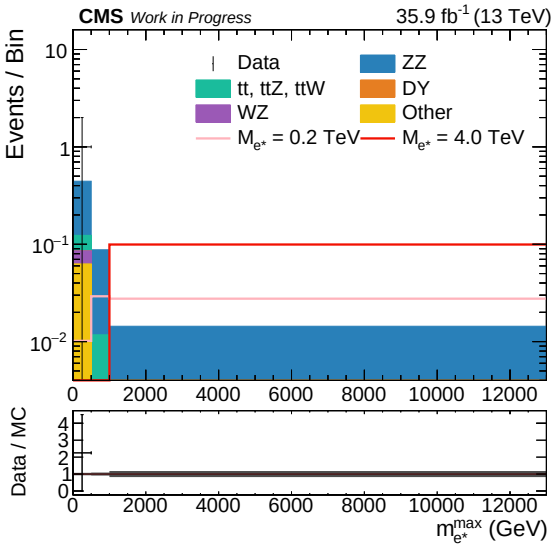

4e

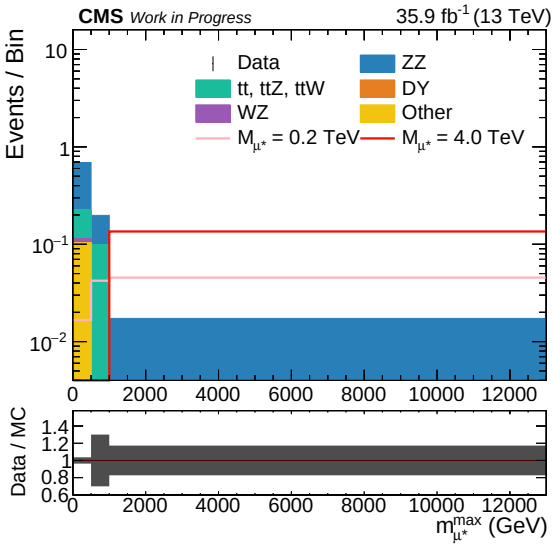

4μ

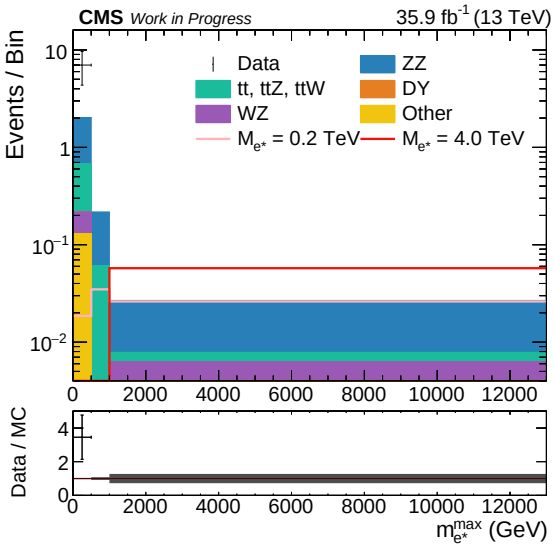

2e2μ,e^*

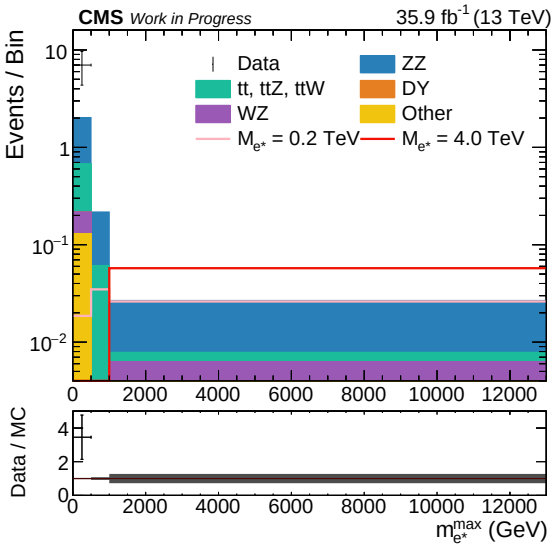

2e2μ,μ^*

Figure 26: Signal region distributions for the 4ℓ categories. Note, that in the 4μ-channel, there is no data entry as no event was found in data, not because it was missed to be plotted.

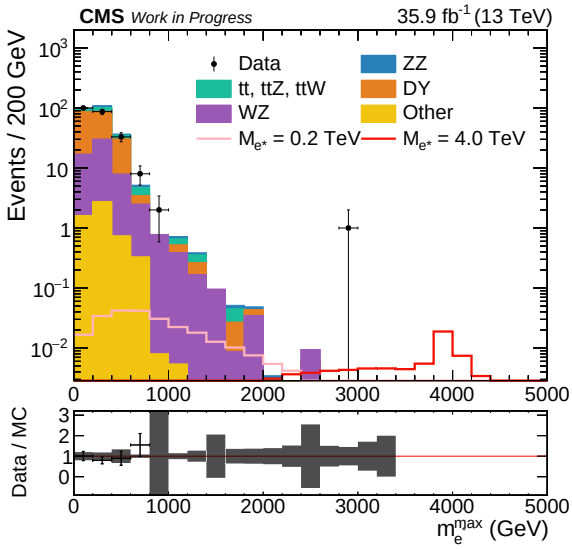

3e

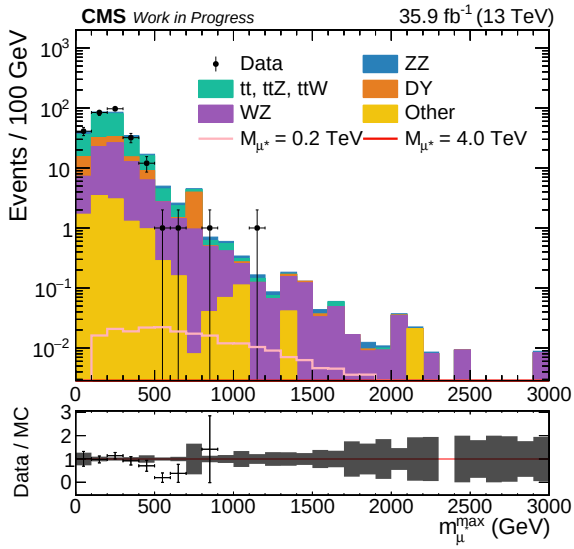

3μ

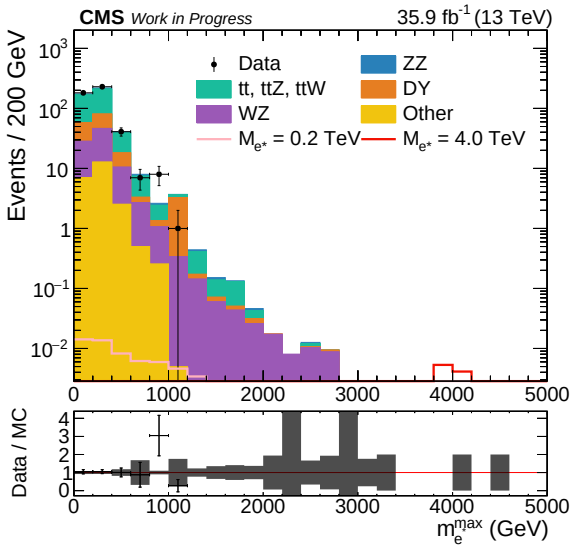

1e2μ

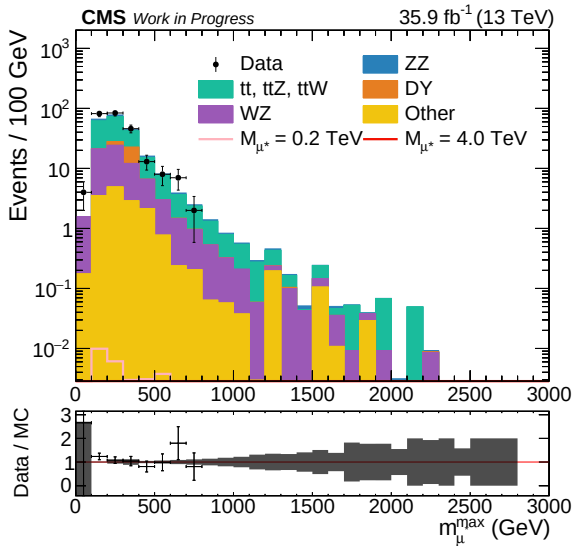

2e1μ

Figure 27: Signal region distributions for the 3ℓ categories, with same restrictions as for the 4ℓ one.

6.2 Statistical Interpretation

As no significant signal contribution was found in the final distributions, exclusion limits for the theory are set. A Markov-Chain MC based Bayesian [54] limits setting approach is used in order to determine limits on the cross section, the mass of a ℓ^* and the scale Λ. The limit setting is performed on the m_{max}-distribution (as explained in 5.4) using the 'higgsCombine'-Tool from the CMSSW software [53]. As mentioned earlier, an issue of this analysis is the lack of statistics in the background estimation. In order to address this problem, different approaches were used for the 4ℓ and 3ℓ categories. For the 3ℓ categories, a background fit is performed for each search channel. For the 4ℓ categories, this is not feasible, as statistics are too low for this approach in these channels. Instead, large bins are used to set the limit in order to increase the MC statistics per bin.

6.2.1 Background Fitting Method

In this section, the backround fit performed on the 3ℓ-categories to cope with lacking statistics from the simulated background is explained. A function of the form

$$f(x) = \frac{\alpha}{(x^3 + \beta x + \gamma)^\delta}$$

is fitted on each of the final distributions (with x = m_{max}, and f(x) being the cross section) in a range from 300 to 1500 GeV. This is an empirically tested function, which has shown to simulate missing statistics quite well. The binning of the distributions is 200 GeV binning in order to ensure decent statistics in the background prediction per bin. The results of this fit are shown in Fig. 28.

In the shown distributions, the grey error bands are fit-only errors and do not include errors from a possible bias due to the choice of function as well as the error induced to choice of the fit range. The latter one was varied and the errors were found to be of the same size as the errors from the fit itself. In order to include this uncertainty, a total uncertainty of 100% is assumed for the whole fit range. The final distributions with all errors included (the same way as they enter the limit setting) are shown in Fig. 29

For the 4ℓ categories, this method is not feasible, as the statistics of the background estimation are too low to perform a reasonable fit. Instead a broad-binning approach with a binning with bin-edges of [0,500,1000,13000] GeV is used.

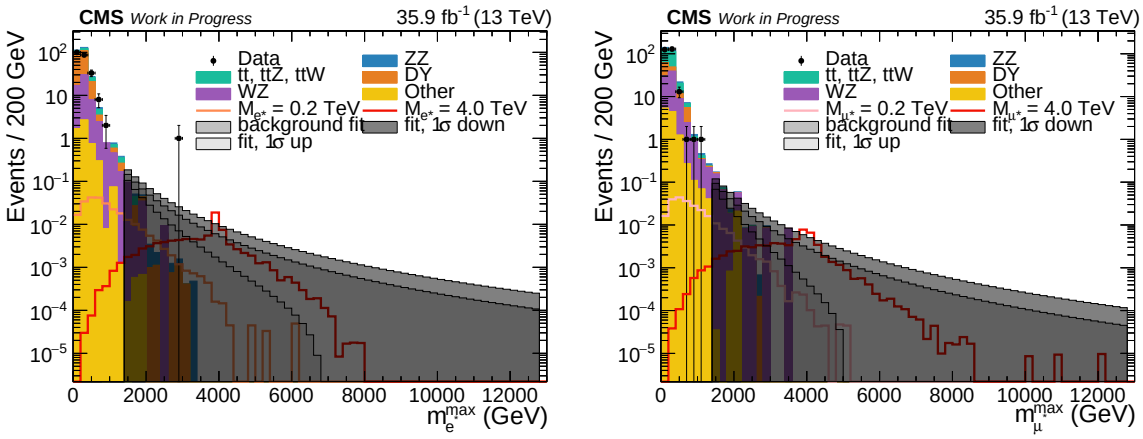

3e

3μ

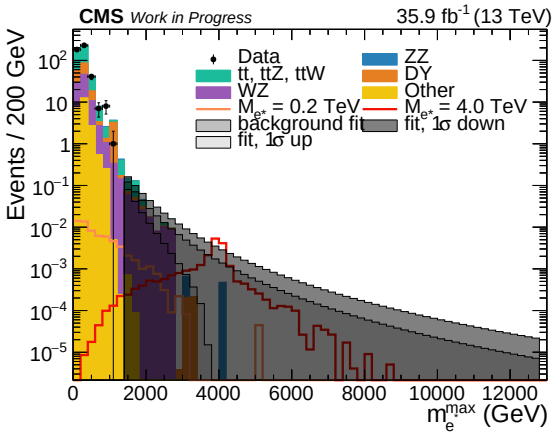

1e2μ

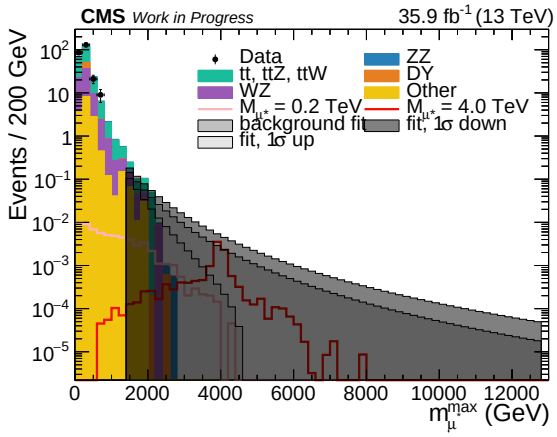

2e1μ

Figure 28: Background fit performed on each final distributions from the 3ℓ category. Grey bands shown the best fit, as well as the corresponding error bands for one σ of deviation up and down coming from the fitting error.

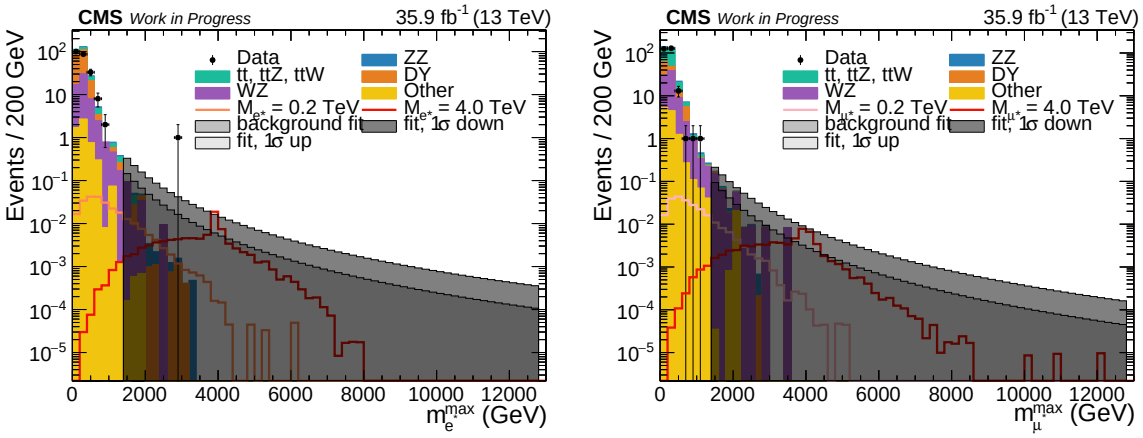

3e 3μ

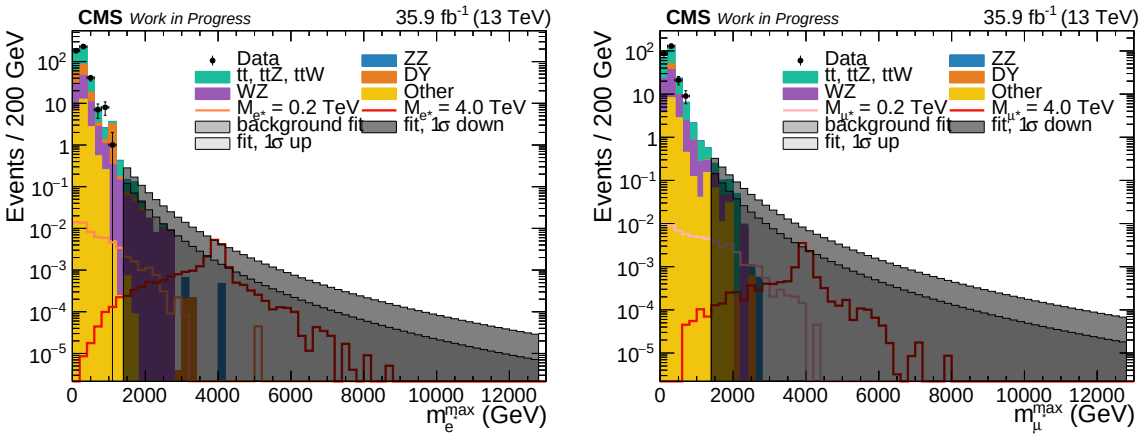

1e2μ 2e1μ

Figure 29: Background fit performed on each final distributions from the 3ℓ category. Grey bands shown the best fit, as well as the corresponding error bands for one σ of deviation up and down. In addition to the fit error, an uncertainty of 100% is assumed to include bias from the choice of function as well as uncertainties coming from the choice of the fit range. As the total error is around 100%, the result of the down shifted fit is not visible.

6.2.2 Limit setting

For limit setting, a Bayesian approach is used. In case of a counting experiment (which is principally true for high masses of the ℓ^*-signal) with no background and an exact knowledge of the efficiency ϵ, the measured number of events is Poisson-distributed with mean $s\epsilon$. Bayes' Theorem then imposes

$$p(s|n) = \frac{P(n|s)\pi(s)}{\int P(n|s)\pi(s)\,\mathrm{d}s}$$

where $P(n|s)$ is the probability of measuring n, given s; $\pi(s)$ is the prior probability density function and $p(s|n)$ is the posterior probability density function for s, given an observed n. Assuming a constant function for $\pi(s)$ and a Poisson distribution for $P(n|s)$

$$P(n|s) = \frac{e^{-s\epsilon}(s\epsilon)^n}{n!}$$

one ends up at

$$p(s|n) = \frac{\epsilon e^{-s\epsilon}(s\epsilon)^n}{n!}$$

The limit is obtained by integrating this function for s until the required fraction β of the total integral from 0 to infinity is reached. β is often called the 'Bayesian confidence level' or credibility of the test. For a chosen β of 95%, the upper limit $\mathrm{s_u}$ is given by

$$\int_0^{s_u} p(s|n)\,\mathrm{d}s = 0.95$$

Similar but more complex methods are used in case of an assumed background and with the inclusion of uncertainties. More information on these methods can be found in [12, 54].

Limits were set on the cross section for both e^* and μ^*. For both signal types, all relevant channels were combined (e^*: 4e, 3e, 2e2µ, 1e2µ; μ^*: 4µ, 3µ, 2e2µ, 2e1µ) and the resulting limit was calculated for each mass point. For the 4ℓ categories, the broad binning approach is used, while for the 3ℓ classes, the background fit as described in 6.2.1, is used. The result is shown in Fig. 30.

As mentioned in the theory section, the cross section highly depends on the compositness scale Λ. Therefore, these cross section limits can be reevaluated into Λ-limits by inversing the formular. The result of this calculationg for both types of signals is shown in Fig. 31.

In order to cross check the limit setting procedure, it was redone using a broad-binning approach for the 3ℓ categories. The results of all single-channel limits can be found in the appendix 8.4. Both methods lead to very similar results. An overview of all limits is given in Tab. 7. The final 95% confidence level exclusion limit on the mass of an excited electron (muon) is 4.5 (4.6) TeV.

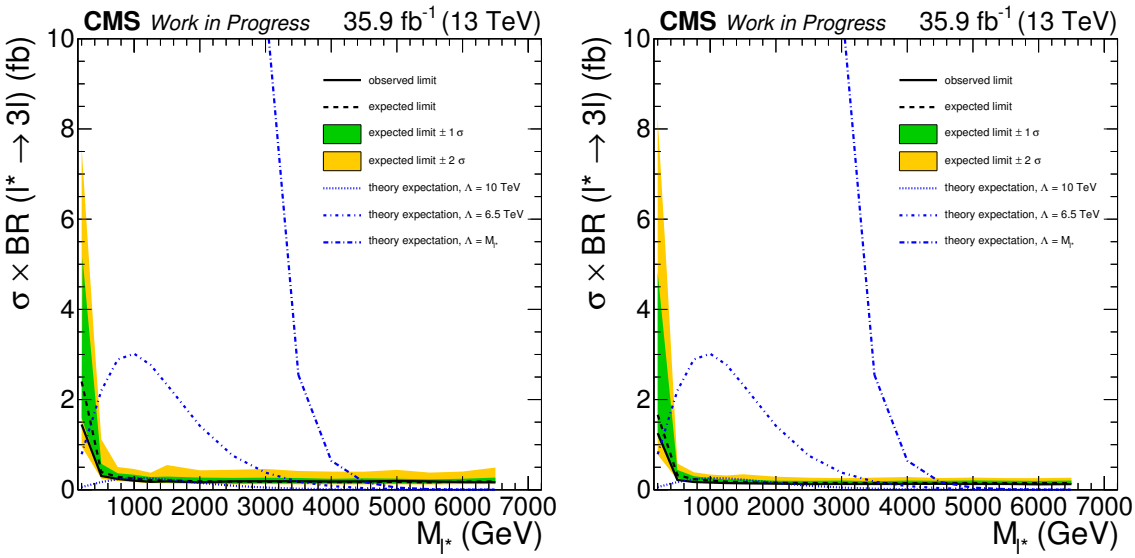

Figure 30: Combined limits for both e^* (left) and μ^*. Limits are calculated using the Bayesian approach and all relevant channels are combined for each signal type.

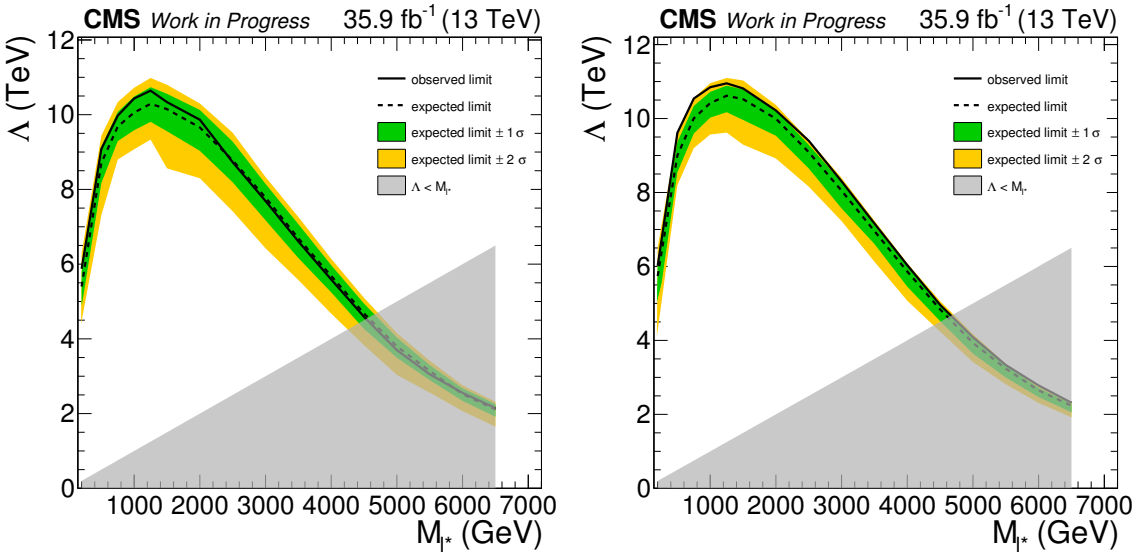

Figure 31: Cross section limits reevaluated into limits on the compositness scale Λ for both $e^*$and μ^*.

Table 7: Overview of all limits calculated with broad binning for the 4ℓ categories and background fit for the 3ℓ categories.

Channel	Cross section / fb^{-1}	Mass limit / TeV
4e	0.4	4.3
2e2μ	0.6	4.0
3e	0.5	4.1
1e2μ	1.0	3.7
e^*combined	0.2	4.5
4μ	0.3	4.4
2e2μ	0.6	4.0
3μ	0.8	4.0
2e1μ	3.0	3.4
μ^*combined	0.14	4.6

6.2.3 Comparison to other analyses

As this is the first analysis in this search channel, one can only compare the results to searches in different channels. The most restraining results in the $\ell\ell\gamma$ channel from CMS provide limits of 3.0 / 2.8 TeV on mass for the muon / electron case [16]. ATLAS published results for excited lepton analyses for $\sqrt{s} = 7$ and $\sqrt{s} = 8$ TeV so far, which are less restraining [17, 55]. So, this analysis does provide the best exclusion limits on the mass of an excited lepton in the contact interaction scenario to date, while it is not as restraining for limits on the compositeness scale Λ (where the $\ell\ell\gamma$-analysis excludes values of up to 17 TeV in Λ for low masses). This is mainly due to the branching fraction of the theory, which is significantly higher for the other search channels in the low-mass region, where the production cross section is still quite high.

7 Conclusion and Outlook

This thesis presents a complete search for excited leptons in the leptonic contact-interaction decay channel. In this previously untouched search channel, seven leptonic final states were analysed (4e, 3e, 2e1µ, 2e2µ, 1e2µ, 3µ, 4µ). The whole 2016 data set (center-of-mass energy $\sqrt{s} = 13$ TeV) recorded with CMS, corresponding to an integrated luminosity of 35.9fb^{-1} was used. Muons are selected using a dedicated set of identification criteria suited for high-p_T muon, while electrons are reconstructed using a cut-based loose ID. After objects are reconstructed, a Z boson cut is implied to further reduce the expected background of the Standard Model. The resulting final distributions based on m_max are analysed with respect to the agreement between data and prediction from simulation. For the 3ℓ search categories, a background fit is performed in order to reduce the analysis' dependency on statistical fluctuations coming from simulation. In the 4ℓ-categories, this is handled by using a large-binning-approach.

The final distributions for both e^* and μ^* were combined with respect to their corresponding channels for limit setting. Exclusion limits with 95% confidence level were set on the mass of an excited electron to 4.5 TeV (10.5 TeV in Λ) and 4.6 TeV (11 TeV in Λ) for excited muons for the case of $M_{\ell*} = \Lambda$. This is a vast improvement in terms of a mass limit compared to earlier analyses with exclusions of up to 3 TeV [16].

In order to increase the sensitivity for this theory, it could be of use to analyse the $2\ell 2q$-channel, as it has a significantly higher branching ratio, as shown in 2.2. This search channel has a significantly higher background expectation, but, if this can be coped with, it can provide better mass limits. Also, it is of high interest to take more data in order to determine, whether the seen deviations from the Standard Model expectation hint towards new physics or are just statistical effects.

8 Appendix

8.1 Channel dependent cuts

In this part, the effect of the different channel-dependent cuts on the transverse momentum of the (sub-)leading electron / muon is shown for different signal samples, the results are shown in Fig. 32. As expected, the imposed p_T cuts have a larger impact on low-mass signals, as the p_T of the generated particles (electron, muon) are typically smaller. For high-mass samples, the cut barely affects the reconstuction efficiency at all.

8.2 The Z cut

After object selection (the reconstruction of light leptons, in this case), all possible Z boson candidates are computed by evaluating the invariant mass $m_{\ell\ell}$ of all possible same-flavor, opposing-charge sign leptons. If this mass is within the mass window of 15 GeV around the Z bosons mass ($\approx$ 91 GeV), the event is vetoed. The cut is shown in Fig. 33 for all channels (only the mass, which is closest to m_Z is filled per event).

8.3 Event Displays

In this short chapter, event displays of the seven 2e2µ-events are shown. They are created using the cmsShow-routine of the CMSSW software on the picked events of the 2e2µ search category. Note, that in these event views, there might be additional muon / electron candidates, but only two of each have passed all selection criteria. Muons are indicated with red lines, electrons are indicated with light blue lines.

8.4 Limits

In this part of the appendix, other limit plots are shown, including single-channel limits (those, which are calculated on a single final distribution), as well as the limit plots made with broad binning for all search categories (combined for e^*,μ^*).

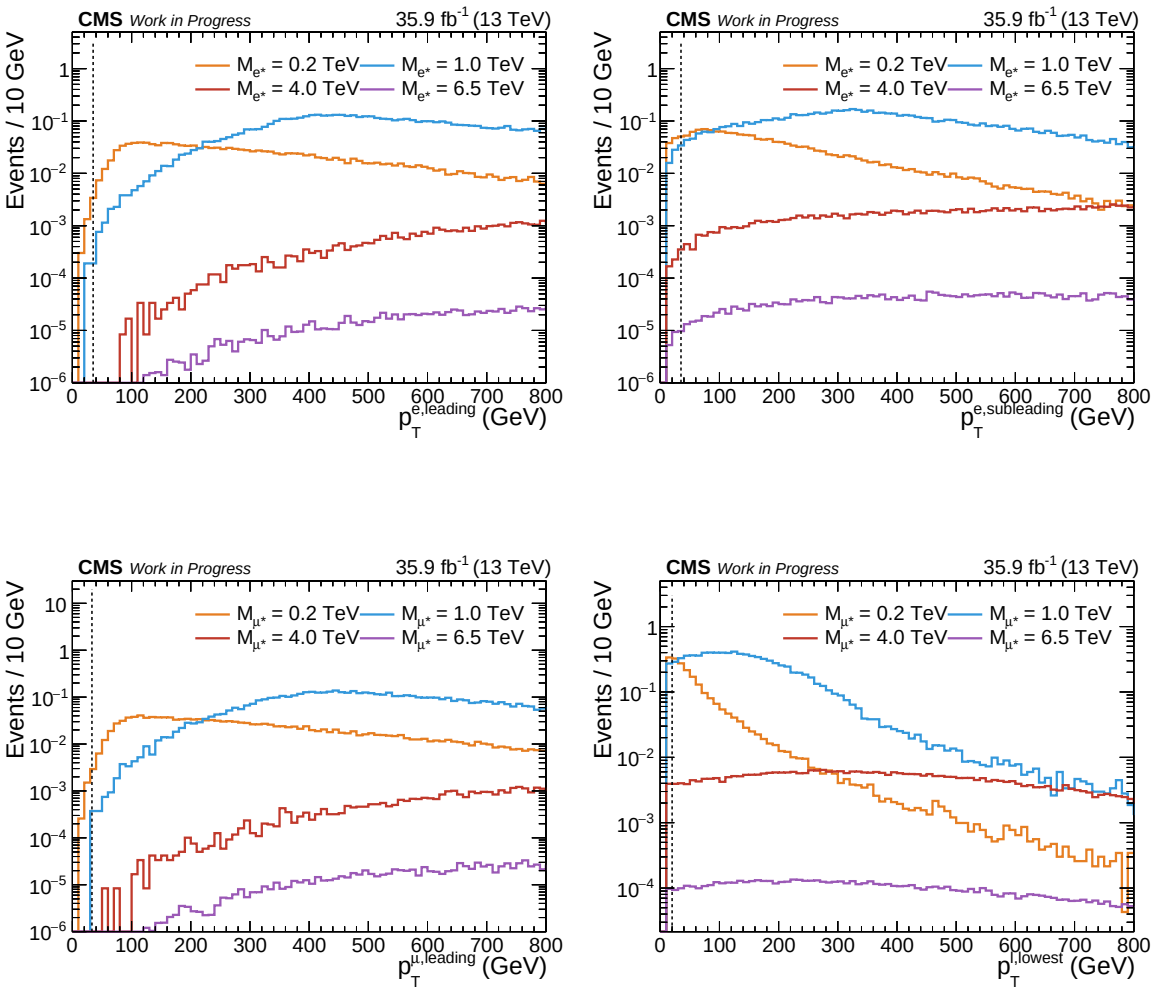

Figure 32: Effect of channel-dependent cuts on signal for different generated signal masses. On the left the distribution where the p_T of the leading electron per event is filled, in the middle it is shown for the subleading electron, and on the right the p_T of the leading muon is shown. The corresponding cut is indicated with the black dotted line. Events, where the (sub-)leading electron / leading muon has $p_T < 35$ GeV, are cut out. Also, all events with a lepton with less than 20 GeV transverse momentum are cut.

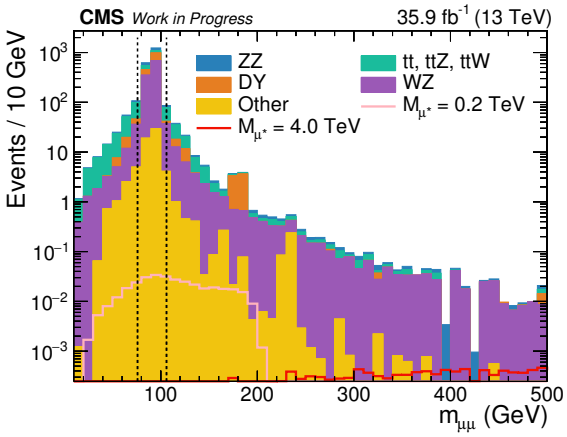

3μ

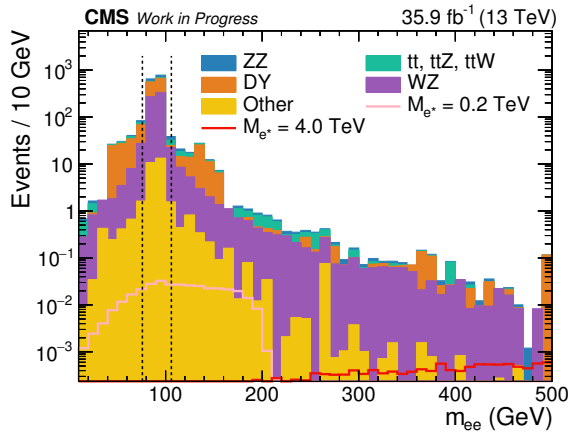

3e

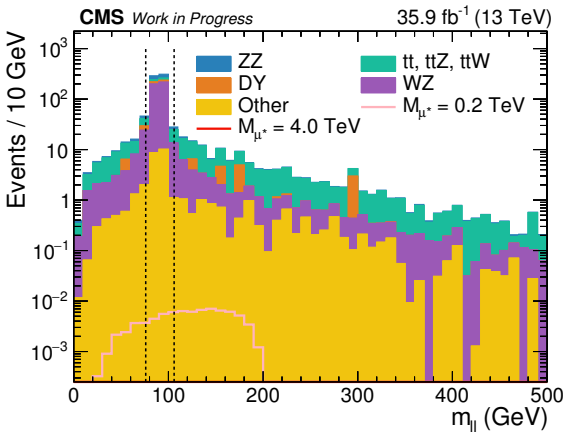

2e1μ

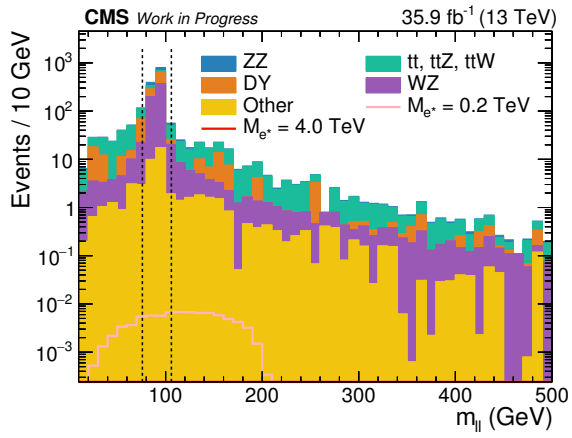

1e2μ

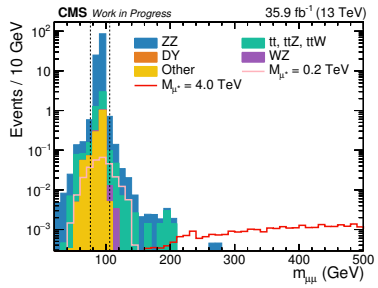

4μ

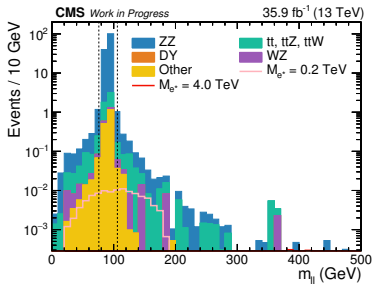

2e2μ

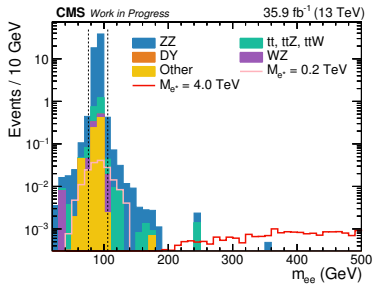

4e

Figure 33: Z cut shown for all channels. The cut's impact is more significant on the 4ℓ categories than on the 3ℓ ones as there are two possible Z bosons to be reconstructed (in ZZ background) and there are more $\ell^+\ell^-$-combinations.

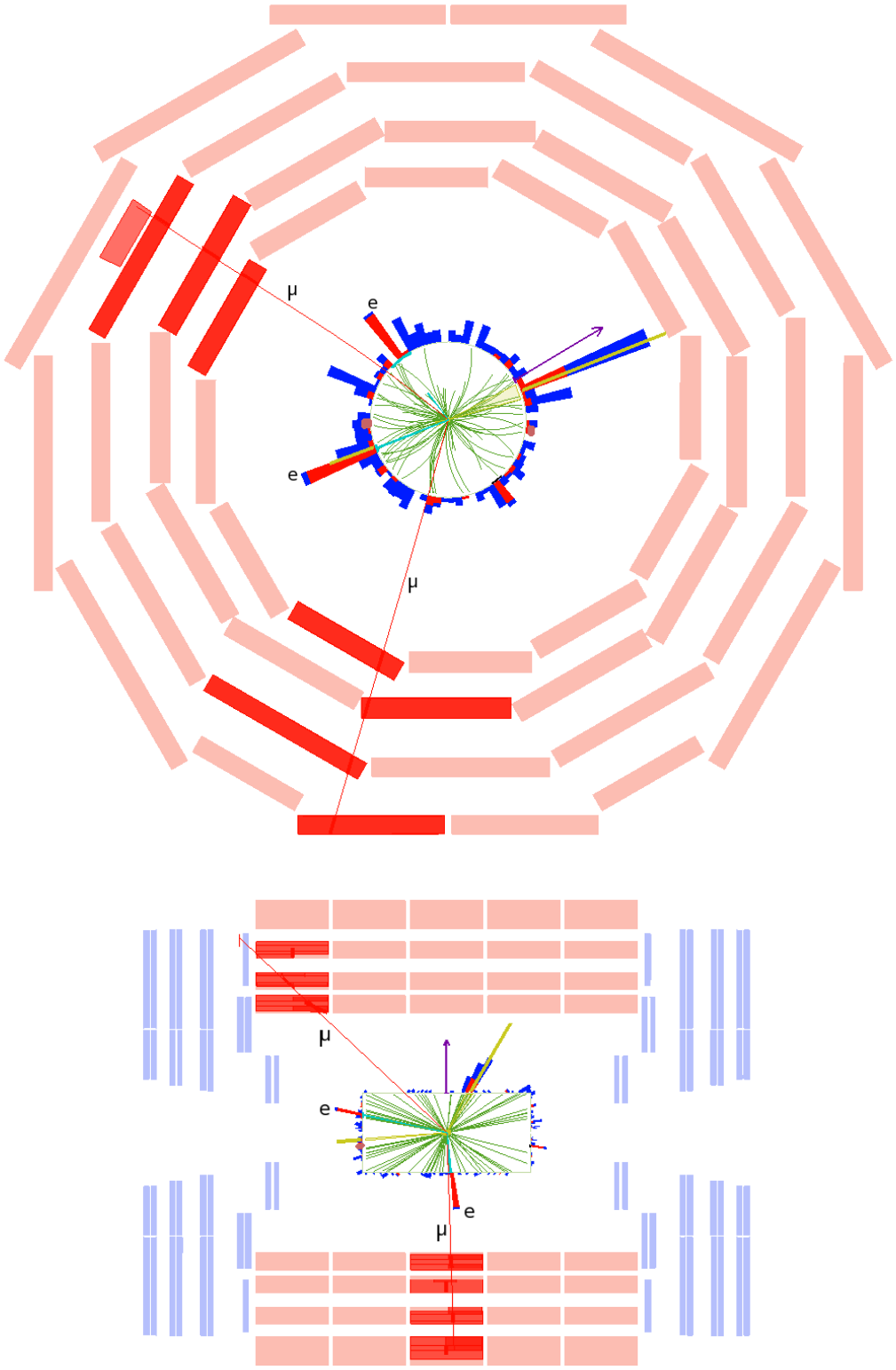

Figure 34: Event view of a 2e2μ event. Left side shows $\rho - \phi$ view, right side the ρ−z view.

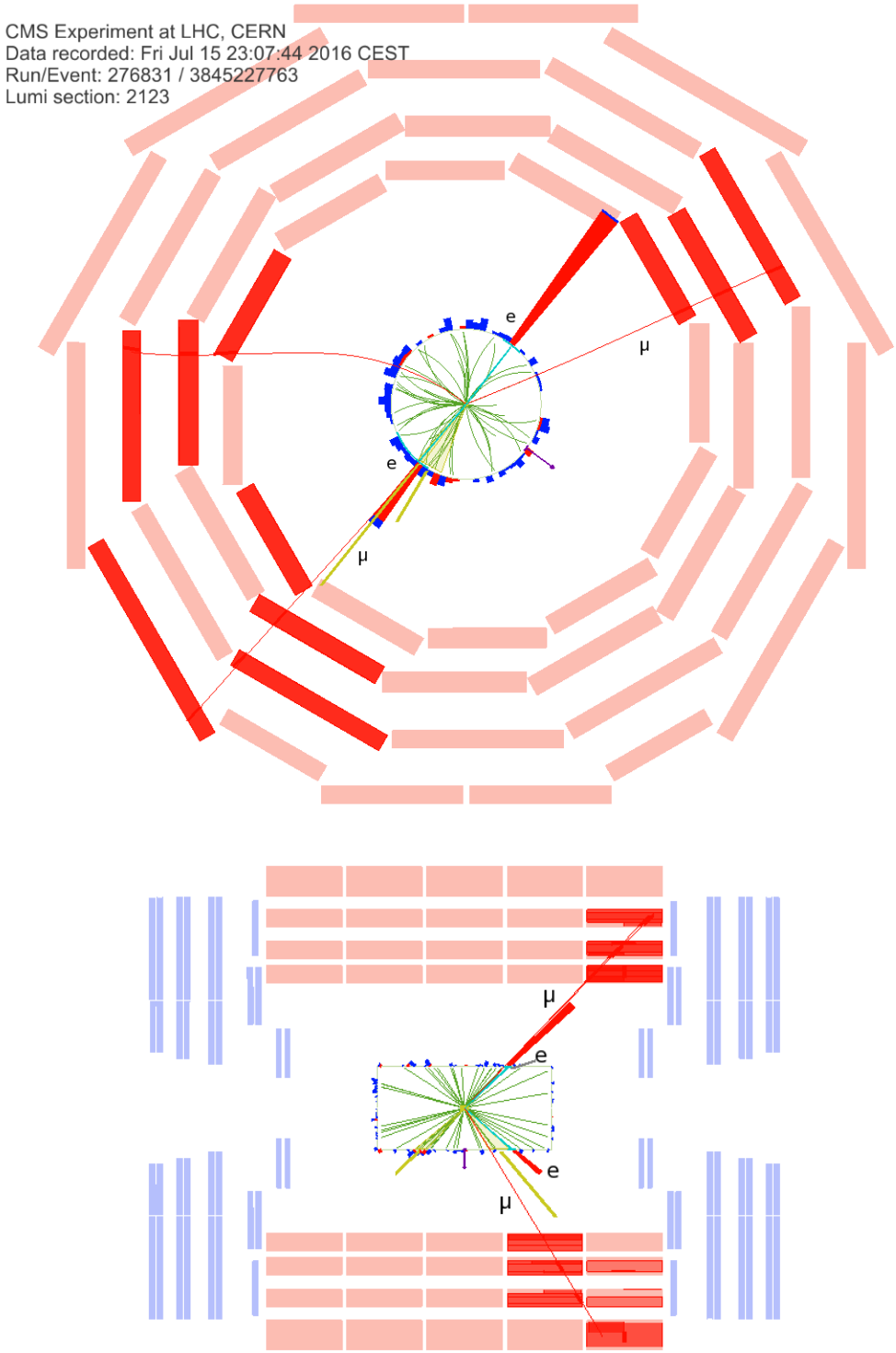

Figure 35: Event view of a 2e2μ event. Left side shows $\rho - \phi$ view, right side the ρ−z view.

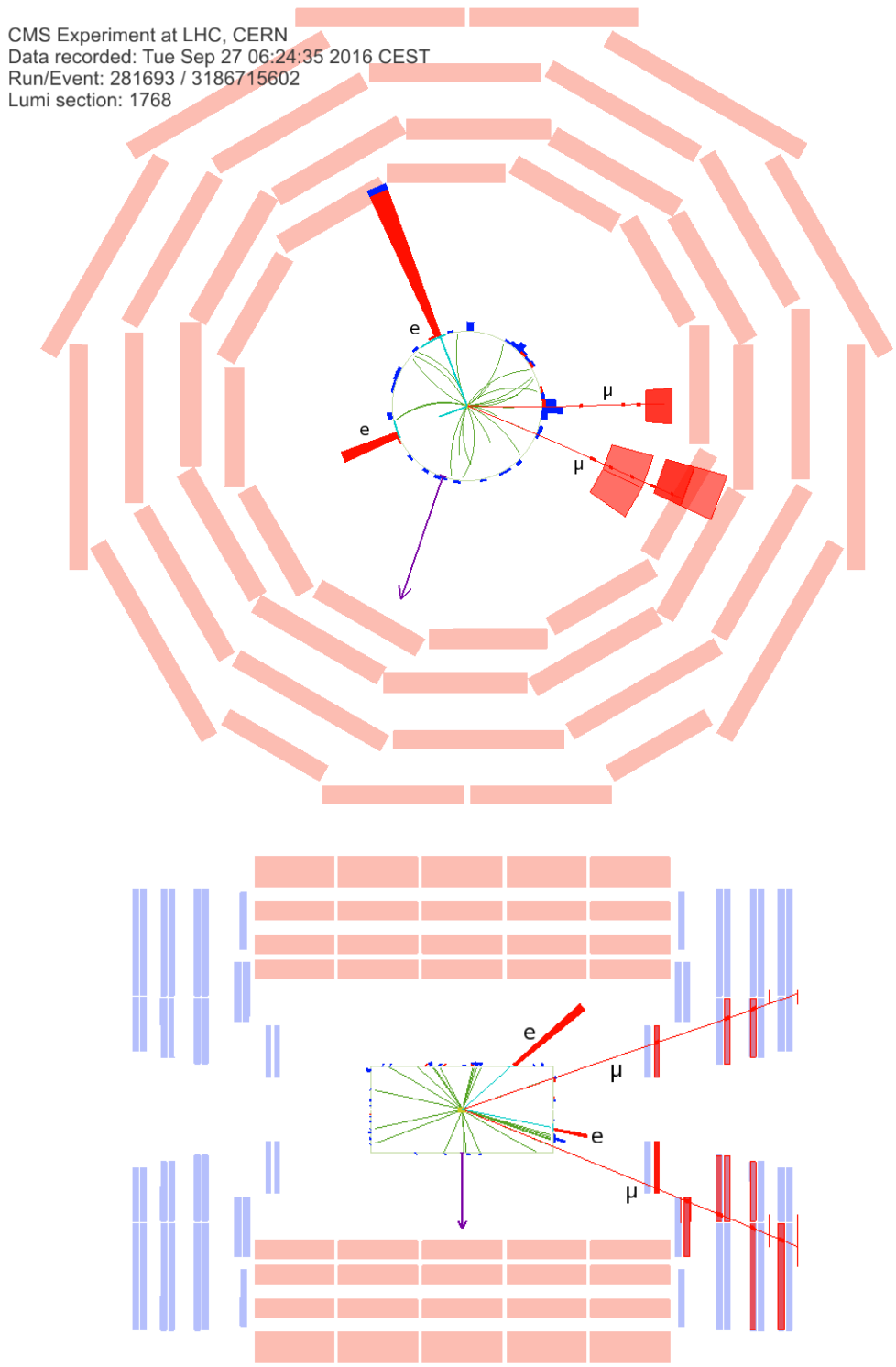

Figure 36: Event view of a 2e2μ event. Left side shows $\rho - \phi$ view, right side the ρ−z view.

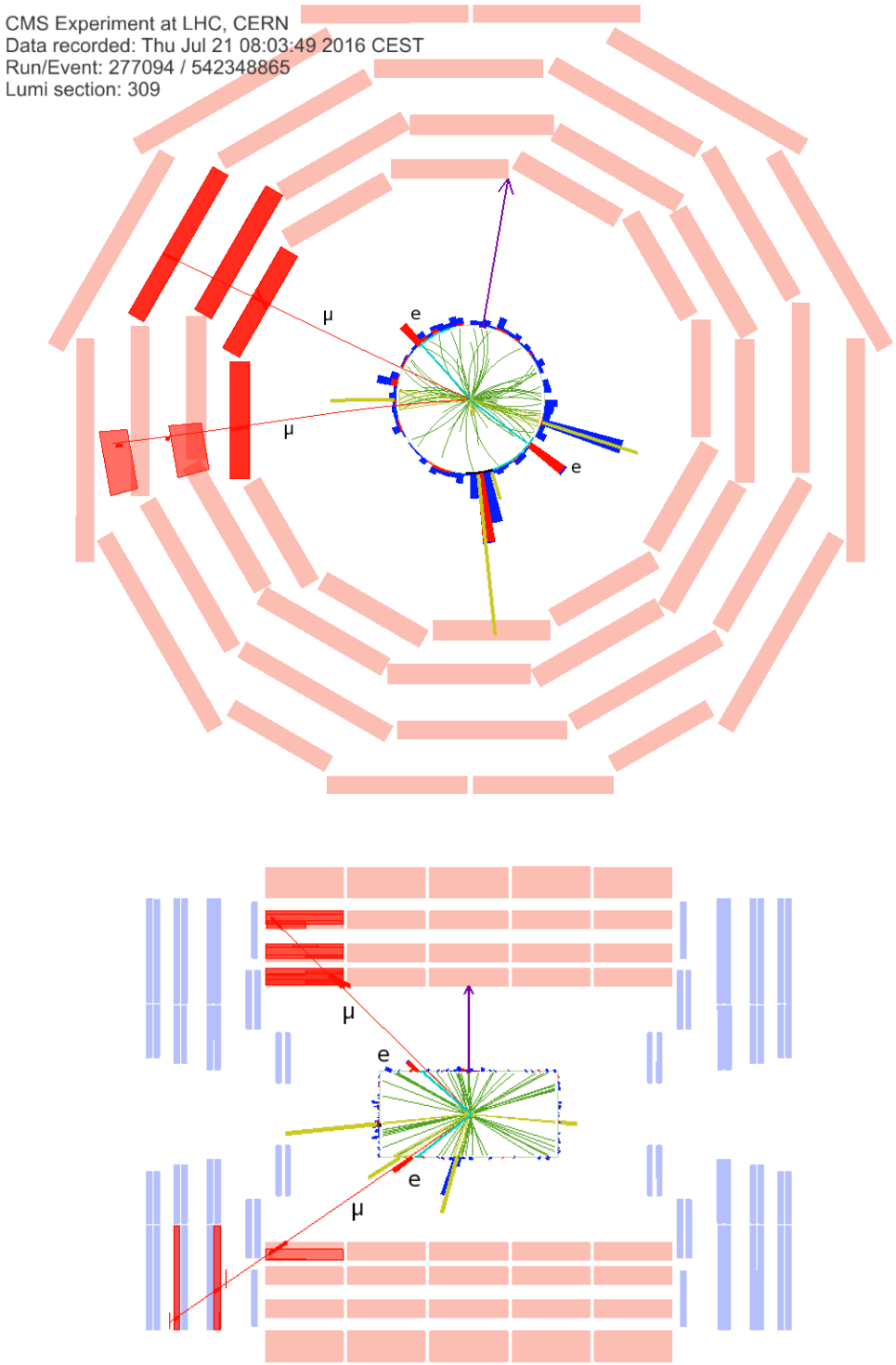

Figure 37: Event view of a 2e2μ event. Left side shows $\rho - \phi$ view, right side the ρ−z view.

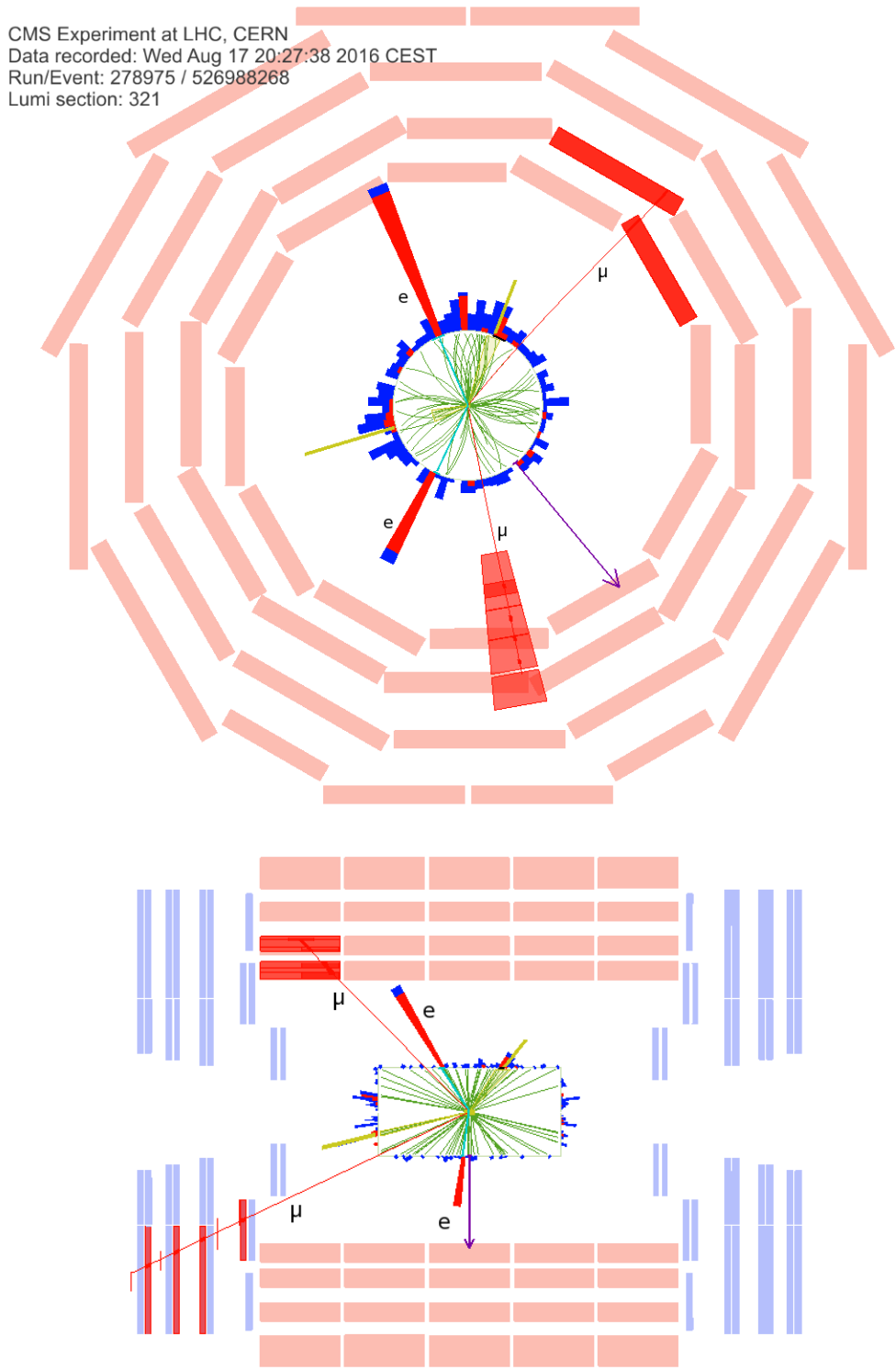

Figure 38: Event view of a 2e2μ event. Left side shows $\rho - \phi$ view, right side the ρ−z view.

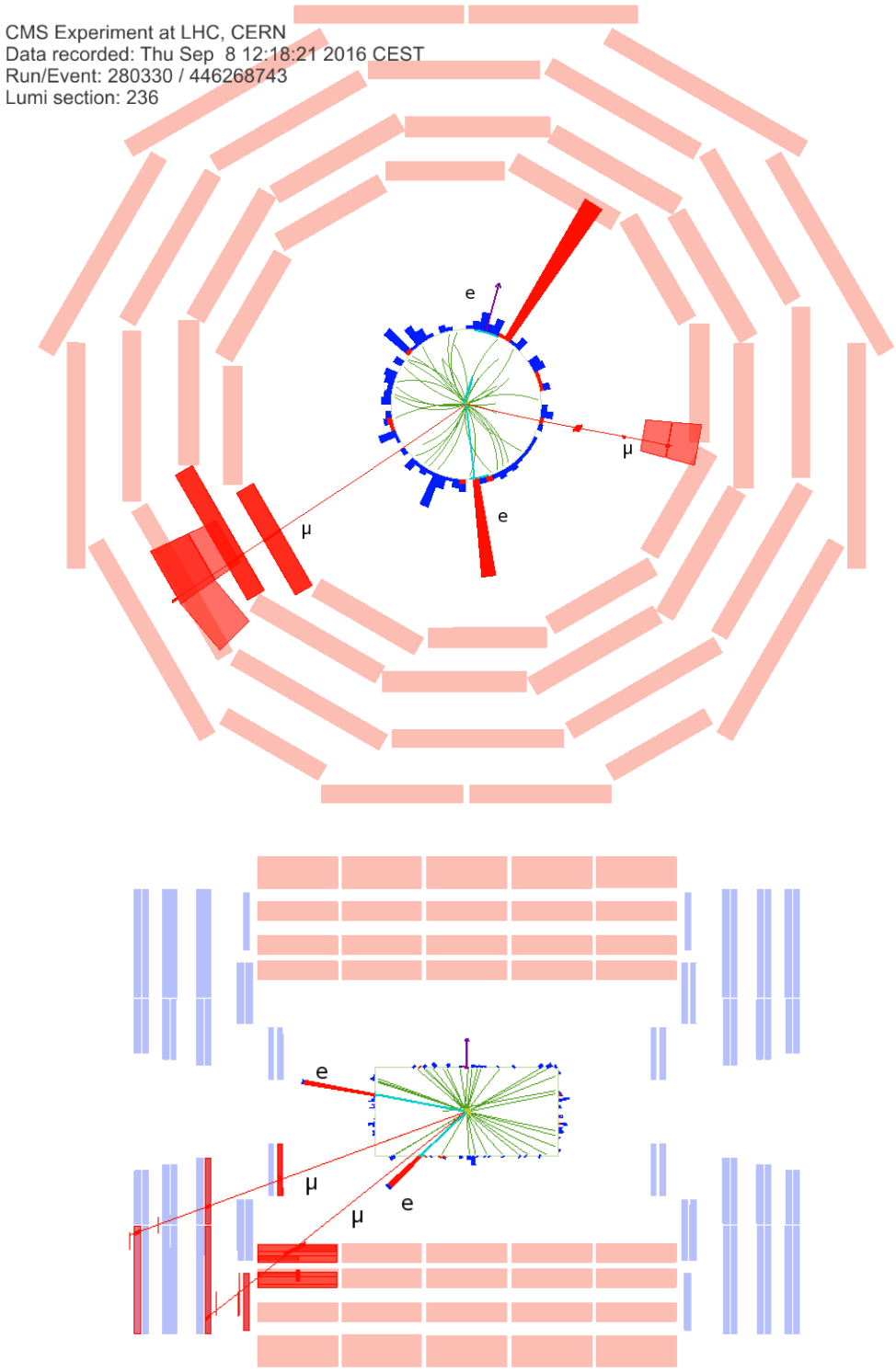

Figure 39: Event view of a 2e2μ event. Left side shows $\rho - \phi$ view, right side the ρ−z view.

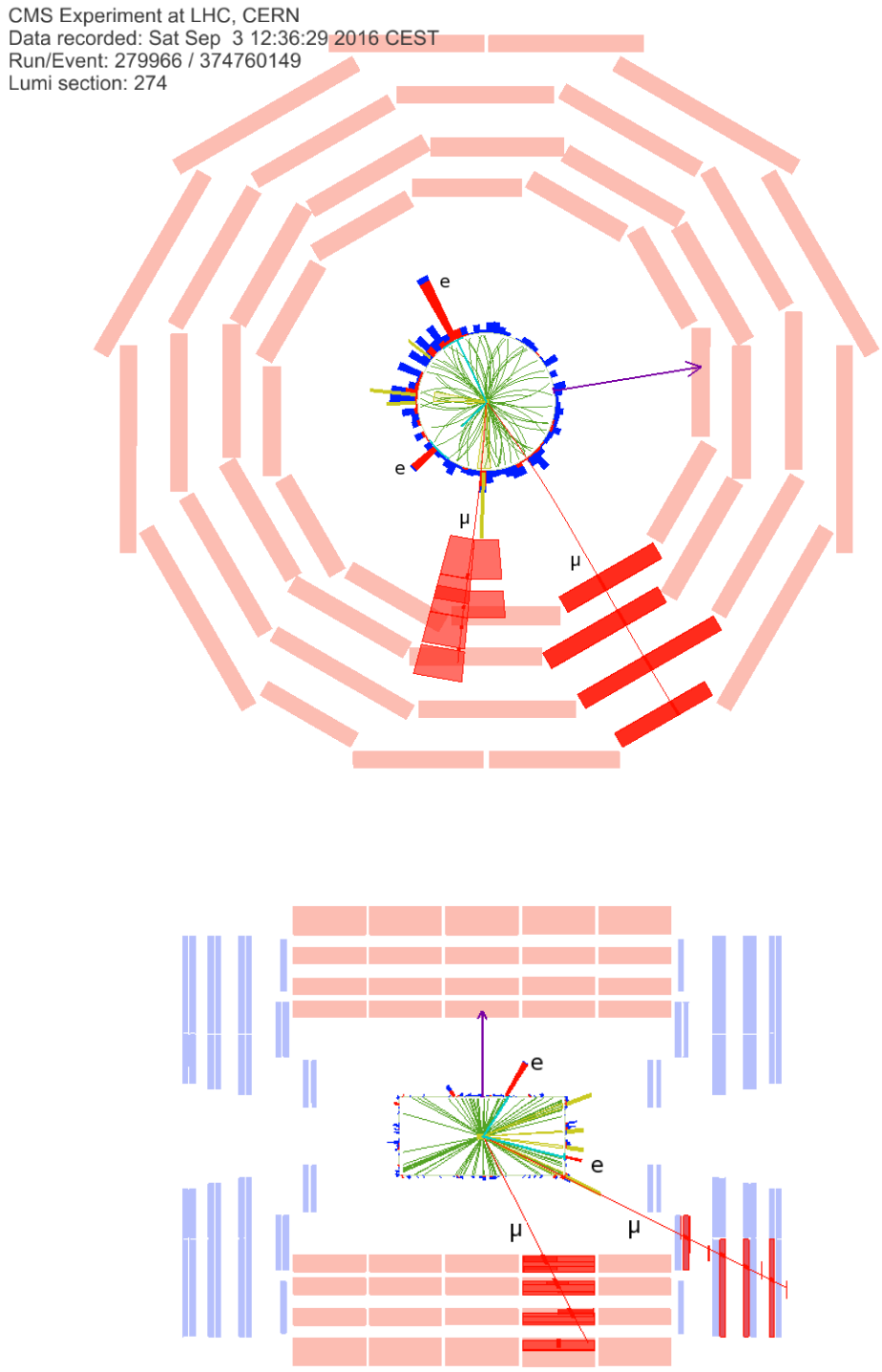

Figure 40: Event view of a 2e2μ event. Left side shows $\rho - \phi$ view, right side the ρ−z view.

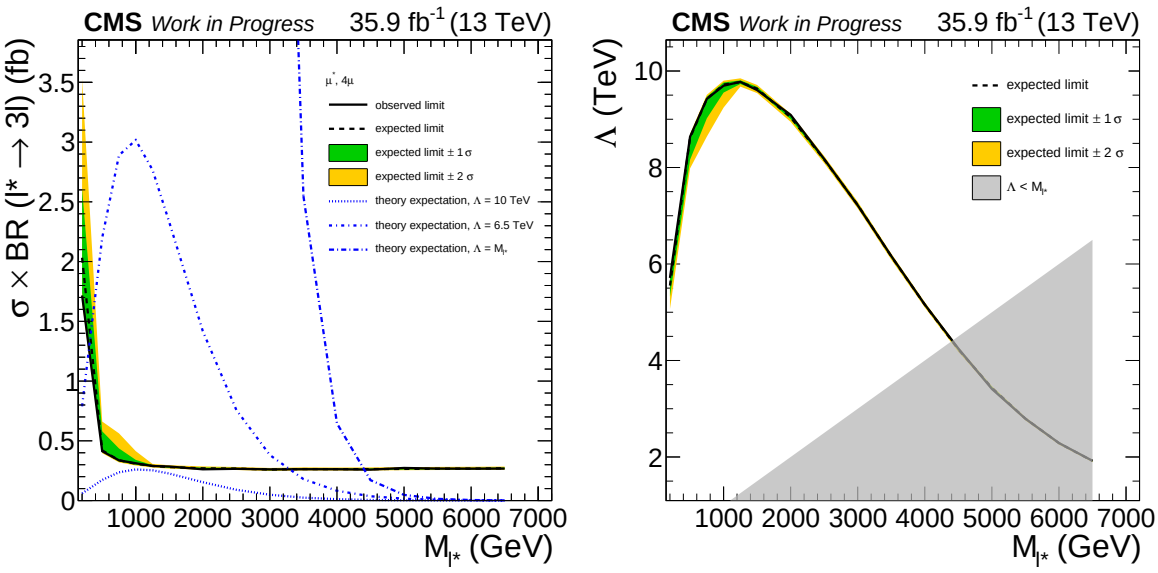

Figure 41: Limit on cross section (left) and Λ (right) based on the 4μ channel only.

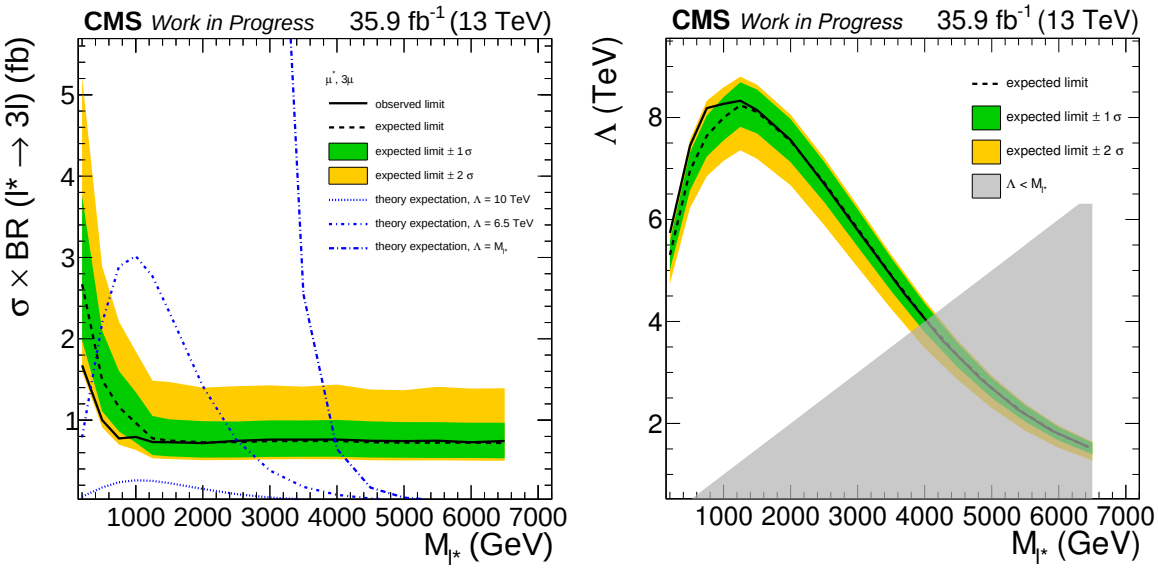

Figure 42: Limit on cross section (left) and Λ (right) based on the 3μ channel only.

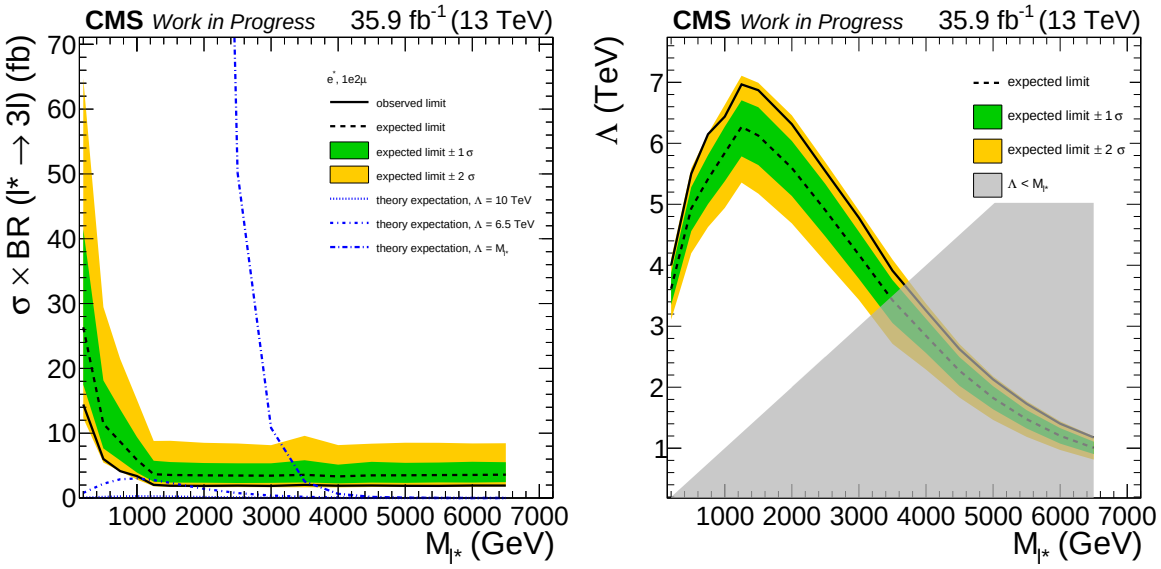

Figure 43: Limit on cross section (left) and Λ (right) based on the 1e2μ channel only.

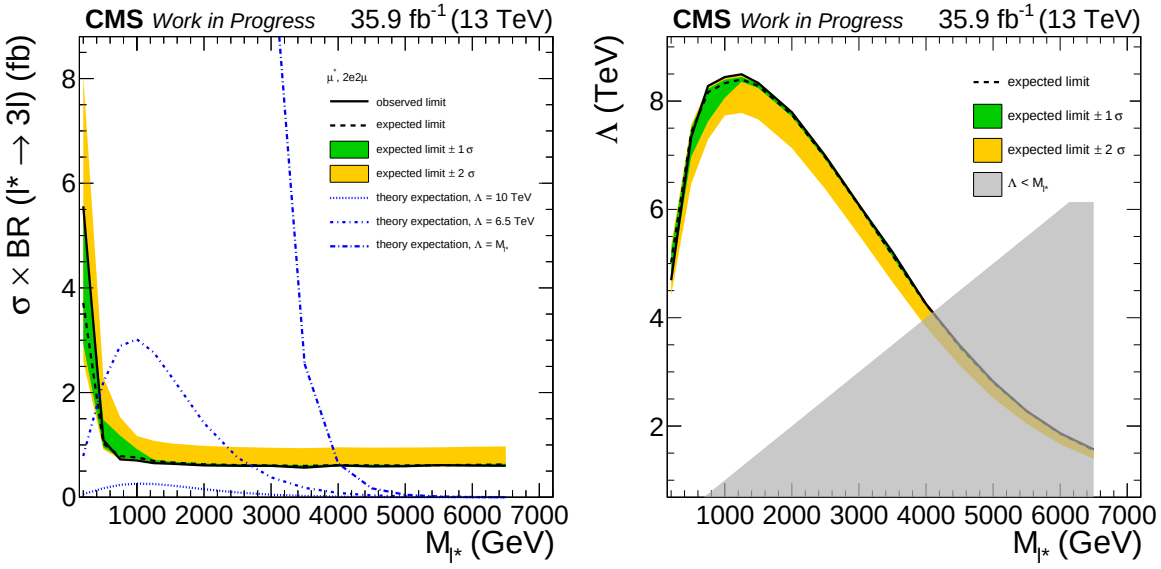

Figure 44: Limit on cross section (left) and Λ (right) based on the 2e2μ channel only, calculated for possible μ^* signals.

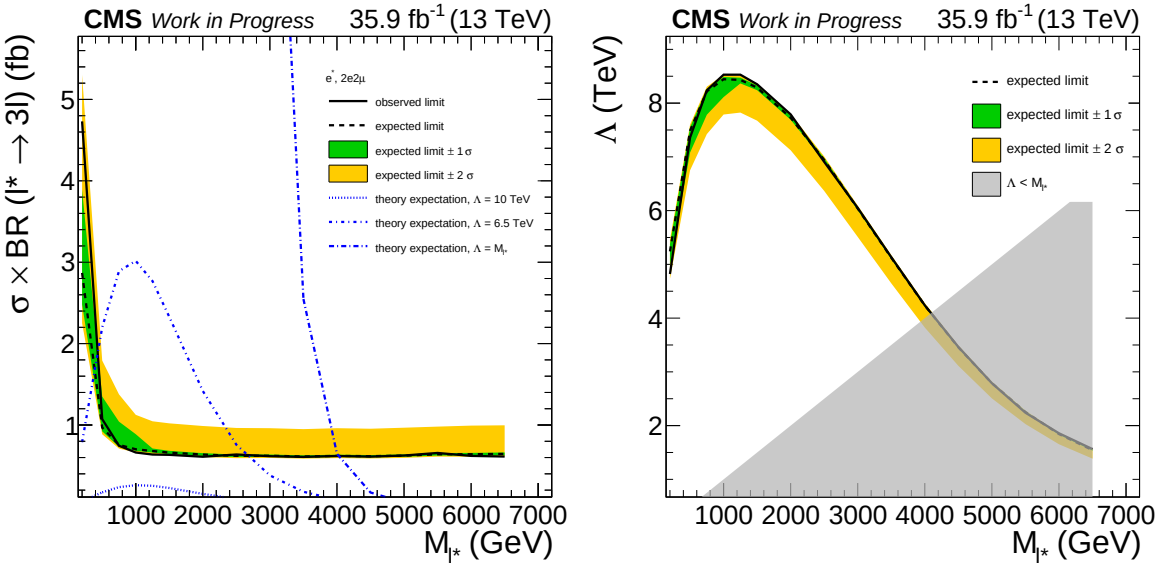

Figure 45: Limit on cross section (left) and Λ (right) based on the 2e2μ channel only, calculated for possible e^* signals.

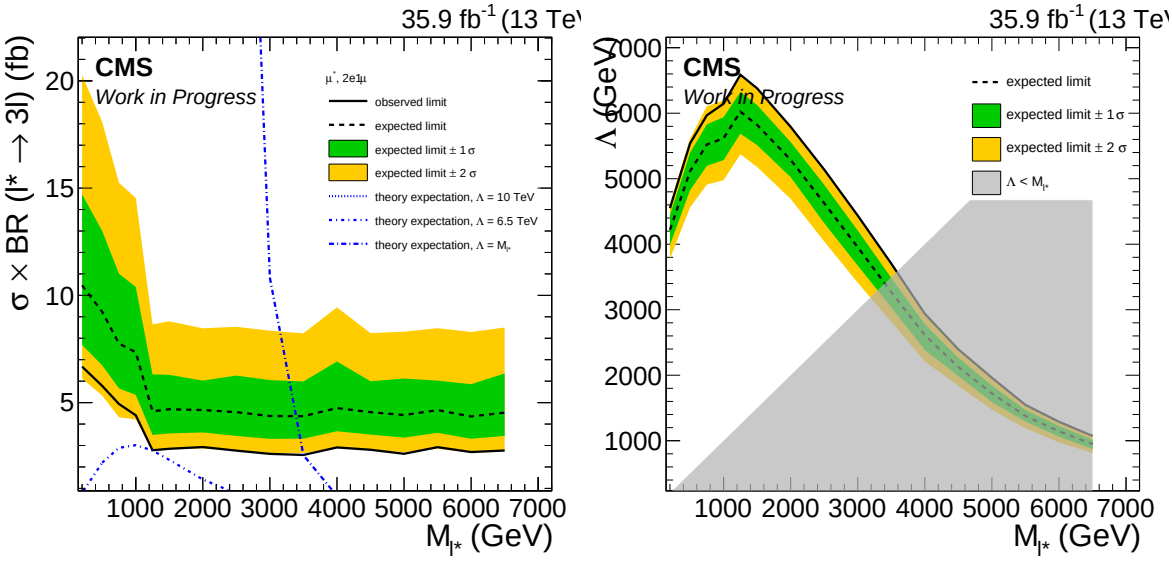

Figure 46: Limit on cross section (left) and Λ (right) based on the 2e1μ channel only.

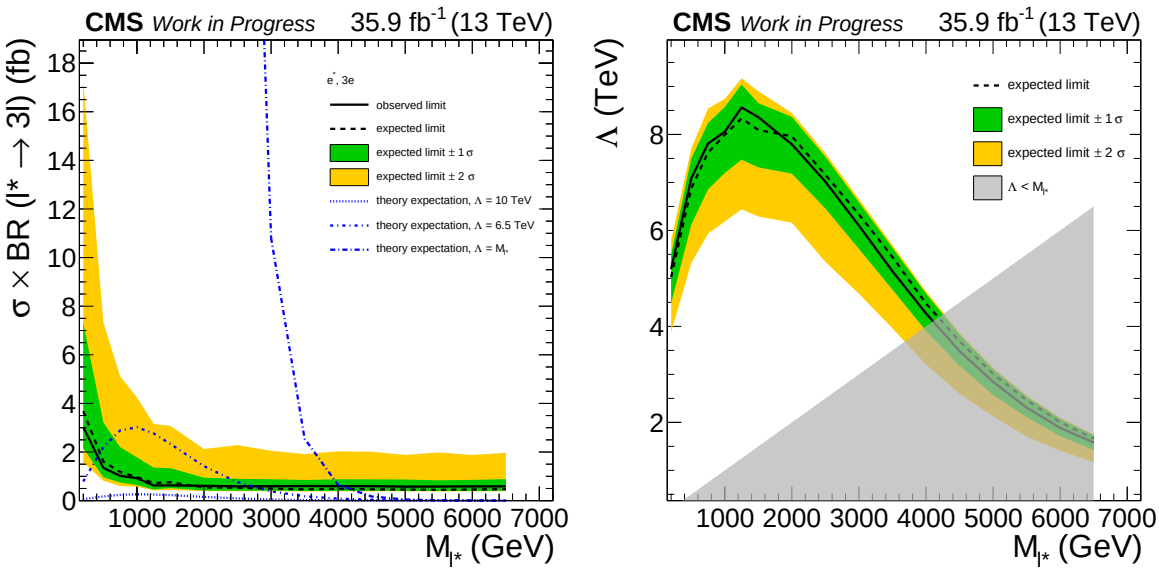

Figure 47: Limit on cross section (left) and Λ (right) based on the 3e channel only.

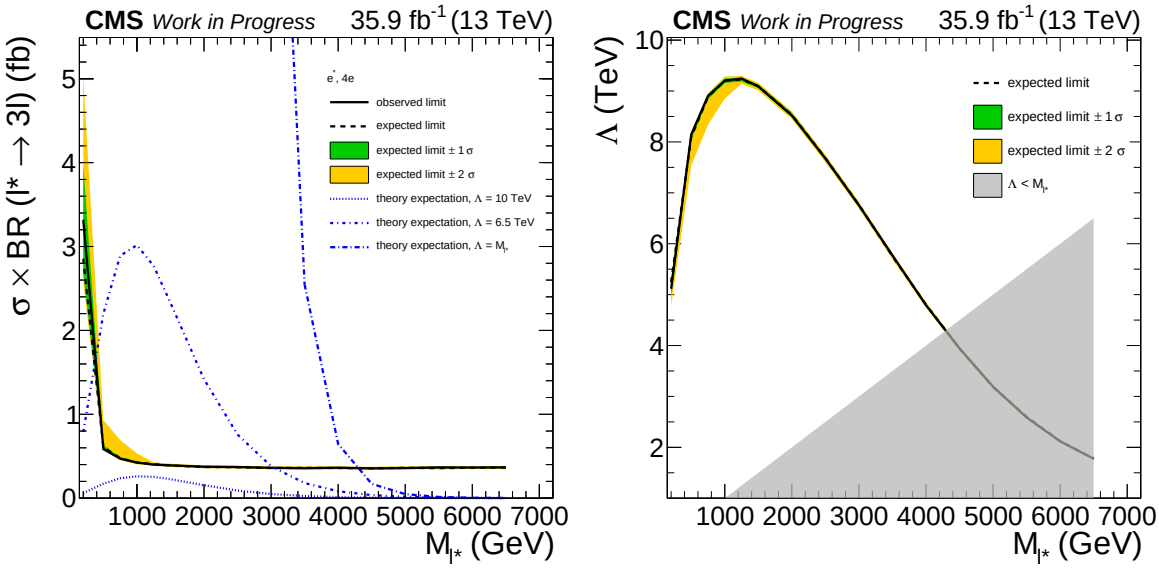

Figure 48: Limit on cross section (left) and Λ (right) based on the 4e channel only.

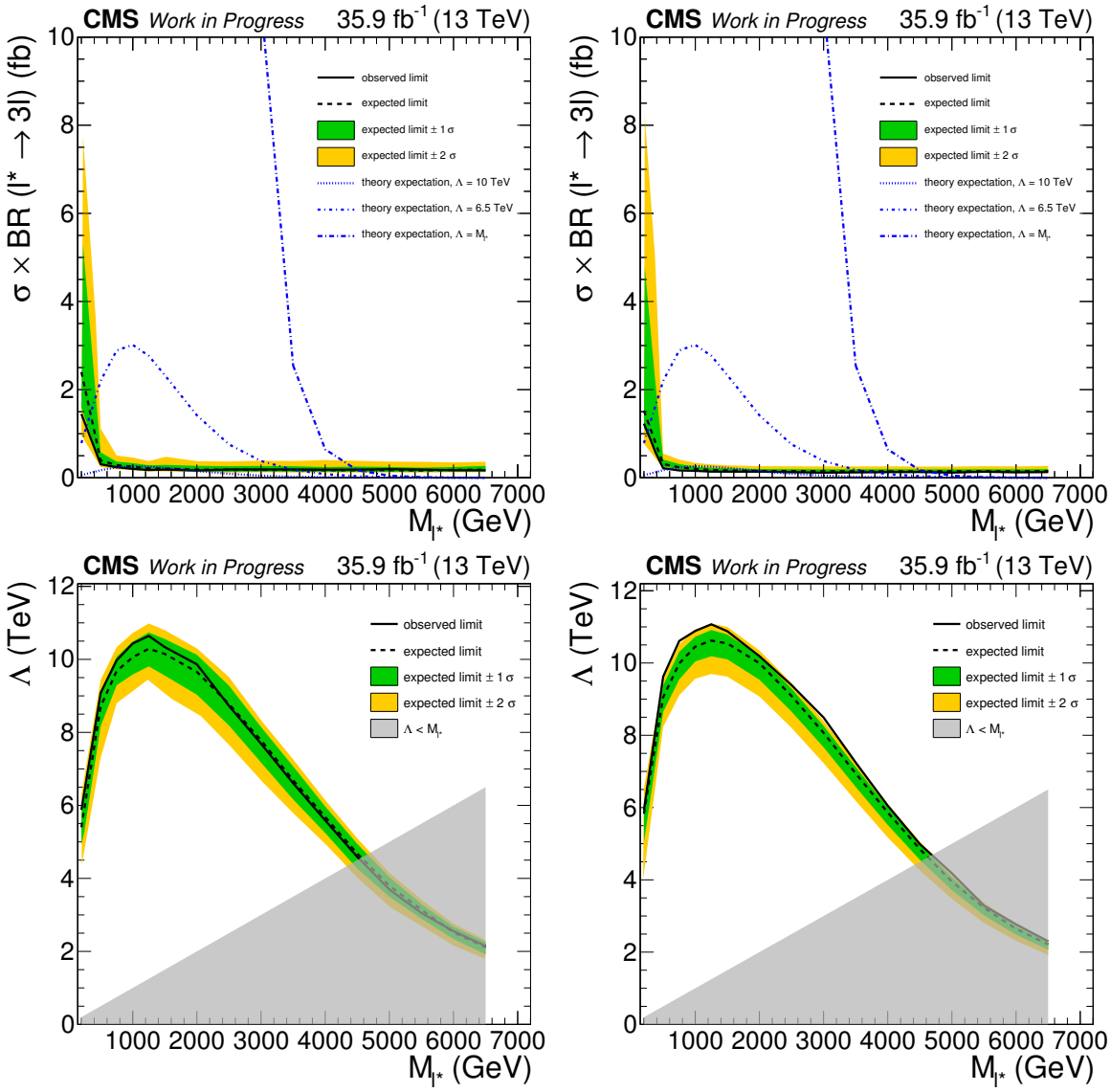

Figure 49: Combined limit on cross section (top) and Λ (bottom) for both e^* (left) and μ^* (right) calculated using a broad binning approach for both channels.

References

[1] K. A. Olive et al. Review of Particle Physics. *Chin. Phys.*, C38:090001, 2014.

[2] Georges Aad et al. Search for new phenomena with photon+jet events in proton-proton collisions at $\sqrt{s} = 13$ TeV with the ATLAS detector. *JHEP*, 03:041, 2016.

[3] U. Baur, M. Spira, and P. M. Zerwas. Excited-quark and -lepton production at hadron colliders. *Phys. Rev. D*, 42:815–824, Aug 1990.

[4] David Griffiths. *Introduction to Elementary Physics*. WILEY-VCH, Weinheim, 2 edition, 2010. Revised Edition.

[5] Martin Erdmann. Particle Physics I, II. Lecture, 2016. Master course lecture, RWTH Aachen University.

[6] Serguei Chatrchyan et al. Observation of a new boson at a mass of 125 GeV with the CMS experiment at the LHC. *Phys. Lett.*, B716:30–61, 2012.

[7] Georges Aad et al. Observation of a new particle in the search for the Standard Model Higgs boson with the ATLAS detector at the LHC. *Phys. Lett.*, B716:1–29, 2012.

[8] Standard Model of Elementary Particles. `https://en.wikipedia.org/wiki/Standard˙Model#/media/File:Standard˙Model˙of˙Elementary˙Particles.svg`, 04 2017.

[9] E. Fermi. Versuch einer theorie der β-strahlen. i. *Zeitschrift für Physik*, 88(3):161–177, Mar 1934.

[10] L. Glashow. Partial-symmetries of weak interactions. `https://doi.org/10.1016/0029-5582(61)90469-2`, 02 1961.

[11] Steven Weinberg. A model of leptons. *Phys. Rev. Lett.*, 19:1264–1266, Nov 1967.

[12] K. Nakamura et al. The review of particle physics. *J. Phys. G*, 37:075021, 2010. Sec. 33.3.1.

[13] O. J. P. Éboli, S. M. Lietti, and Prakash Mathews. Excited leptons at the cern large hadron collider. *Phys. Rev. D*, 65:075003, Mar 2002.

[14] O. W. Greenberg and C. A. Nelson. Composite models of leptons. *Phys. Rev. D*, 10:2567, 1974.

[15] O. W. Greenberg and Joseph Sucher. A quantum structure dynamic model of quarks, leptons, weak vector bosons, and Higgs mesons. *Phys. Lett. B*, 99:339, 1981.

[16] Matthias Klaus Endres. Searches for Excited Leptons in $\sqrt{s} = 8$ and 13 TeV CMS Data. 05 2017.

[17] Search for excited electrons and muons with 13 fb^{-1} of proton–proton collisions at $\sqrt{s} = 8$ TeV with the ATLAS detector. Technical Report ATLAS-CONF-2012-146, CERN, Geneva, Nov 2012.

[18] The CMS Collaboration. The CMS experiment at the CERN LHC. *Journal of Instrumentation*, 3(08):S08004, 2008.

[19] Lyndon Evans and Philip Bryant. Lhc machine. *Journal of Instrumentation*, 3(08):S08001, 2008.

[20] LEP Design Report: Vol.2. The LEP Main Ring. 1984.

[21] CERN Document Server. CERN's accelerator complex. `https://cds.cern.ch/record/1621583/files/CERN's-accelerator-complex2013.jpg?subformat=icon-1440`, 10 2013.

[22] The ALICE Collaboration. The alice experiment at the cern lhc. *Journal of Instrumentation*, 3(08):S08002, 2008.

[23] The ATLAS Collaboration. The atlas experiment at the cern large hadron collider. *Journal of Instrumentation*, 3(08):S08003, 2008.

[24] The LHCb Collaboration. The lhcb detector at the lhc. *Journal of Instrumentation*, 3(08):S08005, 2008.

[25] Performance of muon reconstruction including Alignment Position Errors for 2016 Collision Data. Nov 2016.

[26] CERN Document Server C.Eck et al. Lhc computing grid : Technical design report. `http://cds.cern.ch/record/840543`, 06 2005.

[27] CMS Monte Carlo Validation Group. MC-validation twiki. `https://twiki.cern.ch/twiki/bin/viewauth/CMS/GeneratorMain`, 01 2018.

[28] CMS Collaboration. CMS Luminosity Measurements for the 2016 Data Taking Period. 2017.

[29] J. Allison et al. Geant4 developments and applications. `doi:10.1109/TNS.2006.869826`, 02 2006.

[30] Simone Alioli, Paolo Nason, Carlo Oleari, and Emanuele Re. A general framework for implementing NLO calculations in shower Monte Carlo programs: the POWHEG BOX. *JHEP*, 06:043, 2010.

[31] Stefano Frixione, Paolo Nason, and Giovanni Ridolfi. A Positive-weight next-to-leading-order Monte Carlo for heavy flavour hadroproduction. *JHEP*, 09:126, 2007.

[32] Torbjörn Sjöstrand, Stefan Ask, Jesper R. Christiansen, Richard Corke, Nishita Desai, Philip Ilten, Stephen Mrenna, Stefan Prestel, Christine O. Rasmussen, and Peter Z. Skands. An Introduction to PYTHIA 8.2. *Comput. Phys. Commun.*, 191:159–177, 2015.

[33] J. Alwall, R. Frederix, S. Frixione, V. Hirschi, F. Maltoni, O. Mattelaer, H. S. Shao, T. Stelzer, P. Torrielli, and M. Zaro. The automated computation of tree-level and next-to-leading order differential cross sections, and their matching to parton shower simulations. *JHEP*, 07:079, 2014.

[34] F. Cascioli, T. Gehrmann, M. Grazzini, S. Kallweit, P. Maierhöfer, A. von Manteuffel, S. Pozzorini, D. Rathlev, L. Tancredi, and E. Weihs. ZZ production at hadron colliders in NNLO QCD. *Phys. Lett.*, B735:311–313, 2014.

[35] Fabrizio Caola, Kirill Melnikov, Raoul Röntsch, and Lorenzo Tancredi. QCD corrections to ZZ production in gluon fusion at the LHC. *Phys. Rev.*, D92(9):094028, 2015.

[36] A. M. Sirunyan et al. Particle-flow reconstruction and global event description with the CMS detector. *JINST*, 12(10):P10003, 2017.

[37] W Adam, R Frühwirth, A Strandlie, and T Todorov. Reconstruction of electrons with the gaussian-sum filter in the cms tracker at the lhc. *Journal of Physics G: Nuclear and Particle Physics*, 31(9):N9, 2005.

[38] CMS EGamma POG. Electron ID twiki. `https://twiki.cern.ch/twiki/bin/viewauth/CMS/CutBasedElectronIdentificationRun2`, 10 2017.

[39] G. Abbiendi et al. Muon reconstruction in the CMS detector. *CMS AN 2008/97*, May 2009.

[40] CMS Muon POG. Muon reconstruction, twiki. `https://twiki.cern.ch/twiki/bin/view/CMSPublic/SWGuideMuons`, 03 2009.

[41] The CMS Collaboration. Muon Identification and Isolation efficiency on full 2016 dataset. Mar 2017.

[42] Pierre Billoir. Progressive track recognition with a kalman-like fitting procedure. *Computer Physics Communications*, 57(1):390 – 394, 1989.

[43] CMS Muon POG. Global muons, twiki. `https://twiki.cern.ch/twiki/bin/view/CMSPublic/WorkBookMuonAnalysis#GlobalMu`, 01 2017.

[44] CMS Muon POG. Muon ID twiki. `https://twiki.cern.ch/twiki/bin/viewauth/CMS/SWGuideMuonIdRun2`, 01 2017.

[45] CMS Muon POG. Muon pog twiki. https://twiki.cern.ch/twiki/bin/view/CMS/MuonPOG, 01 2017.

[46] CMS EGamma POG. Electron ID twiki. https://twiki.cern.ch/twiki/bin/view/CMS/EgammaPOG, 10 2017.

[47] CMS Collaboration. Reference muon momentum scale and resolution. https://twiki.cern.ch/twiki/bin/viewauth/CMS/MuonReferenceResolution, 07 2016.

[48] EGamma POG (CMS). Energy smearing and scale correction. https://twiki.cern.ch/twiki/bin/view/CMS/EGMSmearer, 2017.

[49] Lumi Physics Objects Group (CMS). Luminosity physics object group. https://twiki.cern.ch/twiki/bin/view/CMS/TWikiLUM, 2017.

[50] H. Abramowicz and A. Caldwell. HERA collider physics. *Rev. Mod. Phys.*, 71:1275–1410, 1999.

[51] Alan D. Martin. Proton structure, Partons, QCD, DGLAP and beyond. *Acta Phys. Polon.*, B39:2025–2062, 2008.

[52] Andy Buckley, James Ferrando, Stephen Lloyd, Karl Nordström, Ben Page, Martin Räfenacht, Marek Schönherr, and Graeme Watt. LHAPDF6: parton density access in the LHC precision era. *Eur. Phys. J.*, C75:132, 2015.

[53] CMS Collaboration. Higgscombine tool twiki. https://twiki.cern.ch/twiki/bin/viewauth/CMS/SWGuideHiggsAnalysisCombinedLimit, 08 2017.

[54] Joel Heinrich, Craig Blocker, John Conway, Luc Demortier, Louis Lyons, Giovanni Punzi, and Pekka K. Sinervo. Interval estimation in the presence of nuisance parameters. 1. Bayesian approach. 2004.

[55] Georges Aad et al. Search for excited leptons in proton-proton collisions at $\sqrt{s} =$ 7 TeV with the ATLAS detector. *Phys. Rev. D*, 85:072003, 2012.